Auroral Imaging as a Tracer of Global Magnetospheric Dynamics

Karl Magnus Laundal

Thesis for the degree of Philosophiae Doctor (PhD)
at the University of Bergen

August, 2010

ISBN 978-82-308-1627-1
Trykk og innbinding: AIT Oslo AS

Preface

This synthesis and a collection of papers are submitted for the degree of philosophiae doctor (PhD) in physics at the Department of Physics and Technology, University of Bergen.

The thesis is divided into an introductory part and a part consisting of four papers submitted to international journals.

Paper I K. M. Laundal and N. Østgaard (2008). Persistent global proton aurora caused by high solar wind dynamic pressure *Journal of Geophysical Research* Vol. 113, doi:10.1029/2008JA013147

Paper II K. M. Laundal and N. Østgaard (2009). Asymmetric auroral intensities in the Earth's Northern and Southern hemispheres *Nature* Vol. 460, doi:10.1038/nature08154

Paper III K. M. Laundal, N. Østgaard, K. Snekvik and H. U. Frey (2010). Inter-hemispheric observations of emerging polar cap asymmetries, *Journal of Geophysical Research* Vol. 115, doi:10.1029/2009JA015160

Paper IV K. M. Laundal, N. Østgaard, H. U. Frey and J. Weygand (2010). Seasonal and IMF dependent polar cap contraction during substorm expansion phase, *Journal of Geophysical Research* in press, doi:10.1029/2010JA015910

This work is funded by the Norwegian Research Council project *IPY-ICESTAR* with project number 176045/S30.

Contents

Acknowledgements

This thesis is the result of five years of working with auroral images, first as a master student, and the last three years as a PhD student. Professor Nikolai Østgaard has been my supervisor since the beginning. I could not have asked for a more encouraging, inspiring, and ambitious supervisor. He has provided me with the basic ideas which got me started with my studies, and he has been enthusiastic about discussing the results, sometimes keeping us occupied for several hours, at his office, and over coffee, lunch or beer.

My five years at the space science group at the University of Bergen have been very enjoyable, much thanks to my fellow students, and the professors and engineers who work there. I would especially like to thank my officemate Thomas Gjesteland, and past and present PhD students and residents of Room 423. I am very happy to have collaborated with Kristian Snekvik, who has always been eager to discuss new ideas and problems. He is also a co-author on one of the papers, and he proof-read this thesis.

Earlier this year, I spent three months at the High Altitude Observatory at the National Center for Atmospheric Research, in Boulder, Colorado. Much of this thesis was written there, between gathering data for, and running the AMIE model. I would like to thank Gang Lu for making my stay in Boulder interesting and productive.

This work would not have been possible if not for the people behind the excellent data sets which we have used. The FUV instrument, and much of the software that was used for data analysis, was made by the FUV team at Space Sciences Laboratory at UC Berkeley. I would particularly like to thank the P.I., Stephen Mende, and Harald Frey, who has also been a co-author on two of the papers in this thesis. Data from the VIS Earth camera was provided by P.I. John Sigwarth.

I am also very grateful to my friends and family for caring about me, and how my studies progress, and for trying (and bravely pretending) to care about the magnetosphere. Finally, I would like to thank Anne Marie for supporting me despite my many late nights at the office, not to mention being left alone (and morning sick) for three months, while I was in Boulder.

Søgne, August 2010 Karl M. Laundal

Chapter 1

Introduction

The aurora is light which is produced when charged particles precipitate from space and collide with the thin gas in the Earth's upper atmosphere, typically at 100−300 km altitude. Depending on the type of atoms/molecules with which the particles collide, photons with different wavelengths (colors) are produced. A continuous spectrum is also emitted because of the deceleration of the charges. From the ground, we see the aurora as thin discrete arcs, often aligned with circles of magnetic latitude. These arcs are produced by precipitation of electrons, accelerated relatively close to Earth ($\sim$ 1 Earth radius) by quasi-static upward electric fields, and electromagnetic wave activity. On a global scale, the aurora resembles ovals, with centers close to magnetic poles in the northern and southern hemispheres. In addition to the discrete arcs, the auroral ovals are comprised by a background of diffuse aurora. Both the arcs and the diffuse aurora can be seen with appropriate instruments, such as the cameras used in this thesis.

The observational basis of this study is global UV images of the aurora, taken by instruments on the NASA satellites IMAGE and Polar. To some extent, these images can be seen as projections of a much larger region further out in space, to which the Earth is magnetically connected. This region, called the magnetosphere, is constantly changing: Expanding, contracting, twisting, taking in and ejecting plasma, and opening and closing its connection to the interplanetary magnetic field (IMF). Global auroral images can help to identify and quantify these processes.

In Paper I in this thesis, we present observations which demonstrate a very direct relationship between the global aurora and the degree of compression of the magnetosphere. Using images from the SI-12 camera on the IMAGE satellite, which is sensitive to auroral emissions produced solely by proton precipitation, we observe a prompt increase, and persistently elevated intensity when the magnetosphere is compressed. When it expands, the proton aurora immediately diminishes. The compression and expansion of the magnetosphere was deduced from observed changes in the pressure in the solar wind.

In Papers II and III, we study in great detail an event when we had global UV images of the aurora in both hemispheres simultaneously. The unique data from this and a few other events have previously been investigated by *Østgaard et al.* (2004, 2005c), who focused on the location of corresponding auroral features in the two hemispheres (i.e. aurora which

is produced by charged particles moving along the same magnetic field line). They found evidence for a temporally twisted magnetosphere, enforced by the solar wind and IMF. In Paper II, we present an example when the technique employed by Østgaard et al. is not applicable; corresponding large-scale features in the two hemispheres could not be identified. The inter-hemispheric asymmetries in the auroral intensity presented in this paper are suggested to signify currents flowing along magnetic field lines between the two hemispheres. In Paper III we look at the same event, but here we focus on the interior boundary of the auroral ovals, i.e. the poleward boundary of the particle precipitation. The location of this boundary is often assumed to coincide with the boundary between magnetic field lines which are connected to both hemispheres (closed), and magnetic field lines which are connected to the IMF (open). We show that as magnetic flux is exchanged between these regions, the location of the boundary can become different in the two hemispheres, possibly because of differences between the upper atmosphere in the two hemispheres. In Paper IV, we use $\sim 30,000$ auroral images from one hemisphere to study the contraction of the auroral oval statistically. The main result from this study is that, as the oval contracts, average differences appear for different seasonal conditions, as well as for different orientations of the IMF.

This thesis starts with a survey of some fundamental concepts in space plasma physics, followed by a description of the geospace system and the aurora. We then summarize some of the previous work on inter-hemispheric asymmetries. A description of the instruments, and some techniques that we have used in the papers are then presented. The last chapter contains brief summaries of the papers. The main part of this thesis is four scientific papers:

Paper I:

Persistent global proton aurora caused by high solar wind dynamic pressure

Paper II:

Asymmetric auroral intensities in the Earth's Northern and Southern hemispheres

Paper III:

Inter-hemispheric observations of emerging polar cap asymmetries

Paper IV:

Seasonal and IMF dependent nightside polar cap contraction during substorm expansion phase

Chapter 2

Basic concepts in space plasma physics

Space physics is still a relatively young field. Before the launch of the first satellites[1], all knowledge about space was inferred from ground based observations. For example, the existence of a conducting layer in the upper atmosphere, the ionosphere, was postulated around 1900, as the means by which radio waves could be transmitted across the Atlantic ocean. To some extent, the field is still in a descriptive state. This is also reflected by the papers in this thesis, which can be considered primarily as reports of new observational findings. However, we also try to place these findings in a scientific context. The aim of the first part of this thesis is to give a brief review of the current understanding of this scientific context, in a more general way than what is permitted by the format of the scientific papers.

In this chapter we give a brief introduction to space plasma physics. We choose an approach which is inspired by recent works by *Parker* (1996, 1997, 2000, 2007) and *Vasyliunas* (2001, 2005a,b), who present this topic from a somewhat untraditional angle, focusing on causality. This is done by treating the plasma as a fluid, and explaining the dynamics of the fluid in terms of first principles in physics: Newton's laws of motion, and Maxwell's equations. The crude introduction which is presented here is meant to clarify the view which is adopted in the rest of this thesis. For the purpose of brevity, we shall refer to the above citations, and the books by *Baumjohann and Treumann* (1997), *Paschmann et al.* (2003), and *Griffiths* (1981) for mathematical derivations, and elaborations on many of the details which could not be included here.

2.1 Charged particles and electromagnetic fields

The universe is filled with plasma, a gas consisting of electrically charged particles. Only a very few exceptions to this statement exist, and one of them is the cold surface of the Earth, and a surrounding thin layer ($\sim 1/60$ of an Earth radius thick) of gas, called the

[1]The first satellite, Sputnik, was launched in 1957.

atmosphere. The universe is also filled with a magnetic field, and to this there is no known exceptions (*Parker* (2007) p. 14). The physics of space can therefore be said to be that of charged particles moving in magnetic, and sometimes electric fields. The most head-on approach to treat such a system mathematically, is to consider Newton's law of motion for each particle,

$$\frac{d\mathbf{p}_k}{dt} = q_k(\mathbf{E} + \mathbf{u}_k \times \mathbf{B}) \tag{2.1}$$

where $\mathbf{p}_k$ is the momentum of particle number k, q_k is its charge, $\mathbf{u}_k$ is its velocity, and $\mathbf{E}$ and $\mathbf{B}$ are the electric and magnetic fields. As is clear from this equation, the particles move in response to electric and magnetic fields. However, collectively they also change these fields, which behave according to Maxwell's equations,

$$\nabla \cdot \mathbf{E} = \rho/\epsilon_0 \tag{2.2}$$

$$\frac{\partial \mathbf{B}}{\partial t} = -\nabla \times \mathbf{E} \tag{2.3}$$

$$\nabla \cdot \mathbf{B} = 0 \tag{2.4}$$

$$\nabla \times \mathbf{B} = \mu_0 \mathbf{j} + \epsilon_0 \mu_0 \frac{\partial \mathbf{E}}{\partial t} \tag{2.5}$$

where ρ is the charge density and $\mathbf{j}$ is the current density, which depend on the location and velocity of every single charged particle.

This kind of approach belongs to kinetic plasma theory. The enormous number of equations, resulting from the enormous number of particles in the magnetosphere, makes it clear that this approach is of little aid in getting a qualitative basic understanding of global phenomena, at least without the aid of massive computer power. Luckily, there is a simpler approach, in which the plasma can be treated as a fluid.

2.2 Fluid description of a plasma

The key transition in going from a kinetic description to a fluid description of a plasma (or any other substance that can be treated as a continuum), is the introduction of macroscopic quantities. Instead of keeping account of the position of every individual particle, we introduce the density, $n = N/V$, where N is the number of particles in a volume V. Instead of the velocities of each individual particle, $\mathbf{u}_k$, we use the mean velocity, or bulk velocity,

$$\mathbf{v} = \frac{1}{N} \sum_k \mathbf{u}_k \tag{2.6}$$

$\mathbf{u}_k$ can be decomposed as $\mathbf{u}_k = \mathbf{v} + \mathbf{w}_k$, where $\mathbf{w}_k$ is called the thermal velocity of particle number k. By definition of $\mathbf{v}$, the average of $\mathbf{w}_k$ is $\mathbf{0}$. The thermal velocities enter in the pressure tensor:

$$p_{ij} = \frac{1}{V} \sum_k m_k w_{ki} w_{kj} \tag{2.7}$$

where i, j represent the components x, y, z. The macroscopic quantity temperature also depends on the thermal velocities.

We want to be able to use these quantities in differential equations which describe the large-scale dynamics of the system. For this to be possible, two conditions must be fulfilled: 1) The volumes which are considered, $V = \lambda^3$ must be sufficiently large that they contain enough particles that the macroscopic quantities (n, $\mathbf{v}$, pressure, etc.) are not subject to statistical fluctuations. 2) λ must be small compared to the characteristic scale length of variations in the macroscopic quantities (Λ). This is necessary for a differential treatment to make sense.

These two requirements must be balanced according to the need for statistical precision and smallness of λ. In most cases, it is adequate that $\lambda = 10^{-3}\Lambda$ (*Parker* (2007), p. 75). In the case of the solar wind ($n \sim 5$ cm^{-3}) interaction with the magnetosphere ($\Lambda \sim 10^4$ km), we get $\lambda = 10$ km, and $N = 5 \times 10^{18}$. The statistical uncertainty in each cell, $\sim N^{-1/2}$, will be less than 10^{-9}.

The above quantities may be used to describe the plasma as composed by several fluids, e.g. an electron fluid and an ion fluid, in which case two sets of macroscopic variables must be considered, one for each fluid. Another approach is to treat the electrons and ions of a plasma as a single fluid. Multi-fluid theory may be appropriate when the forces acting on the electrons and ions differ, e.g. in the ionosphere, where the friction with neutral particles depends on the particle species. In most of the magnetosphere, a single-fluid approach can be used.

2.2.1 Conservation of mass and momentum

We now look at the differential equations which are used to describe the dynamics of the macroscopic quantities introduced in the previous section. For a derivation of the equations, see e.g. Chapter 7 in *Baumjohann and Treumann* (1997), or Chapter 8 in *Parker* (2007). These equations are conservation laws, and the first law states that the mass of the fluid is conserved:

$$\frac{\partial n}{\partial t} + \frac{\partial}{\partial x_j} n v_j = 0 \tag{2.8}$$

The equation is written on component form, and the subscripts j ($= x, y, z$) are to be summed over. This equation has four unknowns: n, and the three components of the velocity. Newton's second law states that the momentum is conserved. For a fluid, this law takes the form

$$nm\left(\frac{\partial v_i}{\partial t} + v_j \frac{\partial v_i}{\partial x_j}\right) = -\frac{\partial p_{ij}}{\partial x_j} + f_i. \tag{2.9}$$

Again, j is a summation index. m is the mass of the particles in the fluid. For an ion/electron fluid, the mass can be written, $m = m_e + m_i = m_i(1 + m_e/m_i) \approx m_i$, since the lightest ion, H^+, has a mass ≈ 1800 times larger than the electron mass. The pressure tensor describes the momentum flux density transported by the thermal motions of the particles. In the case that the pressure is isotropic, $p_{ij} = p\delta_{ij}$, the pressure term can be

understood as a force which accelerates the plasma in the direction anti-parallel to its gradient. f_i is the external force per unit volume (in the i'th direction). For a space plasma, the most important force is the electromagnetic force, which is the subject of the next section. In the following, we neglect gravity, which typically is small compared to other forces.

Assuming the force f_i to be known, Eq. 2.8 and 2.9 constitute four equations, with four unknowns in addition to the unknown elements of the pressure tensor (note that definition 2.7 implies that $p_{ij} = p_{ji}$). To remedy this, one can introduce yet another conservation law, conservation of energy density. This does however introduce another unknown quantity, the heat flux density. In principle, one can continue introducing new equations and new unknowns ad infinitum. Usually, one therefore truncates the set of equations, for example by making an assumption on the pressure using an equation of state.

For the present purpose, the key aspects of the above discussion is that 1) a plasma can be described as a fluid if its density is well-defined on a scale on which the macroscopic variables do not change much, and 2) that the dynamics of the fluid is governed by the pressure, and forces which are applied on it. This force is the topic of the next section.

2.3 The electromagnetic force on a plasma fluid

We have already mentioned that the collective effect of the charged particles in a plasma can change ambient electric and magnetic fields. We present an argument that this leads to the cancellation of any large-scale electric fields, and that this implies that the magnetic field is transported bodily with the plasma.

2.3.1 Maxwell's stress tensor

The electromagnetic force (Lorentz force) per unit volume is

$$\mathbf{f} = \rho\mathbf{E} + \mathbf{j} \times \mathbf{B} \tag{2.10}$$

where ρ is charge density, and $\mathbf{j}$ is current density. Using Maxwell's equations (2.2 and 2.5) to replace ρ and $\mathbf{j}$, and some vector calculus, the force per unit volume can be written (see *Griffiths* (1981), p. 351 for full derivation):

$$\mathbf{f} = \nabla \cdot \mathbf{T} - \epsilon_0\mu_0 \frac{\partial \mathbf{S}}{\partial t} \tag{2.11}$$

where $\mathbf{S}$ is the Poynting vector, $\mathbf{S} = (\mathbf{E} \times \mathbf{B})/\mu_0$. The Poynting vector term in Equation 2.11 contains the rate of change of the electromagnetic energy entering the volume per unit area per time. $\mathbf{T}$ is the Maxwell stress tensor. Element ij can be written

$$T_{ij} = \epsilon_0 \left(E_i E_j - \frac{1}{2}\delta_{ij} E^2 \right) + \frac{1}{\mu_0} \left(B_i B_j - \frac{1}{2}\delta_{ij} B^2 \right) \tag{2.12}$$

where $\delta_{ij} = 0$ when $i \neq j$ and 1 when $i = j$. The physical meaning of the force associated with element ij of the stress tensor is the force per unit area (or stress) in the i'th direction, exerted on a surface element normal to the j'th direction. The elements on the diagonal represent electric and magnetic pressure, and the off-diagonal elements are shears. The total electromagnetic force exerted on a volume element can be found by integrating Equation 2.11 over that volume.

2.3.2 The relative strengths of magnetic and electric stress

Equation 2.11 follows from Maxwell's equations, and is therefore exact. It is this force which is to be inserted in Equation 2.9. However, it can be simplified by considering the relative strengths of electric and magnetic stresses in space plasmas. The Poynting vector term will be treated later. A plasma is populated by highly mobile electrically charged particles (a potential difference of one volt will accelerate an electron to 600 km/s). Because of these charges, any electric field which arises, will be rapidly canceled. Therefore, there can be no significant large-scale electric fields in the local frame of reference moving with the plasma. The magnetic field will remain, since there are no equivalent magnetic charges or currents to cancel the magnetic field.

Assume for the moment, that the electric field, $\mathbf{E}'$, in the plasma frame of reference is exactly canceled. It is clear that, in this frame of reference, only the magnetic stress plays a role. Since the plasma velocity in general is far from uniform, this frame of reference is highly irregular, and so we want to calculate the forces in a different coordinate system. To do this, we have to use the Lorentz transformations for the electric and magnetic fields ($v^2/c^2 \ll 1$ is assumed). In a coordinate system in which the plasma is seen to move at velocity $\mathbf{v}$ (all quantities are assumed functions of $\mathbf{r}$ and t), the fields are given by:

$$\mathbf{E}' = \mathbf{E} + \mathbf{v} \times \mathbf{B} \tag{2.13}$$

$$\mathbf{B}' = \mathbf{B} - \frac{\mathbf{v} \times \mathbf{E}}{c^2} \tag{2.14}$$

Assuming $\mathbf{E}' = \mathbf{0}$, the electric field observed from our fixed coordinate system is $\mathbf{E} = -\mathbf{v} \times \mathbf{B}$. In general, the v/c^2 factor in Equation 2.14 does not mean that this term is small compared to $\mathbf{B}$, due to the relative magnitude of the two fields in SI units[2], which is used here. However, in this case, it is true, since by inserting $\mathbf{E} = -\mathbf{v} \times \mathbf{B}$ in the last term of Eq. 2.14 we get $\frac{v^2}{c^2}\mathbf{B}$. This means that $\mathbf{B}$ in conducting plasmas is invariant under non-relativistic coordinate transformations. We also note that the component of the electric field which is parallel to the magnetic field, $E'_{\parallel}$, is also invariant (but here we have assumed this component to be 0).

To compare the magnitude of the forces from $\mathbf{E}$ and $\mathbf{B}$, we see from Equation 2.12 that the electric and magnetic stress scale as $\frac{F_E}{F_B} \sim \frac{E^2}{B^2}\epsilon_0\mu_0 = \frac{E^2}{B^2c^2}$, where $c = 1/\sqrt{\epsilon_0\mu_0} \approx$

[2]This is what *Parker* (2007) refers to as a "grotesque" asymmetry of the SI unit system, whose description as a "practical" he compares to Eric the Red's naming of his icy discovery, Greenland.

3×10^8 m/s is the speed of light. In the case that $\mathbf{E}' = \mathbf{0}$, the ratio of electric to magnetic stress is $\frac{F_E}{F_B} \sim \frac{E^2}{c^2 B^2} = \frac{v^2}{c^2}$, when we use that $E = vB$. We can conclude that, when $\mathbf{E}' = \mathbf{0}$, the electromagnetic forces felt by the plasma are those of magnetic fields, and that electric fields play an insignificant role in the dynamics of a plasma. This is true in any frame of reference moving at non-relativistic speed compared to the plasma.

We also note that, since $\frac{F_E}{F_B} \sim \frac{E^2}{c^2 B^2}$, any $E' \neq 0$ will have to be of the order $c^2 B^2$ for the electric stress to directly affect the dynamics of the plasma fluid. For a magnetic field strength of 5 nT (e.g. the tail neutral sheet), the electric field would have to be 2.25 V/m, which can be regarded as a very strong field in the tail (electric fields in tail reconnection are in the order of $\sim 10^{-3}$ V/m (*Østgaard et al.*, 2005b)). For a magnetic field strength of 10,000 nT (e.g. the distant part of the auroral acceleration region), the electric field would have to be 9 MV/m. Electric fields of this magnitude have never been observed in this region of space (for comparison, the dielectric strength of air is $\sim$ 3MV/m).

2.3.3 Frozen-in magnetic field

The above considerations show that electric fields are negligible as a driving force of convection in space plasmas. However, we have not yet looked at how the plasma and the magnetic field are coupled. Including the magnetic stress in the momentum equation (Eq. 2.9) introduces the magnetic field as a new unknown, and we have to add three new equations to complete the system (assuming an equation of state can be used for the pressure). To do this, we rewrite Faraday's induction law (Eq. 2.3), using Equation 2.13:

$$\frac{\partial \mathbf{B}}{\partial t} = \nabla \times (\mathbf{v} \times \mathbf{B}) - \nabla \times \mathbf{E}' \tag{2.15}$$

With $\mathbf{E}' = \mathbf{0}$, it can be shown (see e.g. *Parker* (2007), p. 93) that Equation 2.15 implies that the magnetic field moves bodily with the plasma. The bulk motion of the plasma does not cross magnetic field lines, and we say that the magnetic field is frozen-in. This is an important conceptual notion, and it is a good approximation almost everywhere in the universe. In the magnetosphere, we assume the magnetic field to be frozen-in everywhere except at shock fronts (e.g. sunward of the magnetopause), in magnetic reconnection (we will describe reconnection later), and in the acceleration region of auroral particles. In these regions, $E' \neq 0$, and $\nabla \times \mathbf{E}'$ can become comparable to $\nabla \times (\mathbf{v} \times \mathbf{B})$. This means that, while electric fields play no direct part in the forces acting on a plasma fluid in space, they can affect how the magnetic field evolves, and thus indirectly affect the plasma dynamics. We will discuss some of the regions in which this happens in Section 2.6.

With $\mathbf{E} = -\mathbf{v} \times \mathbf{B}$, the Poynting vector can be written

$$\mathbf{S} = \frac{1}{\mu_0} (-\mathbf{v} \times \mathbf{B}) \times \mathbf{B} = \frac{1}{\mu_0} \left(\mathbf{v} B^2 - \mathbf{B}(\mathbf{v} \cdot \mathbf{B}) \right) = \frac{B^2}{\mu_0} \mathbf{v}_\perp \tag{2.16}$$

which implies that, in the frame of reference of the plasma, the Poynting vector vanishes. This means that there is no transport of electromagnetic energy relative to the plasma.

The rate of change of $\mathbf{S}$ in a given volume therefore depends on $\mathbf{v}$. Since the Poynting vector term in Equation 2.11 is scaled by a factor of $\epsilon_0\mu_0 = c^{-2}$, this term is small compared to the Maxwell stress tensor as long as $v^2/c^2 \ll 1$.

2.4 Ideal MHD

The result of the above discussion is that the electromagnetic force entering in Eq. 2.9 is dominated by the divergence of the magnetic stress, and we get the following equation for conservation of momentum:

$$nm\left(\frac{\partial v_i}{\partial t} + v_j\frac{\partial v_i}{\partial x_j}\right) = -\frac{\partial p_{ij}}{\partial x_j} + \frac{1}{\mu_0}\frac{\partial}{\partial x_j}\left(B_iB_j - \frac{1}{2}\delta_{ij}B^2\right) \tag{2.17}$$

With the assumption that $\mathbf{E}' = \mathbf{0}$, Equation 2.15 reduces to (in component form)

$$\frac{\partial B_i}{\partial t} = \frac{\partial}{\partial x_j}(B_jv_i - B_iv_j) \tag{2.18}$$

Along with Equation 2.8 and an equation of state to handle the pressure, these equations constitute a full set, describing the large-scale dynamics of space plasmas. This description, which follows from $\mathbf{E} = -\mathbf{v}\times\mathbf{B}$, is called ideal magnetohydrodynamics (MHD). When $\mathbf{E}' \neq \mathbf{0}$, the main modification of these equations appears in Faraday's law, describing the evolution of the magnetic field.

2.4.1 Force balance between thermal and magnetic pressure – plasma β

We now look at an important special case of Equation 2.17, which leads to the definition of a useful plasma parameter, β. Assume that the left hand side of Equation 2.17 is zero ("hydrostatic" equilibrium), that we can neglect the off-diagonal terms in the particle and magnetic stress tensors, and that the diagonal terms are all equal, $p_{ii} = p$, and $T_{ii} = B^2/2\mu_0$ (isotropic thermal and magnetic pressure). Then Equation 2.17 reduces to

$$\nabla\left(p + \frac{B^2}{2\mu_0}\right) = 0 \tag{2.19}$$

which means that under these conditions, the total pressure is uniform. The relative importance of thermal and magnetic pressure defines the plasma β:

$$\beta = \frac{p2\mu_0}{B^2} \tag{2.20}$$

The solar wind is an example of a high β plasma, which is why the magnetic field is being pulled almost radially outward, instead of holding the plasma back. The magnetospheric lobes are examples of low β plasma, in which the magnetic field is in charge of the dynamics.

2.5 Contrasting paradigms

Currents and electric fields do not appear in Equations 2.8, 2.17 and 2.18. Having solved the above set of equations, the electric field and current density can be calculated from Ampere's law (2.5), and from Equation 2.13, respectively. It can be shown that **E** and **j** automatically will satisfy Maxwell's equations when the above procedure is followed (*Parker*, 1996).

For our purpose, the importance of the above discussion is that it sets the premises for how to qualitatively describe the large-scale dynamics of the system. Magnetic stress and plasma pressure should always be the primary suspects when large variations in the magnetosphere are observed. Currents and electric fields are derived quantities. In this paradigm, drawing electrical circuits in order to explain variations in the magnetic field by means of currents, would be to go at the problem in the wrong causal direction.

Despite the apparent simplicity of this approach, and the transparent relations to first principles of physics, it remains controversial. A common view, at least until very recently, is that the electric field drives convection. This view arises, in part, from Equation 2.13, which relates **v** and **E**. While this equation holds in ideal MHD, it does not say what is cause and what is effect. *Vasyliunas* (2001) showed more formally than what has been presented above, that **v** is the cause of **E**, and that an initial **E** is unable to maintain any significant flow of plasma. Later, he showed that in space plasma, **B** generally causes **j**, and not vice versa (*Vasyliunas*, 2005a,b). This view, which is called the **B**, **v** paradigm (in contrast to the **E**, **j** paradigm), has also been elaborated in papers (*Parker*, 1996, 1997, 2000) and more recently in a book by Eugene Parker (2007).

The success of the **E**, **j** paradigm in describing the average behavior of the magnetosphere can be attributed to the fact that the average behavior is approximately a steady state. **v** does not change, and the forces balance. Then, electric fields and currents can be described using circuit theory, and the observed steady velocity will follow. However, if the system changes, so does the current paths, and this approach becomes very difficult. Arguably, the above described approach, in which plasma reacts to forces according to Newton's law, is more intuitive in this case.

The importance of the distinction between **E**, **j** and **B**, **v** can also be said to be more fundamental than choosing the parameters which are most practicable. If **E** can not cause **v** in a space plasma, it becomes absurd to explain convection using electric fields, since it should be the other way around. This should also be considered when qualitatively discussing the cause for observations in near-Earth space.

2.5.1 Excitation of ionospheric convection

One example which illustrates the contrast between treating **E** and **j** as primary variables, and using **B** and **v**, is the excitation of ionospheric convection and currents (*Song et al.*, 2009). The high latitude ionospheric convection is often described as (or modeled as) an effect of an electric field, which maps down to the ionosphere along magnetic field lines, from the magnetosphere. Horizontal currents can then be calculated, using Ohm's

law, $\mathbf{j} = \mathbf{\Sigma} \cdot \mathbf{E}$, where $\mathbf{\Sigma}$ is the conductance tensor. Another approach is to start with field aligned currents, which map down from the magnetosphere, and use Ohm's law to calculate the electric field (and hence convection).

This view has been very successful in explaining and describing various observed phenomena. For instance, Ohm's law gives an intuitive explanation for why regions with high conductance, typically where auroral particles precipitate and in the sunlit part of the ionosphere, are associated with suppressed convection. The high conductance in these regions cancels some of the electric field, and thus reduces the convection. It also explains why these regions are associated with stronger horizontal currents.

However, according to *Vasyliunas* (2005b,a), this approach presupposes stable equilibrium. An alternative approach was adopted by *Song et al.* (2009), who used the equations of motion, and an imposed flow at the top boundary of the ionosphere as the driver of ionospheric convection. The imposed flow creates a force acting on the charged particles, which also experience a resisting force (friction), due to collisions with the neutral constituents in the ionosphere (only $\sim 1\%$ of the particles in the ionosphere are charged). The collision frequency is higher for ions than it is for electrons. Therefore, the friction term is also different, and a single fluid description is no longer appropriate. A coupled system of ≥ 3 equations of motion must be considered, one for each particle species: neutrals, electrons, and each type of ion which is present.

The energy dissipation associated with ionospheric flow is usually expressed as Joule heating, $\mathbf{E} \cdot \mathbf{j}$, in the $\mathbf{E}$, $\mathbf{j}$ paradigm. According to *Vasyliunas and Song* (2005), the energy dissipation is not really Joule heating, but frictional heating, arising from the collisions between the charged particles and the neutrals. According to these authors, it is "largely a coincidence" that the energy dissipation takes the form of $\mathbf{j} \cdot \mathbf{E}$ (with $\mathbf{E}$ in the frame of reference of the neutrals).

We return to a more detailed description of ionospheric convection patterns in Section 5.2.4, and in Section 5.3.2 we discuss how the ionosphere may act back on the magnetospheric driving, and even change the geometry of the magnetosphere.

2.6 Breakdown of ideal MHD

The electric field is not always zero in the frame of reference of the plasma. Localized regions exist where the electric field becomes important, and the frozen-in approximation breaks down. In this section, we look at when this happens. We focus in particular on one important example: Magnetic reconnection. Another example is the auroral acceleration regions, which is discussed in more detail in Chapter 4.

The degree to which ideal MHD holds can be quantified using the generalized Ohm's law (see *Baumjohann and Treumann* (1997) for a derivation of this equation):

$$\mathbf{E} + \mathbf{v} \times \mathbf{B} = \eta \mathbf{j} + \frac{1}{ne}(\mathbf{j} \times \mathbf{B} - \nabla \cdot \mathbf{P}_e) + \frac{m_e}{ne^2}\frac{\partial \mathbf{j}}{\partial t} \tag{2.21}$$

This equation is essentially the momentum equation of the electrons in the frame of reference of the single-fluid plasma. We recognize that it has the same form as Eq. 2.13,

with $\mathbf{E}'$ replaced by the terms on the right hand side. This expression can therefore be used to quantify the electric field, $\mathbf{E}'$, in the rest frame of the plasma. In ideal MHD, $\mathbf{E}' = \mathbf{0}$, and all the terms on the right hand side vanish.

The first term is a resistive term, which can be neglected in most of the magnetosphere (e.g. *Paschmann et al.* (2003), p. 50), but it can become important in the ionosphere. The next term is called the Hall term. It can be neglected when the characteristic scale size, $\Lambda \gg c/\omega_{pi}$, where c/ω_{pi} is the ion inertial length. With $n \sim 0.5$ cm^{-3}, the ion inertial length is ~ 300 km. Scale lengths of this size can be found in reconnection regions, and in the auroral magnetosphere (*Paschmann et al.* (2003), p. 50). In these regions, ions are demagnetized, but electrons are still frozen to the magnetic field. The last terms are the electron pressure tensor, and the electron inertial term. These are the most relevant terms contributing to parallel electric fields (*Paschmann et al.* (2003) p. 52).

We emphasize that the regions in which the terms on the right hand side of Equation 2.21 become significant occupy a very small fraction of the volume of the magnetosphere. In between these regions, where the fields vary smoothly, the MHD description applies, just as hydrodynamics applies to the regions between shock fronts (*Parker*, 1997). This means that MHD can not be used to address e.g., the acceleration of the charges in these regions, but it can predict the locations at which the acceleration occurs.

2.6.1 Reconnection

The concept of magnetic reconnection is illustrated in Figure 2.1 (insertion). The oppositely oriented magnetic field lines moving inwards (thick arrows) form a sharp gradient in the magnetic field, where the frozen-in approximation breaks down. These field lines then merge at certain points, forming what is known as the X-line, because of the X-shaped boundary between incident magnetic flux and plasma and the highly curved field lines which are ejected from the reconnection region (thin arrows). The interior white area denotes a region in which ions are de-magnetized (ion diffusion region), due to the Hall term in Eq. 2.21. In this region, electrons are still frozen to the magnetic field, and will be carried away from the X-line, producing a net transport of negative charge.

The figure also shows two regions in which reconnection can change the topology of the magnetosphere. On the dayside, the interplanetary magnetic field (dashed lines) can merge with the closed field lines of the Earth (solid) to form open field lines (dotted). The momentum of the solar wind then transports the open field lines anti-sunward, and stretch them into a tail, which can extend out to several hundred R_E (Earth radius) on the nightside of the Earth. When open field lines with footpoints in opposite hemispheres meet in the tail, they may reconnect, and form new closed field lines. The X-line in the tail can form both at very high altitudes, $\gtrsim 100R_E$ (distant X-line), and closer to the Earth, at $\sim 20R_E$, in what is called the near Earth neutral line (NENL). In the NENL, reconnection can occur between open field lines, or closed field lines which are stretched. Section 3.1 describes in more detail the consequences of dayside and nightside reconnection for the flow of mass and energy throughout the magnetosphere.

The magnetic field and plasma which is ejected from the X-line has a high velocity

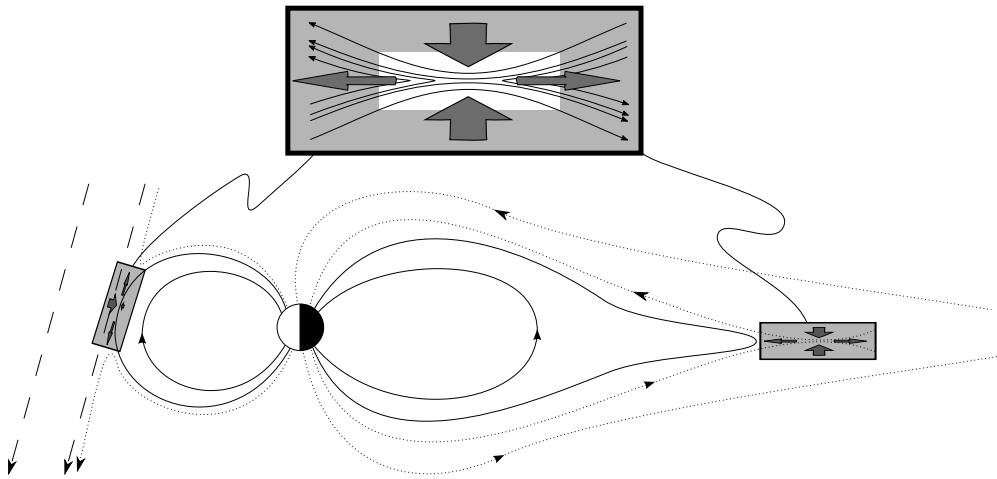

Figure 2.1: Magnetic reconnection shown at two regions in the magnetosphere. On the dayside (to the left in the figure), the interplanetary magnetic field (dashed) merges with closed field lines (solid) of the Earth, producing open field lines (dotted). The open field lines are transported anti-sunward, to the magnetotail. The opposite orientations of the open field lines in the tail enables open field lines to reconnect, forming new closed field lines. The reconnection geometry shown in the insertion illustrates slow (thick arrows) convection of plasma and magnetic field into the X-line (note the asymmetric inflow to the dayside X-line), in which the magnetic field is zero, and fast jets (long arrows) out from the X-line. The interior white region shows where the ions are de-magnetized, due to the sharp gradients in the magnetic field.

($\sim 0.9 v_A$, where v_A is the Alfven speed, $B/\sqrt{\mu_0 nm}$). In-situ measurements of localized regions of high speed plasma are therefore often interpreted as a crossing of these reconnection jets. Another signature of magnetic reconnection observed by spacecraft in the magnetosphere is magnetic perturbations associated with the currents which are implied by the ejection of electrons from the ion diffusion region (e.g., *Snekvik et al.* (2008)).

2.7 Summary

For the present purpose, the key points in the above discussion is that the solar wind-magnetosphere-ionosphere system can be treated largely as a fluid of plasma and magnetic field, which is subject to mechanical forces: Plasma pressure gradients and magnetic stress. $\mathbf{B}$ and $\mathbf{v}$ can be seen as the primary variables, while $\mathbf{E}$ and $\mathbf{j}$ can be derived once $\mathbf{B}$ and $\mathbf{v}$ are known. Of course, if $\mathbf{j}$ and $\mathbf{E}$ are known from measurements (which to some extent can

be true with auroral images), they can be used to make inferences on $\mathbf{v}$ and $\mathbf{B}$, but the physical process leading to these measurements should be described in terms of convection and magnetic field.

The localized regions in which fluid description, and ideal MHD in particular, is not applicable, are of great importance to acceleration of particles and exchange of magnetic flux with the interplanetary magnetic field. These processes facilitate changes in magnetic field geometry, and changes in plasma populations, which then indirectly affects global dynamics.

Chapter 3

Energy and mass flow in the geospace system

In this section we describe the basic constituents of geospace, and look at some important processes governing the flow of mass and energy throughout the system.

Figure 3.1 shows a map of the magnetosphere. Being in a state of perpetual change, this map is at best an average picture. However, the various regions are relatively well-defined, and we will here give a description of the principal processes by which the various regions interact. We also try to keep track of what are the driving processes, and what processes are modulating the driver (feedback). To do this, we take the approach argued in the previous section, that the principal parameters in space plasmas are $\mathbf{B}$ and $\mathbf{v}$.

3.1 The Dungey cycle

When the IMF has a component which is anti-parallel to the geomagnetic field, reconnection can occur between the closed magnetic field lines on the dayside magnetopause, and the IMF. This creates new open field lines which, due to the momentum of the high β solar wind, will be pulled anti-sunward. Since the open magnetic field lines are connected to the Earth, they will be deformed by the anti-sunward motion on higher altitudes, thus forming the magnetotail. In this process, some of the kinetic energy of the solar wind is being converted to magnetic energy, i.e. there is Poynting flux through the magnetopause. The resulting magnetic energy is stored in the lobes, which are regions of highly rarefied plasma ($n \sim 10^{-2}$ cm^{-3}) (*Baumjohann and Treumann* (1997), p. 7), and low β. The lobes are comprised by open magnetic field lines. Being oppositely oriented in the two hemispheres, the implied shear between the two lobes necessitates a cross-tail current, directed from dawn to dusk.

When the lobes are pushed together, reconnection may form new closed magnetic field lines. In this process, magnetic field is annihilated, and magnetic energy is transferred to the plasma, thus producing the high β plasma of the region called the plasma sheet. The newly closed field lines of the plasma sheet are stretched, and the plasma is therefore

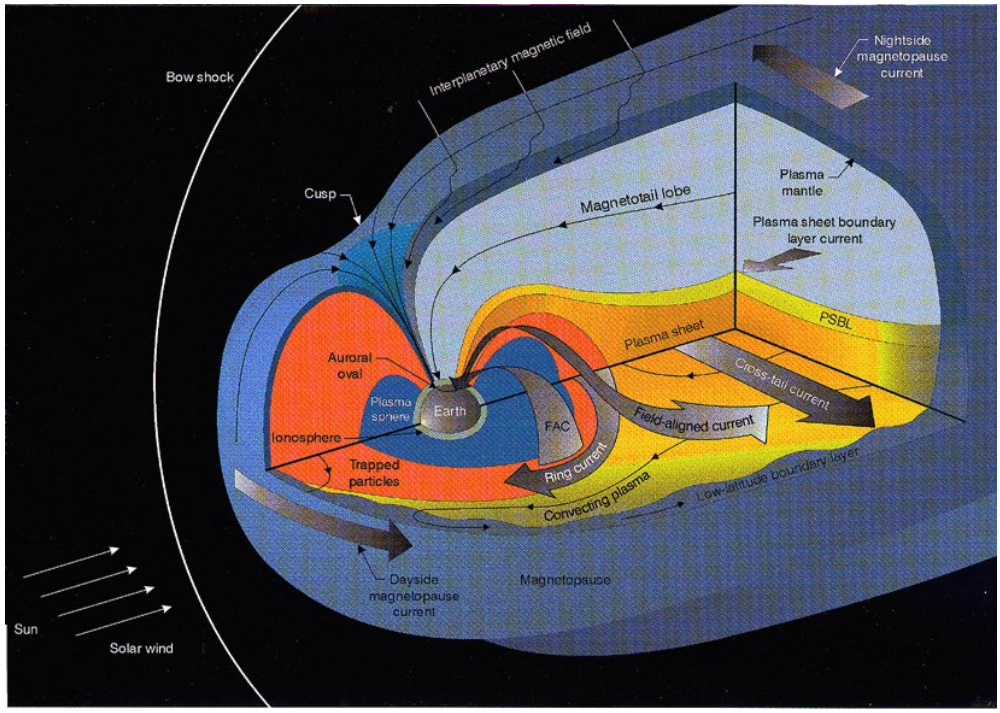

Figure 3.1: Figure showing currents and regions with different plasma populations in the magnetosphere. The *ionosphere*, which consists of a partially ionized, relatively cold and collisional plasma is shown as a thin layer surrounding the Earth. The *plasmasphere* (blue region) consists of co-rotating cold plasma which resides on closed field lines mapping to low latitudes. The *ring current*, whose bulk of energy is carried by energetic ($\sim 10 - 200$ keV) protons, circles the Earth outside (and sometimes interact with) the plasmasphere. The *plasma sheet* is a high-β plasma which maps approximately to the auroral zone. In the tail, it is separated from the low-β plasma of the *lobes* by the plasma sheet boundary layer (*PSBL*). The demarcation between the solar dominated plasma and the region which is dominated by magnetic field lines connected to the Earth, is called the *magnetopause*. The low latitude boundary layer (*LLBL*) and the plasma *mantle* can be seen as the spatial extension of this boundary. Outside the magnetopause is the *solar wind*. A somewhat simpler version of this figure appears in *Kivelson and Russell* (1995), p. 22; the present version is of unknown origin.

subject to magnetic stress (curvature forces), which pushes the plasma towards the Earth. Observations show that the earthward plasma flow takes the form of localized jets, called bursty bulk flows, rather than a large scale, slow convection (*Angelopoulos et al.*, 1994). As the plasma approaches the Earth, it encounters an increased total pressure, which will divert the flow towards the flanks of the magnetosphere. When reaching the dayside, the magnetic flux can once again merge with the IMF, and the above described process can be repeated.

This cycle is called the Dungey-cycle, after the scientist who first suggested its basic principles (*Dungey*, 1961). It is believed to encompass the principal processes responsible for convection of plasma and magnetic flux through the high latitude magnetosphere. The force responsible for the excitation of the convection is magnetic stress and plasma pressure. Reconnection acts simply as a gate opener, changing the topology of the system to allow the magnetic field to relax. The geometry of the reconnection is however of great importance for the geometry of the convection, and hence also for the geometry of the magnetosphere. This will be discussed further in Chapter 5. Several other processes also modulate the cycle, and we will discuss some of them shortly.

Opening of flux on the dayside and closing of flux on the nightside change the total open magnetic flux of the magnetosphere. The ionospheric footpoint of the open flux (the lobes) is called the polar cap. While reconnection only indirectly excites convection, it directly affects the location of the open/closed field line boundary (or polar cap boundary), and the size of the polar cap. Expansion (contraction) of the polar cap therefore signifies flux opening (closure) in excess of closure (opening). Flux closure and opening are quasi-independent processes, since they occur $\sim 30R_E$ (near Earth neutral line) to $> 100R_E$ (distant neutral line) apart. The idea of a quasi-independent expanding/contracting polar cap was suggested by *Siscoe and Huang* (1985), and expanded upon by e.g., *Lockwood et al.* (1990); *Cowley and Lockwood* (1992). This is discussed further in Paper III, where we use auroral images to identify the polar cap boundary. This method is also discussed in Section 4.1.1.

3.2 Different reconnection geometries

The Dungey cycle described above is observed when the IMF has a southward component. When it points northward, the IMF can merge with lobe magnetic field lines. The resulting convection is sunward in the ionospheric polar cap (*Crooker*, 1992). One can also imagine several other geometries in which different kinds of reconnection (and subsequent convection) are important (*Watanabe et al.*, 2007b). However, our main focus is on the Dungey type reconnection, and associated convection, since this cycle is generally believed to dominate the energy transfer from the solar wind to the magnetosphere, and the magnetospheric dynamics during the most active times. It is also worth noticing that, except for the relatively rare case of dual lobe reconnection (small IMF $|B_y|/B_z$ and $B_z > 0$) (*Imber et al.*, 2006), the Dungey-type reconnection is the only one capable of changing the open flux content in the magnetosphere.

3.3 Circulation in the inner magnetosphere

Not directly included in the above description of the Dungey cycle is the circulation in the inner magnetosphere. The plasmasphere is known to co-rotate, albeit not perfectly (*Burch et al.*, 2004), and co-rotation is also a characteristic motion of cold plasma at ring current altitudes. The driving force of the co-rotation comes from below: At low latitudes (to which the forces associated with the Dungey cycle do not usually penetrate) the upper atmosphere rotates with the Earth. Via frictional forces, the ionospheric plasma is brought into the same motion. Since this plasma is frozen to the magnetospheric plasma higher up on the same flux tubes, magnetic stress acts on the magnetospheric plasma until its motion matches the co-rotation.

During periods of particularly strong driving from the solar wind, hot plasma can be injected to the ring current from the plasma sheet, where it can reside for days. These periods are called geomagnetic storms. The energetic particles which carry the ring current undergo gradient and curvature drifts, crossing magnetic field lines. The bulk motion of the single-fluid plasma in the ring current region, on the other hand, does not cross magnetic field lines, since the frozen-in condition still holds there.

In this view, there is a region of the magnetosphere, approximately at ring current altitudes, where the domination of solar wind driving (Dungey cycle) and the more sluggish ionospheric driving (co-rotation) overlap.

3.4 A component view of geospace

In Figure 3.2 we have divided geospace into eight component regions. The arrows indicate how mass and/or energy flows between the various regions, and their labels indicate the process by which this happens. The driving processes in the Dungey cycle and thermospheric winds are both present in the chart. However, from the large number of other interactions, it is clear that other driving processes exist, and that the drivers can be heavily modified by numerous feedbacks. Another process which is thought to be important when the IMF is northward, and can not effectively reconnect with closed field lines on the dayside of the Earth, is viscous interaction (*Axford and Hines*, 1961). Viscous interaction arises from the shear between the solar wind and the magnetosphere, which can trigger instabilities (e.g., Kelvin-Helmholtz), and drive plasma on high latitude closed field lines anti-sunward.

Feedback mechanisms which affect the flow imposed by the driving Dungey cycle processes include i) ionospheric drag, ii) precipitation of particles increasing the ionospheric conductivity, iii) formation of plasmaspheric plumes which in turn affects wave particle interactions, which can increase the precipitation to the ionosphere, and iv) outflow of ionospheric ions (O^+) which can modulate the reconnection efficiency (*Shay and Swisdak*, 2004). These few examples are also interrelated, adding to the complexity. It is clear that the system is highly non-linear, and that a basic qualitative understanding of the global system can not include all eventualities. A common approach is that each observed phe-

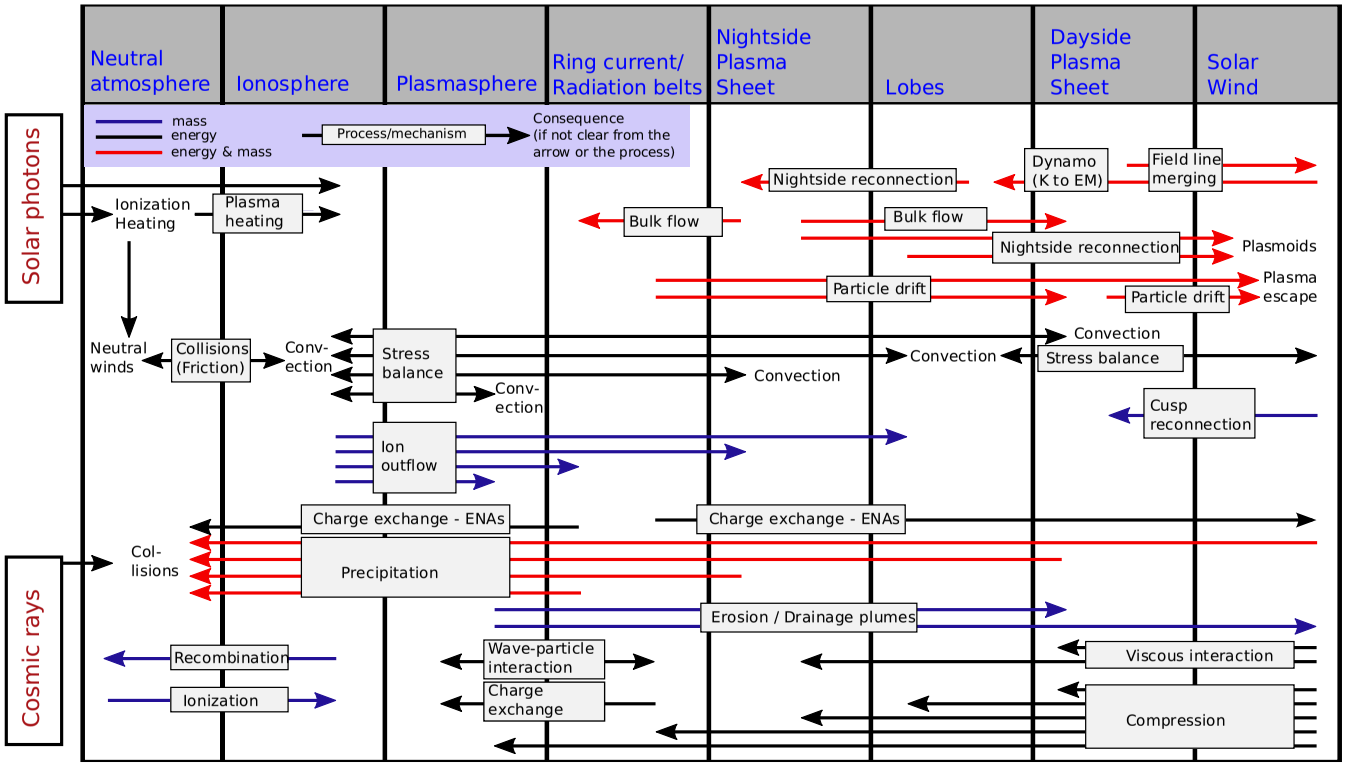

Figure 3.2: Flow chart, showing how mass and energy flow between various regions in geospace. The regions are shown as vertical columns. The flow of mass and energy is from the start to the end of the arrows; arrows crossing a region is not meant to represent flow through that region. The color of the arrow denotes flow of mass and/or energy (see key in upper left corner). The separation into mass and energy is not strictly consistent. One example is ENAs escaping to the solar wind, which represents a significant energy flux, but only a negligible loss of mass. Acronyms: K: Kinetic [energy], EM: Electromagnetic [energy], ENA: Energetic Neutral Atom. This figure was made in collaboration with the System Level Science group at the International Space Science Institute.

nomenon is interpreted in terms of maybe one of the processes in Figure 3.2, believed to be of particular importance.

3.5 The role of substorms

Being an important element in Papers II, III and IV, the role of substorms should also be discussed in the context of global geospace dynamics. Defining and explaining the formation of substorms have been controversial topics the last few decades. We will not attempt a survey of the controversy here, but rather focus on some descriptive aspects of substorms.

In global auroral images, substorms can be identified as a local brightening, followed by an expansion in latitude and longitude, lasting for a few 10s of minutes[1] (*Akasofu*, 1964; *Frey et al.*, 2004; *Gjerloev et al.*, 2008). One example, from 23 June 2000, is shown in Figure 3.3. In this event, the aurora was very faint prior to the onset. Then, at 13:05 UT, a local brightening is observed, and in the subsequent images a longitudinal and latitudinal expansion.

The intensification seen in Figure 3.3 was associated with a contraction of the oval (or equivalently, poleward expansion of the aurora). The contraction signifies a decrease in the open flux in the magnetosphere (see Section 4.1.1). Substorms can thus be seen as a process by which the magnetosphere releases energy, and rids itself with excess open flux through enhanced tail reconnection (*Milan et al.*, 2007). Substorms are relatively frequent, occurring at a cadence of ~ 3 hours during persistent strong solar wind driving (for reasons unknown). The probability of a substorm onset occurring has been shown to increase with the level of open flux (*Boakes et al.*, 2009), and the magnetic flux closure is more significant when the initial level of open flux is higher (*Milan et al.*, 2009a). It should be noted that flux closure is also believed to occur outside of substorm expansion phases, then most importantly by reconnection at the distant neutral line.

The expansion of the aurora from a localized region to a large fraction of the auroral zone reflects processes in the magnetotail. The onset maps approximately to the transition between dipolar field lines and the stretched field lines of the tail. In the subsequent minutes the tail becomes increasingly dipolar, the dipolarization spreading from the onset region to become a global phenomenon. The dipolarization region has been suggested to map to the region of most intense aurora, called the bulge (*Liou et al.*, 2002).

From the description of the Dungey cycle given above, in which reconnection acts as a gate opener for convection, substorm expansion phases are also expected be associated with an increase in convection. This is discussed in Chapter 5.2.4.

[1]The term substorm stems from another substorm signature: A negative perturbation in the horizontal magnetic field seen at ground magnetometers in the auroral zone in the northern hemisphere. These perturbations were long (erroneously) believed to be subgroups of the more long-lasting and global magnetic perturbations which signify geomagnetic storms. Another substorm signature is observations of dispersionless abrupt increase of energetic particles at geosynchronous orbit. However, we will stick to the definition from auroral images.

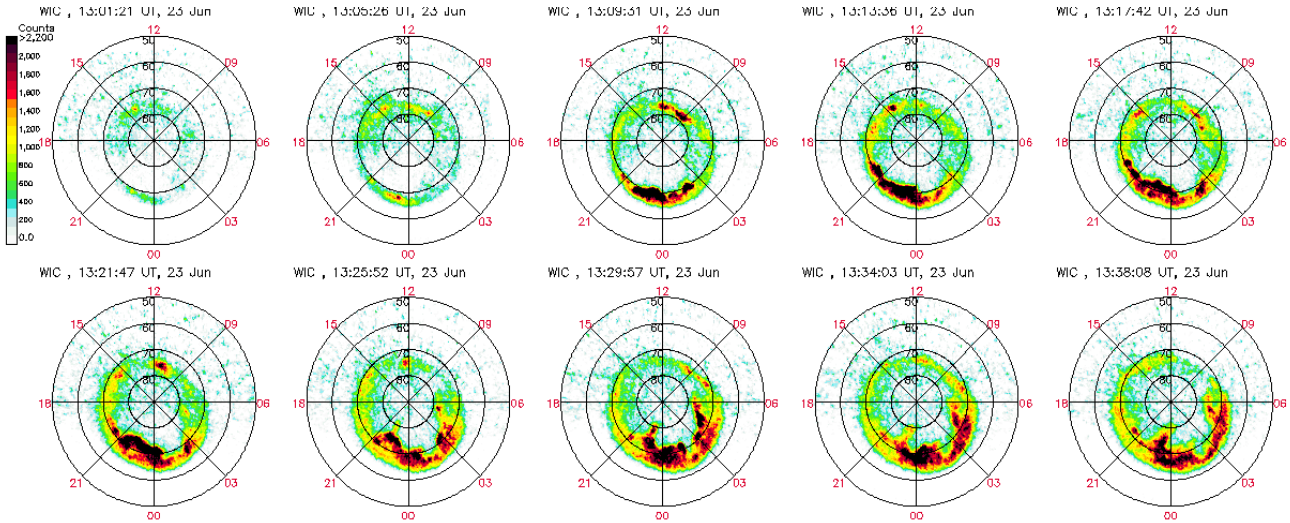

Figure 3.3: Sequence of images, covering ~ 40 minutes, and showing the onset and expansion of an auroral substorm, on 23 June 2000. The onset is seen at 13:05 UT, at 23 MLT. In the next image, four minutes later, the region of bright aurora has expanded to encompass almost six hours MLT. The brightening on the dayside was most likely due to a concurrent increase in solar wind pressure. The images were taken by the WIC camera on the IMAGE satellite.

Chapter 4

The aurora

In this chapter, we look at how auroral imaging can be used as a tracer of magnetospheric dynamics, and in particular how it can be used to estimate the open flux content of the magnetosphere. Then we describe different types of aurora.

It is important to keep in mind that the aurora is not merely an illumination of magnetospheric processes, but also a signature of processes taking place, which modulate the global magnetospheric dynamics. Some examples: 1) Particles producing the aurora also increase the ionospheric conductivity, changing the interaction between the ionosphere and the magnetosphere, and therefore changing the convection in both the magnetosphere and the ionosphere (Chapter 5.3.2). 2) Associated with auroral precipitation is often an upflow of ionospheric ions, which increases the mass content in the magnetosphere, thereby changing the global dynamics. For example, outflow of O^+ ions is believed to affect magnetospheric dynamics in the main phase of geomagnetic storms. 3) The aurora often signifies the existence of parallel electric fields, which are important for particle acceleration. Parallel electric fields also imply that the frozen-in condition no longer holds.

4.1 Mapping to the magnetosphere

For auroral imaging to be used at its full potential, we must know how the precipitating particles relate to source regions and processes in the magnetosphere. Many studies have used auroral features as signs of localized magnetospheric activity. Examples include north-south aligned arcs (streamers) which are interpreted as an ionospheric signature of bursty bulk flows (*Sergeev et al.*, 1999), the cusp spot as a tracer for high-latitude magnetopause reconnection (*Frey et al.*, 2003b), and sudden brightenings signifying the onset of magnetospheric substorms. Several examples of various auroral forms (outside the main oval), and their proposed mapping to magnetospheric processes are found in *Frey* (2007).

4.1.1 Open and closed magnetic field lines

Identifying the magnetospheric regions from which auroral particles precipitate can be done by studying their energy spectra (e.g., *Newell et al.* (2004)). When using UV images, however, this becomes more difficult, since the spectra are generally not known.

However, one region which can often be recognized in UV images of the aurora is the polar cap. This region, which is defined as the ionospheric footpoint of the open magnetic field lines, is largely void of energetic particle precipitation. The low energy precipitation ($\sim$ eV) which can be found there, called polar rain, causes too faint emissions to be observed from global imagers. Just equatorward of this boundary, the precipitation is harder and more intense, causing detectable emissions, which can be used to identify the boundary.

It is however important to be aware that the method for identifying the open/closed boundary also has its problems. First of all, some visible precipitation occurs on open field lines, most notably in the cusp. The cusp is comprised by newly opened field lines, and it borders to precipitation on closed field lines, so that the two regions often are indistinguishable in global UV images. With in-situ particle observations, the cusp can be identified by its lower energies, compared to particles on closed field lines (e.g., *Newell et al.* (2004)).

The perhaps most problematic aspect of using global images to determine the OCB is that the aurora is often faint (e.g., the image prior to substorm onset in Figure 3.3). This might either make it impossible to assess a boundary, or it may produce a wrong boundary. The latter may happen if the precipitation from the center plasma sheet (close to Earth) is intense, while the precipitation from the distant plasma sheet is weak. One example is substorm onset, which maps to a region quite close to Earth, and may be embedded in an otherwise sub-visual auroral oval. Low-altitude in situ particle measurements are much more sensitive than global imagers, and therefore less susceptible to this problem. Comparisons between the open/closed boundaries inferred from these measurements (particle precipitation measured by DMSP in this case), with the boundaries from global UV images, have given credence to the imaging method; *Carbary et al.* (2003) and *Boakes et al.* (2008) found good agreement between the boundaries determined from imaging and in-situ particle observations, but they also identified a systematic bias: On the dawn side, the UV determined boundary was on lower latitudes than the boundaries determined by DMSP, and on the dusk side, the UV boundary was slightly poleward of the DMSP boundaries. This offset could be due to the fact that the field-aligned currents close to the OCB (Region 1) go up at dusk, and down at dawn, and therefore are associated with electron precipitation at dusk and proton precipitation (or at least not high energy electron precipitation) at dawn. This makes the boundary more prominent at dusk, compared to dawn.

4.2 Different types of aurora

In this section we look at different types of aurora. The description given here is focused on the characteristics of the precipitation, without answering why the mechanisms appeared

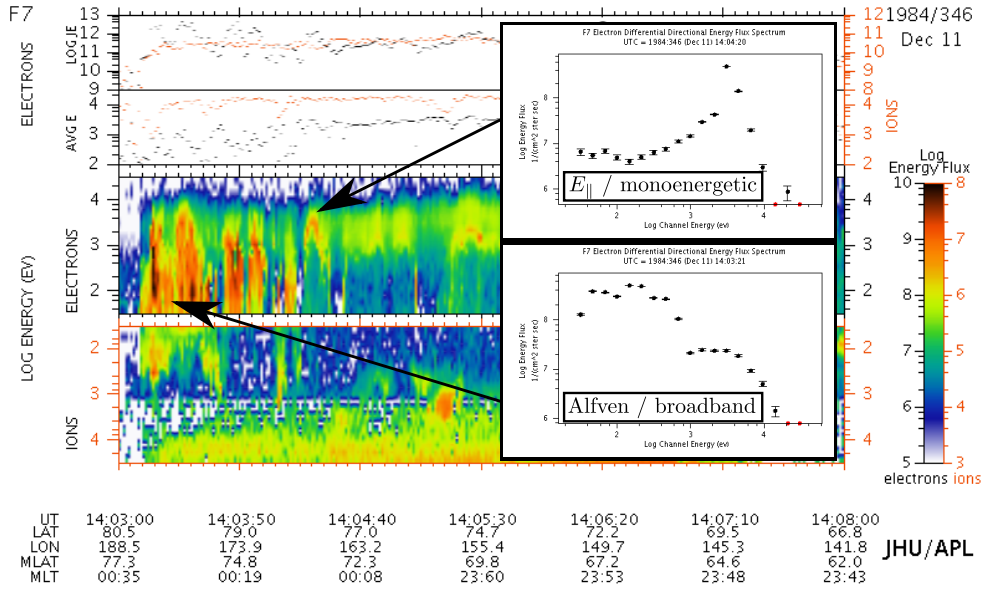

Figure 4.1: Example of a DMSP pass, with in-situ measurements of precipitating electrons and ions. The colors show differential flux in 19 different energy bins, spaced logarithmically. Two kinds of discrete aurora are seen: Alfven wave accelerated, broadband precipitation and monoenergetic precipitation, accelerated by a potential drop parallel to the magnetic field ("inverted V"). Two spectra are shown to illustrate the two types of aurora. Plots from APL website, example from *Newell et al.* (2009).

in the first place: We know that the electrons in an auroral arc can be accelerated by parallel electric fields, but the origin of the parallel electric field is still an active field of research, which we will not go in to here.

4.2.1 Monoenergetic aurora

Low-altitude satellites passing through auroral arcs often observe a monoenergetic spectrum, meaning that a small range of energies dominate completely over other energies. This characteristic is consistent with the electrons having been accelerated by a potential drop somewhere along the field line (*Evans*, 1973). The acceleration region is believed to be at 1000 km up to a few R_E. In some cases, the potential drop tends to gradually decrease away from its maximum, making the spectrogram from a satellite pass display a shape looking like an inverted V (Λ). An example of an inverted V, and a monoenergetic

spectrum is shown in Figure 4.1.

While the dynamics of parallel electric fields is a topic of extensive research, their existence can be shown to be reasonable by a quite simple argument (e.g. *Parker* (1996)). If the flow of plasma creates a curl in the magnetic field, Ampere's law (Eq. 2.5) implies a current and/or a change in electric field. The charges which are to carry the current are subject to Newton's inertia law, and one can presume that this might prevent $\mu_0\mathbf{j}$ to immediately match $\nabla\times\mathbf{B}$. This implies an increase in electric field, in a direction such that the charges are accelerated to increase the current. This explanation is also supported by the observation that parallel electric fields are stronger when the ionospheric conductivity is low (*Newell et al.*, 1996; *Liou et al.*, 2001), which means that the number of available charges is less. Therefore, the charges must be accelerated more to carry the imposed current (see also Section 5.3.4).

4.2.2 Broadband aurora

Another energy spectrum which is often observed in auroral arcs is characterized by a high flux in a broad range of energies. Figure 4.1 also has an example of "broadband" precipitation. *Chaston et al.* (2003) showed that precipitation with this kind of spectrum is associated with electromagnetic Poynting flux, carried by Alfven waves[1] downward towards the ionosphere. Their study showed that broadband precipitation is likely energized by these waves at altitudes between 1 and 2 R_E. Alfven wave aurora often appears in the dayside cusp, and on the nightside, close to the polar cap. These locations indicate a connection between reconnection and the excitation of dispersive Alfven waves.

Newell et al. (2009) showed that the total energy carried by broadband precipitation is very sensitive to solar wind driving, increasing more than other types of aurora. They found that broadband aurora is responsible for a large fraction (28%) of the particle number flux to the ionosphere during active times. Solar wind driving was quantified using a solar wind coupling function: $v^{4/3}B_T^{2/3}\sin^{8/3}(\theta/2)$, where v is the solar wind velocity [km/s], B_T is the IMF magnitude [nT] in the plane perpendicular to the Sun-Earth line, and θ is the IMF clock angle.

4.2.3 Diffuse aurora

Diffuse precipitation is always present, and consists of particles which have not been accelerated in localized regions. It is generated when trapped magnetospheric particles are scattered into the loss cone, or new particles are injected from the tail. Diffuse electrons are scattered primarily by waves, especially by broadband electrostatic waves (*Newell et al.*, 2009). Protons can also be scattered by the stochastic motion that occurs when their gyroradius is comparable to changes in magnetic field. This is typically seen at magnetotail field lines whose apex are highly curved (*Sergeev et al.*, 1983). The latitude separating the

[1] Alfven waves are magnetohydrodynamic waves. They can be pictured as string like oscillations of magnetic field lines.

protons on curved field lines, which precipitate, and protons on dipolar field lines, whose loss cone is empty, is called the isotropic boundary. According to *Mende et al.* (2003b) the equatorward auroral boundary seen by the proton aurora imager on IMAGE, SI-12, possibly coincides with the isotropic boundary.

Newell et al. (2009) showed that the largest fraction of the total precipitating energy (61%) is carried by diffuse electron precipitation, and that the amount of energy which precipitates increases with solar wind driving.

4.2.4 Proton aurora

Electrons carry most of the energy in the night side precipitation, but the proton aurora has been shown to dominate at certain instances (*Frey et al.*, 2001; *Galand and Lummerzheim*, 2004). Even if protons are accelerated in localized regions, the proton aurora will be diffuse. This is because of their large gyro-radius, and because the precipitating protons charge exchange with the neutral atmosphere and become neutral hydrogen atoms, which can move large distances before they become ionized again (and this process can be repeated thousands of times), thus spreading the deposited energy over a large area in the ionosphere. Precipitating protons also produce secondary electrons, which then can excite other emissions. The aurora seen by global UV imagers can therefore not be attributed to electron precipitation alone. In Paper I, we use the IMAGE SI-12 camera, which so far is the only camera that have provided global images of the aurora produced only by protons. We will describe the principle behind this instrument in Chapter 6.1.4, and how it can be used to estimate and subtract the proton contribution to the other cameras in the FUV package.

One of the principal advantages of the SI-12 camera was summed up by *Mende et al.* (2003a): "[...] protons, especially on the nightside, tend to be fairly energetic, with mean energies above 10 keV, and they are only minimally modulated by the field-aligned electric fields which have a fundamental influence on the electron aurora. Therefore, auroral protons are expected to be much better tracers of magnetospheric plasma populations than electrons." Some of the existing studies utilizing the SI-12 camera have focused on the statistical morphology of the precipitation (*Coumans et al.*, 2006), the hemispheric power associated with proton precipitation (*Hubert et al.*, 2002), the statistical behavior of proton aurora during substorms (*Mende et al.*, 2003a,b), and estimates of the oval radius/open flux, due to the low contamination of dayglow in the camera (*Hubert et al.*, 2006; *Milan et al.*, 2009b).

In Paper I, we found that the proton aurora increases when the solar wind dynamic pressure is high. We also presented data from two storm main phases, which showed fundamentally different intensities, possibly because of the large difference in the solar wind dynamic pressure between the two events. An interesting follow-up study would be to look at a larger data set of SI-12 images in relation to solar wind dynamic pressure, and ring current dynamics, manifested by a drop in the SYM-H index (Section 6.4).

Chapter 5

Hemispheric differences

Papers II, III and IV are all concerned with differences between hemispheres inferred from auroral imaging. In Paper II we observe an unusual event in which the intensity of the aurora was very different in the two hemispheres. This was interpreted as an effect of magnetic field aligned currents flowing between the hemispheres. In Paper III, we studied the same event, but with a different approach, looking at spatial asymmetries in the polar cap boundary. These observations led to conjectures about the magnetosphere-ionosphere coupling, which would have implications for all events with rapid flux closure. The statistical study of images in one hemisphere, presented in Paper IV supports some aspects of these findings, but many questions remain.

In this chapter we look at what we mean by asymmetric magnetic field line footpoints. Then we survey previous studies, particularly on magnetic field asymmetries, but we also touch upon studies of convection. We then try to synthesize some mechanisms which are thought to be responsible for the inter-hemispheric asymmetries.

5.1 The meaning of asymmetric field line footpoints

In the context of the Earth's magnetosphere, the footpoints of a magnetic field line are asymmetrical if the two points are not part of the same International Geomagnetic Reference Field (IGRF) line. The IGRF is a model of the magnetic field which is generated in the Earth's interior, and it represents what the Earth's magnetosphere would look like in the absence of external influence, primarily from the solar wind and IMF. Not all types of external forcing produce asymmetric field line footpoints. An obvious example is the magnetotail, which is always present, but generally does not affect the symmetry of field line footpoints. A measured inter-hemispheric asymmetry signifies a perturbation of the IGRF which is not balanced in the opposite hemisphere.

To quantify asymmetries, it is clear that we need a coordinate system which is based on the IGRF. Such coordinate systems are Apex coordinates (*VanZandt et al.*, 1972; *Richmond*, 1995) and the Altitude Adjusted Corrected Geomagnetic (AACGM) coordinates (*Baker and Wing*, 1989).

5.1.1 The Apex coordinate system

In the papers in this thesis, we primarily use the Apex coordinate system. Consider a point at some given altitude above the surface of the Earth, given in geographic coordinates. To find the Apex coordinates of this point, we start tracing along the IGRF magnetic field line, until we reach the point that lies at the highest altitude above the earth (the slightly spheroidal shape of the Earth is taken into account). This point is the apex of the field line. Its radius (in R_E), A, is

$$A = 1 + \frac{h_A}{R_{eq}}, \tag{5.1}$$

where h_A is the apex altitude, and R_{eq} is the equatorial radius of the Earth. The apex latitude is then defined by

$$\lambda_A = \pm cos^{-1} A^{-\frac{1}{2}}. \tag{5.2}$$

This equation is the relation between the equatorial distance to a dipole magnetic field line (in this case the distance is A), and the latitude of its intersection with a unit sphere. The plus (minus) sign corresponds to the northern (southern) hemisphere. The geomagnetic dipole longitude[1] of the apex defines the apex longitude, ϕ_A. This definition ensures that points which trace out to the same apex, and thus belong to the same field lines, get symmetrical coordinates in the two hemispheres. This definition depends on altitude: Points which are on the same geographic longitude and latitude, but at different altitudes will get different magnetic coordinates. For the auroral images in this study, an altitude of 130 km was used.

The other much used coordinate system, AACGM, is defined in a similar way: Instead of tracing to the field line apex, the tracing stops at the geomagnetic dipole equatorial plane. Both coordinate systems are shown on geographic coordinates in Figure 5.1, AACGM in black and Apex in red. The deviation between the two systems is less than the uncertainty in pixel localization in global auroral imagers.

5.1.2 Effects of the non-uniform magnetic coordinate system

Several interesting phenomena can be understood by inspecting the mapping between magnetic and geographic coordinates revealed by Figure 5.1. In the absence of asymmetries, corresponding grid cells in the two hemispheres are ionospheric mappings of the same magnetic field lines, or flux tubes. Since the sizes of conjugate grid cells may be different, precipitating particles can be spread over a larger geographic area in one hemisphere, leading to a difference in particles per unit area, and hence auroral intensity. However, this effect is countered by the stronger magnetic field, and thus mirror force, in the hemisphere with the smallest area. In the case of inter-hemispheric asymmetries in magnetic field

[1] The geomagnetic dipole longitude is measured eastward of the western hemisphere half of the meridian connecting the *centered* dipole poles and the geocentric poles. A nice overview of magnetic coordinate systems, but especially the AACGM, is found in the pdf presentation file by K. Baker at http://superdarn.jhuapl.edu/tutorial/Baker_AACGM.pdf

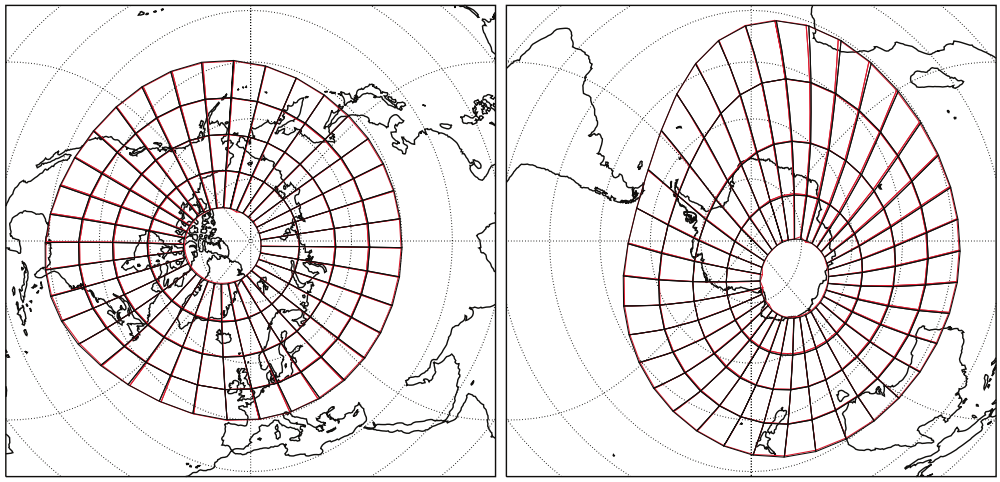

Figure 5.1: The figure shows the apex (red) and AACGM (black) coordinate systems mapped to geographic coordinates. Shown are circles of magnetic latitude at 40, 50, 60 and 80 degrees. The magnetic meridians are separated by 10 degrees magnetic longitude. The difference in total area enclosed by the apex and AACGM coordinate boxes is $\approx 0.5\%$ of the total area.

line footpoints, the corresponding grid cells in the two hemispheres will shift, and the effect of the non-uniform coordinate system can increase or decrease. Note that, due to the magnitude of the magnetic field on low altitudes, a shift in the field line footpoint is almost exclusively due to perturbations on high altitude.

The non-uniformity of the magnetic coordinate system, seen from a geographic coordinate system, may become important when comparing measurements which are ordered by the two different coordinate systems. Three examples are: 1) Studies which relate the solar illumination in the ionosphere, which is ordered by geographic coordinates, to phenomena which are ordered by magnetic coordinates, such as the onset location of substorms. 2) Dynamics of high latitude ionospheric convection: The friction and the effective inertia of the ionosphere should be higher in large grid cells (i.e., the size of the magnetic grid in geographic coordinates), since they contain more mass, while the forces driving the convection might be better ordered by a magnetic coordinate system. 3) Studies of the transition regions between plasma which is controlled by the co-rotation of the ionosphere, and plasma which is controlled by the interaction with the IMF.

One can also imagine, by looking at Figure 5.1, that the frequency of phenomena that are ordered by magnetic coordinates, e.g. substorm onsets, are longitude dependent when sorted by geographic coordinates. This is because these phenomena are spread out in a larger geographic area in large grid cells, compared to the smaller grid cells on the

same latitude, while each cell has the same number of events. A more curious effect of the irregular magnetic coordinate system is that the resolution of auroral images, when plotted in magnetic coordinates, depends on the low altitude magnetic field strength: Since the pixels are evenly spread out in geographic coordinates (on average), the large grid cells (weak magnetic field) will contain more pixels.

5.2 Previous observations of inter-hemispheric asymmetries

Here we give a review of some of the previous works reporting observations of inter-hemispheric asymmetries. A summary of some suggested causes for inter-hemispheric asymmetries is given in Chapter 5.3.

5.2.1 Simultaneous auroral images

Table 5.1 contains a list of conjugate studies of the aurora, using imaging. In the following, we summarize the findings of the works which are most relevant to the papers in this thesis. We focus on studies using imagers, although conjugate studies of the auroral zone have also been carried out using magnetometers (review by *Wescott* (1966)), riometers (e.g., *Hargreaves* (1969)), X-ray detectors carried by balloons (e.g., *Anderson et al.* (1962)), scanning photometers (*Sato et al.*, 1986), and in-situ particle detectors in one hemisphere combined with imaging in the other (e.g., *Vo et al.* (1995)).

Ground all-sky cameras: The first optical study of the aurora in both hemispheres simultaneously was conducted by *DeWitt* (1962). Using all-sky cameras in Alaska and in the south Pacific, in geomagnetically conjugate regions, he confirmed what was expected at the time, that the auroral shapes, motion, and variation in intensity was similar in the two hemispheres. Further confirmation was provided that same year, by *Anderson et al.* (1962), who detected very similar coincident X-ray fluxes from balloons flying at approximately conjugate points.

The advantage of using all-sky imagers for conjugate studies is that they can have a much better time resolution than the cameras which so far have been carried by satellites. Their proximity to the auroral emissions also enables all-sky cameras to resolve fine structures in the aurora. A pair of stations in Syowa in Antarctica and in Iceland have been used for conjugate observations for three decades, utilizing both scanning photometers (*Sato et al.*, 1986) and all-sky imagers. Ground based auroral studies require darkness and clear skies, minimal interference from moon light, and of course, auroral activity. Because of these requirements, conjugate ground based observations can only be conducted during equinox, when both hemispheres are in darkness. Excellent conditions were prevalent during an event presented by *Sato et al.* (1998), enabling a number of detailed comparisons between the hemispheres. In the course of only a few minutes,

Authors	Northern hemisphere	Southern hemisphere
(*DeWitt*, 1962) (*Bond*, 1969) (*Sato et al.*, 1998, 2004, 2005) (*Fujii et al.*, 1987) (*Watanabe et al.*, 2007a) (*Minatoya et al.*, 1996)	Ground ASC	Ground ASC
(*Belon et al.*, 1969) (*Stenbaek-Nielsen et al.*, 1972, 1973) (*Stenbaek-Nielsen and Otto*, 1997)	Airplane ASC	Airplane ASC
(*Burns et al.*, 1990)	Ground ASC	Viking
(*Craven et al.*, 1991) (*Pulkkinen et al.*, 1995)	DE-1	Viking
(*Frey et al.*, 1999) (*Vorobjev et al.*, 2001)	Polar UVI	Ground ASC
(*Fillingim et al.*, 2010)	Ground ASC	Polar UVI
Frank and Sigwarth (2003)	Polar VIS Earth	Polar VIS Earth
Zhang et al. (2006)	TIMED/GUVI	IMAGE FUV
(*Østgaard et al.*, 2003, 2004, 2005c,a, 2007) (*Stubbs et al.*, 2005) (*Fillingim et al.*, 2005) Paper II, Paper III	IMAGE FUV	Polar VIS Earth/ UVI

Table 5.1: Overview of inter-hemispheric studies of the aurora, using imagers (ASC = all-sky camera). A few early studies in conference proceedings and monographs have been omitted.

they observed conjugate aurora with larger scales in the southern hemisphere (also when accounting for the IGRF mapping, shown in Figure 5.1), arcs showing excellent conjugacy, and a non-conjugate auroral breakup in the southern hemisphere. Comparing the travel times of Alfven waves between the hemispheres to their observation of a one minute delay between auroral breakups in the two hemispheres, they suggested that the triggering source of the auroral breakup was located near the ionosphere. A later study (*Sato et al.*, 2005) reported another event with very similar auroras observed in both hemispheres. In this event however, they observed corresponding auroral features to move relative to each other, ~ 200 km in longitude and ~ 50 km in latitude, during the course of one hour. This motion seemed to be independent of concurrent changes in the IMF. They suggested that the change in conjugate points was due to asymmetrical field aligned currents in the two hemispheres. In light of the discussion in Paper III, we may add that these asymmetries could also have been an effect of field aligned electric potential drops or by differences in ionospheric convection (see also Chapter 5.3.3).

All-sky cameras on airplanes: Conjugate observations of the aurora have also been conducted from airplanes. *Belon et al.* (1969) reported data from three flights along conjugate segments of a magnetic meridian in 1967. The conjugate images showed remarkable good dynamical and spatial conjugacy. Tracing arcs from the southern hemisphere, along a realistic model of the Earth's magnetic field (similar to the IGRF), onto the northern hemisphere, the arcs proved to be nearly coincident. These flights were done during magnetically quiet periods, but later flights, when the magnetic activity was high, contained events in which bright aurora appeared exclusively in one hemisphere. This disturbed event was later studied in more detail by *Stenbaek-Nielsen et al.* (1972), who concluded that the observations either implied that the aurora was non-conjugate, or that it was displaced from its counterpart in the opposite hemisphere by more than 1000 km. At auroral latitudes, this corresponds to a displacement of approximately 20° longitude, or $\approx$1.3 h MLT, which we now know is high, but not unheard of (*Østgaard et al.*, 2004).

A substantial result from the flight campaigns was that the inter-hemispheric displacement seemed to be stronger, and more transitory on higher latitudes. During the course of a substorm (as evidenced by a magnetic bay), the relative displacement was seen to change signs. On lower latitudes, *Stenbaek-Nielsen et al.* (1972) reported a stable arc system, which consistently showed a large degree of symmetry. *Stenbaek-Nielsen et al.* (1973) looked at intensity differences between hemispheres, and found that in all the flight observations, the equatorward arc was more intense in the northern hemisphere. At the longitude of the flight paths, the magnetic field is stronger in the southern hemisphere, which increases the mirror force there, preventing precipitation (see Section 5.3.4).

In a later paper, *Stenbaek-Nielsen and Otto* (1997) revisited the aircraft measurements, and argued that some of the observations, showing large inter-hemispheric variations in the distance between the equatorward arcs and poleward arcs, could not be reasonably explained in terms of spatial displacement. They offered a new interpretation, that some of the poleward arcs were in fact non-conjugate, and that the non-conjugacy arises from an

inter-hemispheric current. The inter-hemispheric current was suggested to be caused by a partial penetration of the IMF B_y component into the magnetotail. They argued that this penetration is lower at the earthward and tailward ends of the plasma sheet, implying two shears, or currents. For a positive B_y, the direction of these predicted inter-hemispheric currents would be from the northern to the southern hemisphere at the earthward end (presumably modifying the Region 2 current system) of the penetration region, and from the southern to the northern hemisphere at the tailward end (modifying the Region 1 current system). A more detailed description of inter-hemispheric currents is given in Chapter 5.3.4.

Ground all-sky and Viking: *Burns et al.* (1990) compared keograms derived from cameras at the South pole station, and from the Viking satellite in the northern hemisphere, during northern summer season. During the three events studied, they found that conjugate points were displaced up to 1.9 hours MLT, and 5.3° latitude. During one of the events, they observed the southern aurora to propagate further towards the pole than the aurora in the north. Given the similar seasonal conditions and type of asymmetry, this could represent the same kind of asymmetric poleward propagation reported in Paper III.

Viking and DE: The first purely space based opportunity for conjugate studies of the global aurora came with the launch of the Swedish satellite, Viking, in 1986. At this time, the Dynamics Explorer 1 was already in orbit, and both these satellites carried instruments which could observe the global UV aurora. Using these instruments, *Pulkkinen et al.* (1995) studied a substorm observed in both hemispheres. Similar features were observed, and the mapping of the auroral luminosity to the tail showed consistent results between the hemispheres.

Ground all-sky and Polar: *Frey et al.* (1999) and *Vorobjev et al.* (2001) used the UVI instrument on Polar together with ground all-sky cameras in Antarctica to study conjugate auroras. *Vorobjev et al.* (2001) focused on the poleward boundary of the aurora, in relation to the orientation of the IMF. They found that this boundary could be displaced by up to 5° latitude. Observations from 10 time intervals showed the night side aurora to be located on higher (lower) magnetic latitudes in the northern hemisphere when the IMF was in the $B_x < 0, B_y > 0$ ($B_x > 0, B_y < 0$) Parker spiral sector, compared to the aurora in the southern hemisphere. This displacement is in accordance with magnetic field perturbations on the nightside in the same direction as the IMF (see Figure 5.2).

Polar only: *Frank and Sigwarth* (2003) reported conjugate observations of a substorm using a single camera, VIS Earth on the Polar satellite. At the time of this event (1 November 2001), Polar had its apogee close to the geographic equatorial plane, on the nightside of Earth, and the large field of view of the VIS Earth camera enabled simultaneous observations of the nightside auroral zone in both hemispheres. The onset of the substorm occurred with a displacement of $\sim$ 40 minutes of local time. The intensity of the aurora

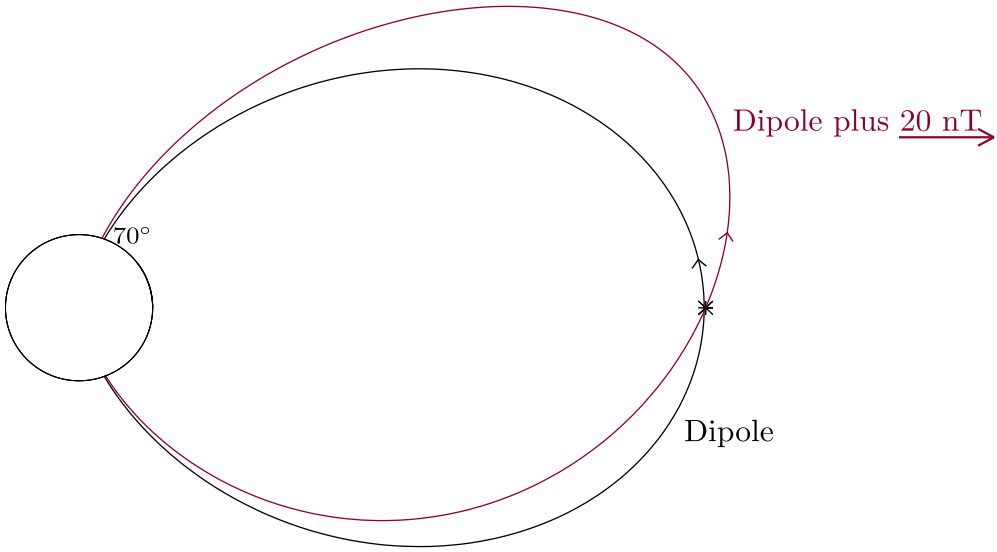

Figure 5.2: A dipole magnetic field line (using the dipole moment of the Earth, 8.05×10^{22} Am^2 (*Baumjohann and Treumann* (1997), p. 32)), intersecting the Earth surface at 70° latitude (black), and the field line of a dipole plus a 20 nT uniform field towards the right in the figure (red). The tracing of the "dipole plus uniform field"-line, using the Runge-Kutta-Fehlberg method with adaptive stepsize, was started at the crossing of the equatorial plane (asterisk). Its footpoints are displaced poleward in the northern hemisphere, and equatorward in the southern hemisphere, compared to the dipole field line. In this figure the dipole field line is in the same plane as the perturbation field, resulting in a latitudinal asymmetry. In all other cases, the perturbation field will produce a longitudinal asymmetry as well.

was also reported to be higher in the southern hemisphere. Since the southern hemisphere had summer in this event, the asymmetry in the intensity is opposite to what has been found in statistical studies of seasonal effects (described later in this chapter).

Polar and IMAGE: While still a scarce data set, the best global coverage of the aurora in the two hemispheres was provided by the IMAGE and Polar satellites. On a few occasions, primarily in the first years of the IMAGE mission, 2000 to 2002, the constellation of these satellites was such that both hemispheres could be observed simultaneously, at an unprecedented spatial and temporal resolution. *Østgaard et al.* (2004) identified 12 auroral forms which could be seen in both hemispheres, and showed that these forms were displaced in longitude, depending on the orientation of the IMF, in the yz plane. The displacement

was consistent with a partial penetration of the IMF to the magnetosphere. In a later study, *Østgaard et al.* (2005c) showed that the observed displacements were an order of magnitude stronger than the displacement predicted by the Tsyganenko 96 and 02 magnetic field models (*Tsyganenko* (2002) and references therein). They also found indication that the dipole tilt angle may act as a secondary controlling parameter, displacing the winter hemisphere footpoint dawnward compared to the summer hemisphere footpoint.

Stubbs et al. (2005) were the first to use these satellites to study the time development of inter-hemispheric asymmetries, during a 1.5 hours interval. Using a circle fitting technique, similar to *Holzworth and Meng* (1975), they found that the center of the ovals changed in step with concurrent variations in the IMF, in agreement with the "dipole plus uniform field" picture described by *Cowley et al.* (1991), shown in Figure 5.2. They also found that the ovals in both hemispheres were displaced towards dawn.

Fillingim et al. (2005) used the UVI camera on the Polar satellite, during an event when this camera observed the southern hemisphere afternoon sector while IMAGE WIC observed the northern hemisphere. They found that in the southern hemisphere, the afternoon aurora was structured, showing a "string of pearls" configuration, while the afternoon aurora in the northern hemisphere was more uniform. Because of modest seasonal differences, the most likely cause for this inter-hemispheric difference was the positive IMF B_y. Positive B_y is often associated with a crescent shaped convection cell at dusk in the southern hemisphere, and a round cell in the northern hemisphere. *Fillingim et al.* (2005) proposed that the stronger flow shears, and associated field-aligned currents in the southern dusk sector was the cause for the different morphology of the afternoon aurora.

5.2.2 Statistical studies of one hemisphere

Because of the relatively few truly conjugate observations, most of our quantitative knowledge about inter-hemispheric asymmetries stems from observations from only one hemisphere. To investigate the effect of IMF B_y, B_x and dipole tilt angle, such studies require a large number of measurements. To infer about instantaneous inter-hemispheric differences, one must assume that the northern hemisphere reacts to positive B_y, B_x and dipole tilt angle, in the same way as the southern hemisphere reacts to negative B_y, B_x and tilt, respectively.

Auroral morphology

Holzworth and Meng (1984) employed auroral images from a DMSP satellite to study the polar cap boundary in relation to the IMF orientation. Using a technique described by *Holzworth and Meng* (1975) they fitted the observed points of the polar cap boundary to a circle. The center of the circle in the southern hemisphere was observed to be displaced towards dusk (dawn) when $B_y > 0$ ($B_y < 0$), by 1° per 2 nT B_y. They also observed a shift of the center in this circle, independent of the IMF, $\sim 5°$ tailward, in agreement with an earlier study of a subset of the same data, by *Meng et al.* (1977). The B_y dependent dawn-dusk shift was later pointed out by *Cowley et al.* (1991) to be consistent with the

IMF creating a global perturbation to the geomagnetic field in the same direction as the IMF, the "dipole plus uniform field" picture. Figure 5.2 illustrates this concept, for a dipole field line in the same plane as the perturbation field.

Later, *Oznovich et al.* (1993) showed, using UV images of the aurora from the Polar BEAR satellite, that the auroral oval is displaced further towards midnight in the summer hemisphere, compared to the winter hemisphere. The displacement at noon and midnight was approximately 1° per 10° tilt angle.

Elphinstone et al. (1990) used images from the Viking satellite, in conjunction with IMP-8 measurements of the IMF, during times when the IMF B_z was positive. Among other findings, they concluded that in the northern hemisphere, the polar cap was displaced towards dawn (dusk) when $B_y > 0$ ($B_y < 0$), consistent with the findings of *Holzworth and Meng* (1984).

The repeating pattern of auroral substorms make them ideal for statistical studies of the IMF influence on the aurora. *Liou et al.* (2001) used observations of 648 substorm onsets, observed by Polar UVI, to study how their average location is affected by the IMF and by seasons. They found that the average location of substorm onsets is 22:30 MLT, and 67° magnetic latitude. When the IMF $B_x > 0$ ($B_x < 0$), the average onset location is shifted equatorward (poleward). They also found that, when keeping $|B_x| < 1$ nT, the average location of substorm onset is shifted westward in the northern hemisphere when the IMF $B_y > 0$, and eastward when $B_y < 0$. These shifts in average onset locations are consistent with a perturbation of the magnetic field in the direction of the IMF. They also found that when separating the substorms according to seasons, the onset on average occurs ~ 1.5 hours dawnward (closer to midnight) during winter, compared to summer.

Several similar studies have later been undertaken, based on observations of substorm onsets by the IMAGE FUV instrument. The basis for these studies is a list of more than 2400 onsets and their locations, compiled by *Frey et al.* (2004). Their list has later been expanded to include 4193 substorms from the whole IMAGE mission life time (*Frey and Mende*, 2006). Using this list, *Østgaard et al.* (2007) showed that the average MLT of the onset depends on the clock angle of the IMF. This result was contested by *Wang et al.* (2007), who, using the same data set, found that B_y exercises a better control over the onset location, than the clock angle. *Wang et al.* (2007) did not find evidence for inter-hemispheric differences in the latitude of the substorm onset, in contrast to the *Liou et al.* (2001) study. Not surprisingly, both *Liou et al.* (2001) and *Wang et al.* (2007) found that the latitude of the onset moves equatorward with an increasingly negative IMF B_z, presumably because this enhances the dayside reconnection, opening more flux, and consequently expanding the auroral oval. However, this effect is expected to occur in both hemispheres.

We note that the correlation between the onset MLT and the solar wind B_y is low: For the 4089 substorms in the *Frey et al.* (2004) list for which ACE data is available (see Paper IV), the correlation is only -0.19 (reversing the sign of B_y for observations in the southern hemisphere). This is significant (the chance of it being random is less than 0.01%), but it also means that a linear relation between B_y and the onset MLT can only explain $\approx 4\%$ of the variation in onset location. A natural interpretation of this, is that B_y does not

affect where in the magnetospheric equatorial plane the onset occurs, but it does affect the geometry of the field, and hence the mapping to the ionosphere.

Auroral intensity

The precipitation power, as well as the mean energy of the precipitating particles, can also vary between hemispheres. *Newell et al.* (1996) used DMSP electron energy spectra in a statistical study investigating the relation between electron energy and the degree of solar illumination in the ionosphere. They found that the probability of observing monoenergetic particle precipitation (electrons accelerated by parallel electric fields) is significantly higher when the ionosphere is in darkness. *Liou et al.* (2001), using the ratio of different passbands in the UVI imager, confirmed that on the night side, the average energy of precipitating electrons, as well as the total energy flux, is higher in darkness (by a factor of ~ 3). On the dayside however, the energy flux is higher in summer, by a factor of ~ 2. *Coumans et al.* (2004), using the SI-12 imager on IMAGE, showed that proton precipitation shows a generally opposite dependence on seasons, compared to electrons. The different dependencies for electrons and protons reflect the proposed seasonal dependence of parallel electric fields.

In a more recent study, by *Newell et al.* (2010), the seasonal dependencies of the various types of aurora were investigated. They found that the monoenergetic aurora is most dependent on seasons, with the nightside power being a factor of 1.7 higher during winter than during summer, when the solar wind driving (see Chapter 4.2.2) is strong. The Alfven wave aurora and diffuse electron aurora also show a seasonal dependence, with factors of of 1.26 and 1.3 higher power in winter. On the dayside, the electron auroral power is generally higher in the summer hemisphere, although the differences are less pronounced.

The orientation of the IMF has also been reported to cause intensity variations which are expected to be different in the two hemispheres. *Liou et al.* (1998) reported a significant increase in the auroral intensity, measured by Polar UVI, on the nightside in the northern hemisphere, when B_y is strongly negative. *Liou et al.* (1998) (and references therein) also showed that in the afternoon sector in the northern hemisphere, the aurora is more intense when B_x is negative. Later, *Shue et al.* (2002), who also used the UVI instrument, showed that the global auroral power in the northern hemisphere is higher when B_x is negative.

5.2.3 In-situ measurements of the magnetic field

In-situ observations confirm that the IMF B_y is associated with a similarly directed magnetic perturbation on closed field lines. *Wing et al.* (1995) studied 5 and 6 years of magnetic field measurements from the geo-stationary satellites GOES-6 and GOES-7 in relation to the y component of the IMF, measured by the IMP-8 satellite. B_y at geostationary orbit was found to be well correlated with B_y in the solar wind at all local times. Maximum correlation was found at midnight and at noon. However, the slope of the regression lines between the two variables had a minimum at midnight, increased towards the flanks and reached maximum on the dayside. This means that variations in the nightside magnetic

field are more sensitive to IMF B_y, but the amplitude of the variation, or degree of penetration, is stronger on the dayside.

The IMF orientation also affects the magnetic field further downtail (*Fairfield*, 1979). *Tsurutani et al.* (1984) showed that in the distant tail ($150 - 238R_E$ downtail), B_y in the north-dawn lobe and in the south-dusk lobe was correlated with positive IMF B_y. Practically no correlation with positive IMF B_y was found in the two other lobe quadrants. For negative IMF B_y, the situation was the opposite, with correlation between IMF B_y and north-dusk and south-dawn lobe B_y. The same asymmetry in lobe susceptibility to IMF B_y was later reported by *Khurana et al.* (1996), who presented measurements from $x = 43 - 87R_E$ downtail.

In a recent study, *Petrukovich* (2009) used 11 years of Geotail data from $|Y_{GSM}| < 15R_E$, and $-31R_E < X_{GSM} < -8R_E$, and found that B_y in the tail increases with increasing tilt angle (the northern hemisphere increasingly tilting towards the sun), after having subtracted the effect of the IMF. That is, during northern summer, the tail B_y is more positive, and during winter, it is more negative. This effect seemed to decrease with increasing distance from the Earth. One possible source for this is the shift in position of the sunlight terminator in the ionosphere. This connection is suggested by theoretical works (see Chapter 5.3.2), and studies of convection which are reviewed below.

5.2.4 Inter-hemispheric differences in ionospheric convection

As argued in Chapter 2, the magnetic field and plasma are frozen-in in most of the magnetosphere. Since the magnetic field moves with the plasma, we expect asymmetries in the the magnetic field to be closely linked to asymmetries in the convection. With very few exceptions, all empirical knowledge about global magnetospheric convection stems from measurements of the convection in the ionosphere. Here we briefly review some of the numerous studies that have been conducted of ionospheric convection patterns, and how these change with different seasons and the sign of IMF B_y when $B_z < 0$.

One of the first documented effects of different signs of the IMF B_y is that Hall currents in the high-latitude dayside ionosphere tend to flow eastward when $B_y > 0$ and westward when $B_y < 0$. This is called the Svalgaard-Mansurov effect (*Svalgaard*, 1968; *Mansurov*, 1969). Since the collision frequency with the neutral atmosphere is higher for ions than for electrons, ionospheric convection sets up these Hall currents in the opposite direction of the convection (the direction of the positive ions relative to the electrons). The Svalgaard-Mansurov effect is therefore equivalent to westward convection on the dayside during $B_y > 0$ and eastward convection when $B_y < 0$.

Statistical studies of average convection

Global convection patterns, derived from statistical ensembles of various measurements, have confirmed these findings. *Heppner and Maynard* (1987) and *Weimer* (1995) used DE-2 measurements, *Papitashvili and Rich* (2002) used DMSP, *Ruohoniemi and Greenwald* (2005) used SuperDARN radar measurements, and *Haaland et al.* (2007) used mea-

surements from Cluster. The latter study was the first to derive global convection patterns from measurements at magnetospheric altitudes. Figure 5.3 shows their measured convection patterns, mapped to the northern hemisphere ionosphere. Each pattern corresponds to a given sector of concurrent IMF clock angle.

This figure, which is in good agreement with the other studies cited above, reveals several details about how the IMF orientation affects the ionospheric and magnetospheric convection. When the IMF is southward, the convection is significantly stronger than when it is northward. This is in good agreement with what we expect from the discussion in Section 3.1. The convection is also profoundly affected by the sign of B_y. For positive B_y, the convection cell at dawn is crescent shaped, and the dusk convection cell is more circular. For negative B_y, we see the opposite configuration, although the differences between the convection cells are much less prominent. This lack of mirror symmetry between different signs of B_y appears in most large statistical studies of the convection.

Ruohoniemi and Greenwald (2005), who used SuperDARN measurements, found that the tendency that B_y sculpts a pair of crescent/round convection cells is reinforced for the combinations $B_y > 0$/summer and $B_y < 0$/winter. These combinations coincide with the findings of *Petrukovich* (2009), that the "penetration" of IMF B_y is reinforced in the tail for the same combinations. In Section 5.3, we discuss how this may be seen as an effect of ionospheric feedback on magnetospheric dynamics.

Conjugate measurements of convection

With the increased coverage of ground measurements in both hemispheres, it has become possible to study instantaneous inter-hemispheric differences in the convection. This was first done by *Lu et al.* (1994), using the Assimilative mapping of ionospheric electrodynamics (AMIE) technique. This technique employs all available measurements of convection (SuperDARN, DMSP, incoherent scatter radars), magnetic field (ground magnetometers) and ionospheric conductance (incoherent scatter radars, and indirectly from auroral imaging, ground magnetometers, and in-situ particle measurements from DMSP and NOAA), to produce an instantaneous map of ionospheric convection, conductance, and field-aligned current. *Lu et al.* (1994) studied a three days period, covering both positive and negative IMF B_z. When B_z was southward, they found a two-cell pattern which was largely mirror-symmetrical in the two hemispheres. When it was northward, lobe reconnection in one hemisphere produced significant differences in polar cap convection.

Later, studies of instantaneous conjugate ionospheric convection patterns have been undertaken, using SuperDARN (*Grocott et al.*, 2005; *Ambrosino et al.*, 2009). *Ambrosino et al.* (2009) looked at the response in the dayside convection patterns to rotations of the IMF. They found an immediate change in the convection in both hemispheres when the IMF turned southward, while the southern hemisphere response to a northward turning lagged behind the northern hemisphere by ~ 10 minutes. This time difference led them to suggest that the reconfiguration of the ionospheric convection was caused by lobe reconnection, and that this happened faster in the northern hemisphere because of the concurrent negative IMF B_x.

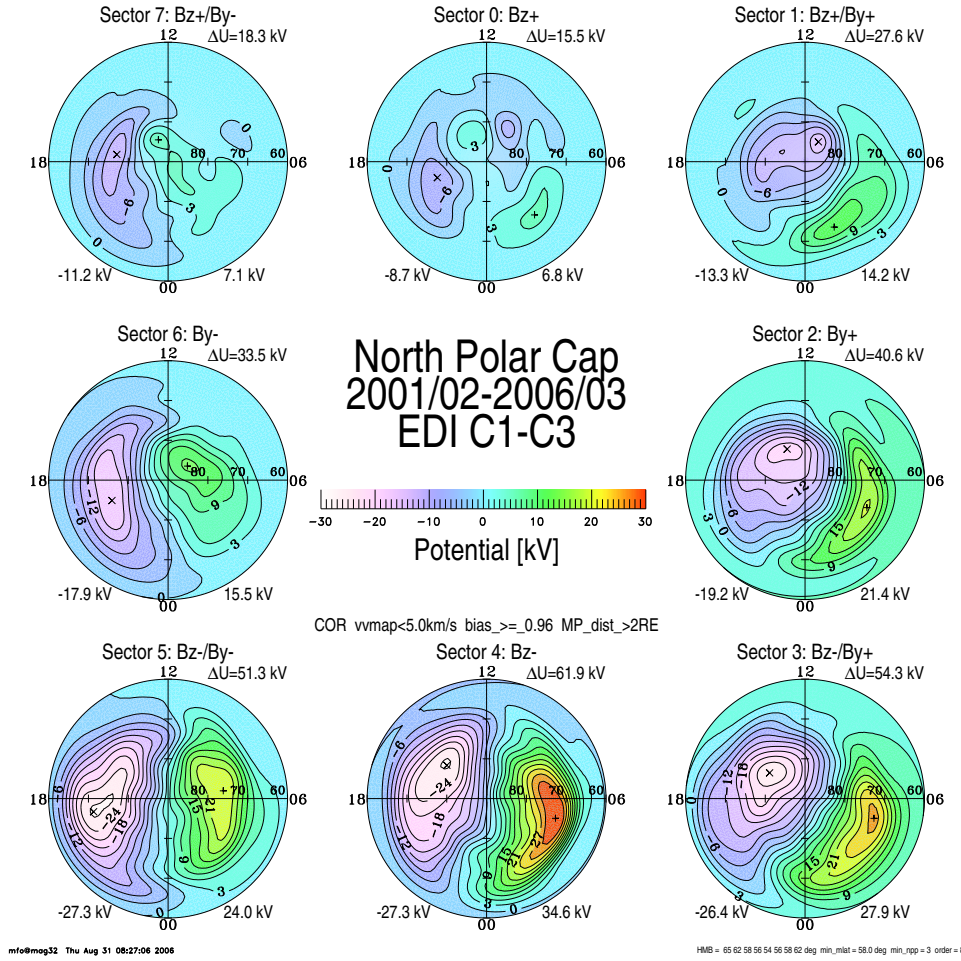

Figure 5.3: Electric potential, ϕ, composed by Cluster EDI measurements of plasma velocity, mapped to the ionosphere. The potential patterns are binned by concurrent IMF clock angle sectors. The convection velocities ($\mathbf{v} = -\nabla\phi \times \mathbf{B}/B^2$) are along the equipotential contours, clockwise where the potential is negative, and counter-clockwise where the potential is positive. Equipotential contours are spaced by 3 kV. From *Haaland et al.* (2007).

Ionospheric convection during substorms

Common to most of the statistical studies of convection is that they mainly considered steady IMF conditions, and relatively quiet conditions in the magnetosphere. Our observations in Papers III and IV are suggested to imply differences in the convection between the two hemispheres during a substorm expansion phase, which is not necessarily well represented by statistical studies based on steady conditions. A few studies exist which more directly observe the ionospheric convection following the onset of substorms. *Blanchard et al.* (1997) looked at the convection using the Sondrestrom incoherent scatter radar during 24 events. They found that on average, the convection does not increase until ~ 20 minutes after the substorm onset. Subsequent studies have employed the SuperDARN radars to study the convection during substorms statistically. Based on 67 events, *Provan et al.* (2004) reported a faster response than what was observed by *Blanchard et al.* (1997). *Bristow and Jensen* (2007), who looked at 10 substorms, observed an abrupt decrease in convection velocity, accompanied by a rotation from zonal to meridional, equatorward flow. A statistical study of 1979 isolated substorms, by *Grocott et al.* (2009), showed that during the expansion phase, the convection tends to increase for substorms with onset at high latitudes, and decrease for substorms with onset on lower latitudes. It should be noted that none of these studies focused on seasonal effects. Seasonal differences in ionospheric convection during substorms seem to be implied by the observations in Papers III and IV.

5.2.5 Summary

Before we look at some of the prevailing theories explaining the observed inter-hemispheric asymmetries, we briefly sum up the most important and established results reviewed above. Conjugate auroral imaging show that on high latitudes, the conjugate field line footprints can be significantly distorted from the IGRF predictions. Auroras on lower latitudes have been observed to be mostly symmetrical. From conjugate auroral imaging, statistical studies of the aurora, and in-situ magnetic field measurements, we know that on average, there is an effective "penetration" of the IMF to the magnetosphere, on both open and closed field lines. This is certainly true for the B_y component, while ambiguous results exist for the effect of B_x. However, this penetration is likely not uniform, as evidenced by the different correlations found in different sectors of the lobe (*Tsurutani et al.*, 1984), and at different local times (*Wing et al.*, 1995). The B_y component also has a very clear effect on the average ionospheric convection, sculpting a pair of crescent/round convection cells. Compelling evidence exists that the convection pattern for $B_y < 0$ is not the exact mirror image of $B_y > 0$ patterns, presumably due to a secondary seasonal control. Seasonal conditions is also a decisive factor for the acceleration of auroral electrons. In the dark hemisphere, electron spectra are harder than in the sunlit hemisphere. The auroral power is higher on the dayside during the summer, but it is lower on the nightside, compared to winter conditions.

5.3 Causes for inter-hemispheric asymmetries

In this section we look at theoretical works which address possible causes for inter-hemispheric asymmetries. We retain the approach from Section 2.3, focusing on the forces acting on the plasma fluid, causing the plasma to move such as to manifest the observations reviewed above. We start by considering asymmetrical forces acting on the magnetosphere from the solar wind, or forces which can be considered to directly generate the asymmetries. Then we look at how an asymmetrical ionospheric response between hemispheres may affect the global geometry of the magnetosphere. We also look at how regions where ideal MHD breaks down can contribute to the observed inter-hemispheric asymmetries. Finally we look at some proposed causes for inter-hemispheric differences in auroral intensity.

5.3.1 Asymmetric driving of the magnetosphere

In an effort to explain the Svalgaard-Mansurov effect, *Jørgensen et al.* (1972) proposed that newly opened magnetic field lines in the dayside magnetosphere are subject to magnetic stresses in the east-west direction. Figure 5.4a is copy from the paper by Jørgensen, showing that when the IMF has a positive B_y component, the geometry of newly opened field lines implies curvature forces, which produce flow from dusk to dawn in the northern hemisphere. For negative B_y, the effect is the opposite. This is in good agreement with observations of convection on the dayside, and this effect has been the starting point of many subsequent theories, addressing convection, ionospheric current systems, and inter-hemispheric asymmetries in field-line footpoints.

Although its influence is much less prominent in observations, a similar effect can be ascribed to the IMF B_x. Figure 5.4b is a copy from *Cowley* (1981a), who proposed the following scenario: If B_x is positive, the curvature on newly opened field lines will exert a stronger anti-sunward force in the northern hemisphere, causing an acceleration of the flow on these field lines, compared to the southern hemisphere. When the open field lines have crossed the dawn-dusk meridian, the curvature force will act in the opposite direction. These sunward forces will also be different in the two hemispheres, causing a more efficient breaking of the open field lines in the southern hemisphere, compared to the northern hemisphere. This implies that magnetic flux is added more rapidly to the northern lobe at any given distance along the GSM x axis, displacing the neutral sheet in the negative z direction. The result is equivalent to a net penetration of IMF B_x to the magnetosphere.

Based on earlier work by *Cowley* (1981b), their own observations and MHD modeling, and the observations by *Tsurutani et al.* (1984) of non-uniform (in tail cross-sections) correlation between the IMF B_y and lobe B_y, *Khurana et al.* (1996) presented a conceptual model to explain how the IMF affects the closed field line geometry in the magnetosphere. Figure 5.5a shows a cross section of the magnetotail. It illustrates an idea first suggested by *Cowley* (1981b), that in the presence of IMF $B_y \neq 0$, the normal component of the magnetic field through the magnetopause will be stronger in certain sectors. This is a consequence of the azimuthal B_y generated flow on newly opened field lines, which implies asymmetric addition of open flux to the lobe. For positive B_y, magnetic flux will enter the

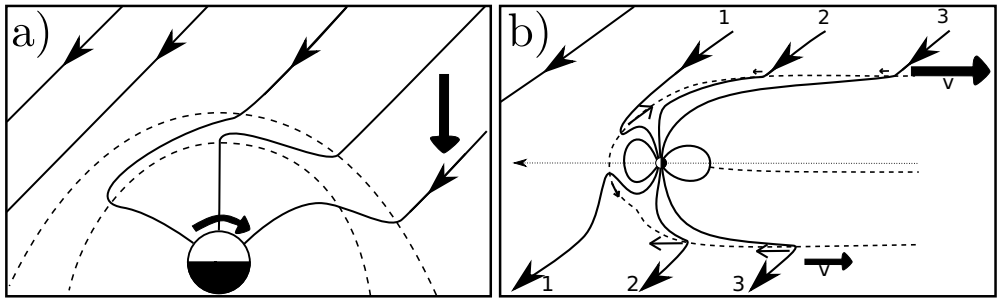

Figure 5.4: a) Equatorial cross section of the magnetosphere, in the presence of positive IMF B_y. Due to the orientation of the IMF, newly opened field lines are subject to curvature force, pulling them from dusk to dawn on the dayside. The resulting flow is shown with thick black arrows. After *Jørgensen et al.* (1972). b) Cross section of the magnetosphere in the xz-plane in the presence of positive IMF B_x. Curvature forces on open field lines (thin arrows) cause the field lines to move faster anti-sunward in the northern hemisphere. The thick arrows indicate flow velocity. The asymmetric velocity causes an increased pressure in the northern lobe, displacing the neutral sheet in the negative z direction. After *Cowley* (1981a).

magnetosphere preferentially in the northern dawn and southern dusk sectors of the tail, and the two remaining sectors will essentially be closed. *Khurana et al.* (1996) proposed that the asymmetric addition of flux and plasma which is implied by this geometry leads to a higher pressure, magnetic and thermal, in the open sectors. The pressure differences across the tail then induces a flow towards the closed parts of the lobe, indicated by the gray arrows in Figure 5.5a. Figure 5.5b shows the same phenomenon projected on the equatorial plane of the magnetosphere. The numbers indicate the progression of open field lines as they are being transported by the solar wind anti-sunward. In the northern lobe (left), magnetic flux enters through the magnetopause on the dawn flank (IMF $B_y > 0$). Since the magnetospheric part of the field line has been slowed down compared to its far end, the field lines gradually align with the x axis, decreasing B_y in the lobe. This process also implies convection from dawn to dusk in the northern lobe, and from dusk to dawn in the southern lobe (right part of Figure 5.5b). It also implies that in the closed sectors of the lobe, the magnetic field will be almost unaffected by the sign of the IMF B_y. The duskward convection in the northern lobe is also consistent with the duskward convection seen on the night-side of the polar cap, when $B_y > 0$ (see e.g., Figure 5.3), which takes over after the dawnward convection on the dayside which presumably is due to magnetic stresses on newly opened field lines (*Jørgensen et al.*, 1972).

The shear flow across the neutral sheet which is implied by this model is what *Khurana et al.* (1996) proposed leads to the observed "penetration B_y" on closed magnetic field

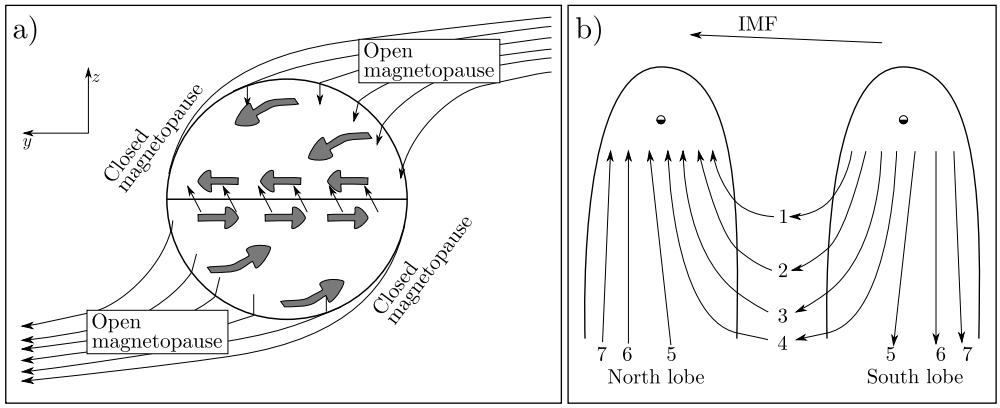

Figure 5.5: a) Cross section of the magnetotail in the presence of positive IMF B_y. Flux is added to the tail asymmetrically, causing the boundary to be essentially closed in the northern dawn and southern dusk. The asymmetrical addition of flux causes a gradient in the pressure, which induces the convection indicated by the thick gray arrows. b) Evolution of open magnetic field lines in the tail, in the northern (left) and southern (right) lobes. After *Khurana et al.* (1996).

lines. If this shear flow partially extends to closed field lines, it implies a perturbation B_y in the same direction as the IMF B_y. The resulting field is shown as tilted arrows at the demarcation line between the two lobes in Figure 5.5a. *Khurana et al.* (1996) suggested two ways that the shear flow in the lobes can be extended to closed field lines: 1) The inertia of the lobe will be partially preserved when field lines are closed, implying a continuation of the shear flow on closed field lines, and 2) viscous drag between the two regions, through a wave particle interaction mechanism.

5.3.2 Asymmetrical ionospheric feedback

In the above models, the ionosphere was regarded as passively (or at least symmetrically) complying with the imposed magnetospheric flow. This idealization has been prevalent in most theoretical works on inter-hemispheric asymmetries. However, as has become more and more clear from observations (including Papers III and IV), the ionosphere may play a key part in producing asymmetries at high latitudes.

In the time-dependent case, when the convection in the magnetosphere changes, the time it takes for the ionosphere to adapt to these changes depends, among other things, on the conductivity. The way that the magnetospheric flow, or the imposed stresses, are communicated to the ionosphere, is by shear Alfven waves (e.g. *Song et al.* (2009)). These waves can be reflected, depending on conditions in the ionosphere. *Scholer* (1970) derived

the following equation for the reflection of Alfven waves in the ionosphere:

$$R = \frac{E^{ref}}{E^{inc}} = \frac{\Sigma_A - \Sigma_P}{\Sigma_A + \Sigma_P} \tag{5.3}$$

where E is the electric field of the incident (superscript inc) and reflected (ref) Alfven wave, Σ_A is the Alfven conductance, $1/\mu_0 v_A$, and Σ_P is the ionospheric Pedersen conductance. Usually, $\Sigma_P > \Sigma_A$, and the ratio will be negative. This implies, considering a superposition of the incident and reflected wave, that the electric field is reduced. In the case that $\Sigma_P \gg \Sigma_A$, the coefficient is -1, and the ionosphere will remain unaffected by the wave, tying the magnetic field line footpoint to its current position (*Coroniti and Kennel*, 1973). Because of the frozen-in property, field-line tying will affect the geometry and convection in the magnetosphere.

The Pedersen conductance increases with the degree of solar illumination, and precipitation of particles, preferentially of low energies (*Robinson et al.*, 1987). Both of these parameters may well vary between hemispheres, causing the ionosphere to respond differently to magnetospheric convection in the two hemispheres. The different degrees of field-line tying will then lead to asymmetries between hemispheres, independent of whether or not the driving forces in the magnetosphere are symmetrical between hemispheres.

Atkinson and Hutchison (1978) showed that gradients in ionospheric conductance also can affect the convection in the steady state. Using a very simple model, they were able to qualitatively reproduce the observed accumulation of ionospheric convection equipotential contours at dawn, which seems to be implied by the lack of mirror symmetry between the average convection patterns when B_y is positive and when it is negative (e.g. *Heppner and Maynard* (1987); *Ruohoniemi and Greenwald* (2005)). Later, *Tanaka* (2001) confirmed, using an MHD model, that when the ionospheric conductance is uniform (Figure 5.6a), the convection is largely mirror symmetrical for different signs of B_y, and that deviations from mirror symmetry only appear when gradients in the ionospheric conductance are introduced (Figure 5.6b). The lack of mirror symmetry also affects the convection at magnetospheric altitudes, as demonstrated by *Haaland et al.* (2007), who used in-situ measurements from the Cluster spacecraft to derive average convection patterns, mapped to the ionosphere. Combined, these results strongly indicate that the ionosphere affects magnetospheric convection (and hence the geometry) also in the average, time-independent case.

Based on this, we may interpret the findings of *Ruohoniemi and Greenwald* (2005), that the sculpting of crescent/round convection cells are reinforced with the combination of summer/positive B_y and winter/negative B_y, to be an effect of the changing average location of the sunlight terminator with seasons. The same can be said about the findings by *Petrukovich* (2009), that the "penetration" B_y is more strongly positive (negative) in the magnetosphere during northern summer (winter), as well as the secondary influence of dipole tilt angle on the inter-hemispheric longitudinal displacement of the aurora, indicated by the data set of *Østgaard et al.* (2005c).

In summary, there is clear evidence, both from theoretical considerations and from observations, that the ionosphere significantly modulates the magnetospheric dynamics,

a) Uniform conductance: mirror symmetry

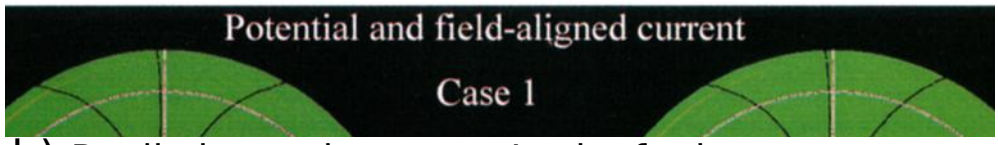

b) Realistic conductance: Lack of mirror symmetry

Figure 5.6: Figures 1 (a) and 4 (b) from *Tanaka* (2001). The contours show ionospheric convection patterns (in steps of 6 kV) in the northern hemisphere, from MHD modeling with uniform (a) and realistic (b) ionospheric conductance, and otherwise similar conditions ($B_y = \pm 2.5$ nT and $B_z = -4.3$ nT). Note that the colors show different quantities in the two figures (FACs [$\mu \mathrm{Am}^{-2}$] in the upper figure, and conductance [mhos] in the lower figure). The numbered arrows refer to the text in Tanaka's paper.

and because the ionospheric conditions rarely are symmetrical between hemispheres, inter-hemispheric asymmetries are expected to arise in the magnetosphere. This is true, not only in the average, steady state magnetosphere, but also in the highly dynamical case.

5.3.3 Effects of breakdown of ideal MHD

Two effects which arise only when ideal MHD breaks down may also affect the geometry of the magnetosphere more directly than what has been discussed in the preceding section: Reconnection and parallel electric fields.

Reconnection

Terrestrial magnetic field lines which connect to the interplanetary magnetic field on the dayside of the magnetosphere are being transported tailward with the solar wind. Newly opened field lines will have a curvature which depends on the orientation of the IMF. In the southern hemisphere, the curvature will cause these field lines to be pulled in the same direction as the orientation of the IMF (in the y direction), and in the northern hemisphere, the field lines will be pulled the other way. The effect that this has on nightside reconnection is illustrated in Figure 5.7, where the solid open magnetic field lines, which have symmetrical ionospheric footpoints, do not meet in the tail. Instead, reconnection takes place between the dashed open field lines, which have asymmetrical footpoints. The result is equivalent to a net penetration of the IMF to closed field lines (*Østgaard et al.*, 2004).

Parallel electric fields

As discussed in Chapter 2.3.3, any electric field which appears in the frame of reference of the plasma will affect the time development of the magnetic field, in such a way that the frozen-in condition will break down. One way to look at the frozen-in property is to consider the field lines to be labeled by the plasma to which it is frozen. A temporal breakdown of the frozen-in condition can therefore be seen as a period when the magnetic field lines are "re-defined"; plasma which used to be attached to field lines mapping to one region of the ionosphere becomes frozen to field lines mapping to a different region in the ionosphere, without the field lines or the plasma convecting (field line motion may not even be a meaningful concept without some way to label them).

The effect of parallel electric fields was discussed quantitatively in Paper III, for the open/closed boundary, based on an approach by *Vasyliunas* (1984). We repeat the argument here, to emphasize that it holds for arbitrary closed field lines.

Faraday's law (Eq. 2.3) can be written:

$$\oint (\mathbf{E} + \mathbf{u} \times \mathbf{B}) \cdot d\mathbf{l} = -\frac{\partial \Phi}{\partial t} \tag{5.4}$$

where we used Equation 2.13 to transform the electric field in the frame of reference of the integration path to the frame of reference in which the path moves at velocity $\mathbf{u}$.

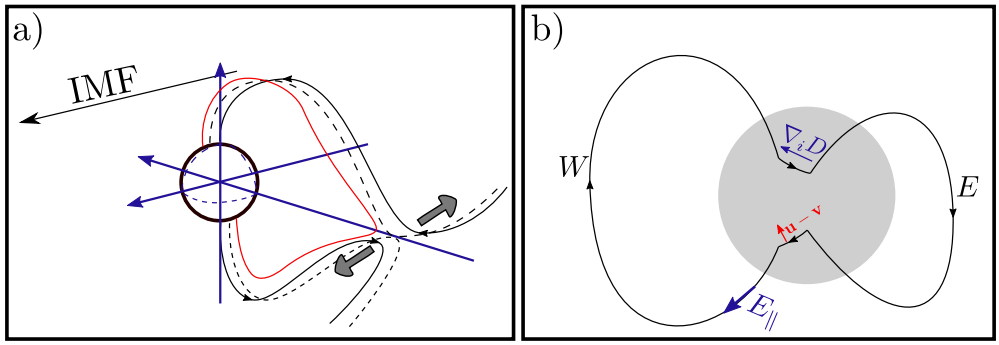

Figure 5.7: a) Reconnection of magnetic field lines with asymmetrical footpoints. The open solid field lines have symmetrical footpoints, but curvature forces (gray arrows) pull the southern hemisphere field lines in the direction of the IMF, and the northern hemisphere field line the other way, preventing them from reconnecting in the tail. Instead, reconnection takes place between the dashed field lines, which have asymmetrical footpoints (after *Østgaard et al.* (2004)). b) Illustration of the effect of gradients in net magnetic field aligned potential drops between hemispheres. For simplicity, we only consider a parallel electric field in the southern hemisphere in the western magnetic field line. This implies a westward gradient in net field aligned potential drop.

We choose the integration path sketched in Figure 5.7b, which we can divide into four parts: Two segments which run along magnetic field lines between hemispheres, and two segments connecting these field lines in the ionosphere. We place the ionospheric paths at sufficiently high altitude so that we can assume that $\mathbf{E} = -\mathbf{v} \times \mathbf{B}$, where $\mathbf{v}$ is the ionospheric convection (*Østgaard et al.*, 2005b). Integrating 5.4 along magnetic field lines yield the net electric potential drop along the field lines. We define $D = \int E_\parallel d\mathbf{l}$, with $E_\parallel$ positive in the direction parallel to the magnetic field. With this convention, the integrals along magnetic field lines in Figure 5.7b can be written $D_W - D_E$, where W and E indicate west and east, respectively. The different signs arise from the opposite directions of the integration paths. Now we choose the integration path such that it encloses a surface which is never threaded by magnetic field lines. Then, the right hand side of Equation 5.4 is constantly 0, and therefore vanishes. The result is

$$D_W - D_E + \int_{C_{iN}} (\mathbf{u} - \mathbf{v}) \times \mathbf{B} \cdot d\mathbf{l} + \int_{C_{iS}} (\mathbf{u} - \mathbf{v}) \times \mathbf{B} \cdot d\mathbf{l} = 0 \tag{5.5}$$

where C_{iS} and C_{iN} denote the ionospheric segments of the integration path in the southern and northern hemispheres, respectively. The $\mathbf{u} - \mathbf{v}$ terms denote plasma flow across the integration path. This flow is zero in ideal MHD, but Equation 5.5 shows that the presence of non-canceling parallel electric fields causes this to break down. A change in the $\mathbf{u}$'s,

relative to the **v**'s is equivalent to "re-defining" the flux tubes, by changing the plasma by which they are labeled. This equation can be used to address the magnitude of the plasma flow across magnetic field lines: We approximate the ionospheric integration paths by introducing average magnetic fields, assumed to point in the perpendicular direction, $B_\perp$, average **v** and **u**, positive in the equatorward direction, and perpendicular to the integration path, and the length of the integration path, L. $LB_\perp$ is, for simplicity, assumed to be equal in magnitude in the two hemispheres (although the signs are different, because of the different magnetic field directions in the two hemispheres). We also assume that the equatorward ionospheric convection is equal in the two hemispheres. Then Equation 5.5 reduces to:

$$u_N - u_S = \frac{D_E - D_W}{L|B_\perp|} = \frac{\nabla_i D}{|B_\perp|} \tag{5.6}$$

where ∇_i denotes the gradient along the ionospheric integration paths, positive in the eastward direction.

As illustrated in Figure 5.7b, a westward gradient in net potential drop is associated with an equatorward motion of the southern hemisphere footpoint relative to the northern hemisphere footpoint. *Sato et al.* (2005), who used ground all-sky imagers, reported a relative difference in the motions of conjugate magnetic field line footpoints between 43 and 66 m/s. According to Eq. 5.6, for a difference in u of 50 m/s, magnetic field strength of 50,000 nT, and a scale of 300 km (the field of view of the all-sky camera at 110 km is 1000 km), the corresponding difference in net field aligned potential drop along the western magnetic field lines is 750 V (assuming $D_E = 0$). With typical auroral arc electron energies of a few keV, this does not seem unreasonable.

We note that even though the plasma and magnetic field are not frozen-in at regions with parallel electric fields, the frozen-in condition holds in the surrounding regions, and the ideal-MHD conditions prevent plasma from entering these regions. The flow of plasma across field lines is confined to regions in which ideal MHD breaks down. This suggests that the effect of $\nabla_i D$ could be much less straightforward than what has been described above.

5.3.4 Causes for differences in auroral intensities

Differences in auroral energy spectra and power between hemispheres have been reported both statistically and from conjugate measurements. To gain a complete understanding of the cause for many of the reported differences, it is likely that we have to consider a long chain of events, involving global magnetospheric dynamics, ionospheric feedback, reconnection, and current sheets in the auroral acceleration region.

A simplified approach is therefore often used, in which the auroral precipitation is thought to reflect the field-aligned current (FAC) density. This is partly motivated by the Knight relation (*Knight*, 1973), $j_\parallel = KE_\parallel$, where $j_\parallel$ is the FAC density, $E_\parallel$ is the parallel electric field, and K is a proportionality constant, which depends on the electron density. While this is a useful relation, which may provide explanations to many reported auroral phenomena, it may also be misleading.

Ohtani et al. (2009) studied the relation between FAC density and precipitating particles in the pre midnight sector, using DMSP satellites. Contrary to what we would expect from a naive inspection of the Knight relation, the mean energy did not show a clear dependence on the current density. However, the precipitating electron energy flux was observed to increase with increasing FAC density. The latter finding lends some credence to the use of FACs to explain variations in auroral luminosity. A surprising conclusion from their study was that field-aligned currents (region 1 and region 2) in the pre-midnight sector were generally stronger in the dark hemisphere, compared to the sunlit hemisphere. They suggested that this difference is because the Pedersen conductance, which they calculated using their measurements of electron precipitation, and the *Robinson et al.* (1987) formula, is actually higher in the dark hemisphere than in the sunlit hemisphere. This is because of increased precipitation in the dark hemisphere, creating an "over-reaction" to the absence of sunlight induced conductance. These results demonstrate the complexity of explaining variations in auroral intensity.

In the following, we have grouped some of the proposed explanations for inter-hemispheric differences in auroral intensity into three mechanisms which are linked to FACs (these are necessarily simplifications), and one which is an effect of the magnetic field geometry.

Solar illumination

As described in Section 4.2.1, increasing parallel electric fields can be understood as a way of compensating for the inability of ambient electric charges to carry the current implied by $\nabla \times \mathbf{B}$ (Eq. 2.5). Intuitively, we would therefore expect parallel electric fields to be stronger in regions with fewer charges, i.e. in the dark hemisphere. This is in agreement with the observed seasonal differences on the nightside. A similar conclusion can be drawn from the Knight relation: with equal current densities, stronger electric fields are needed when the electron density is low.

Seasonal differences in the ionosphere also affect the formation of the feedback instability (*Lysak*, 1991). This instability, which may be responsible for small-scale structuring of auroral arcs, arises from the modification of the ionospheric conductivity which is due to precipitating particles.

Effects of the IMF

The IMF has also been suggested to cause intensity asymmetries more directly. For instance, the observations by *Shue et al.* (2002), that the intensity in the northern hemisphere is higher when $B_x < 0$ were suggested to be caused by a change in the prevailing convection pattern, modifying the flow shears and consequently FACs and auroral intensity. The change in convection was proposed as a direct consequence of the partial penetration of the B_x component, changing the geometry of the field (*Cowley*, 1981a).

Inter-hemispheric field aligned currents

As mentioned in Section 5.2.1, *Stenbaek-Nielsen and Otto* (1997) proposed that inter-hemispheric field aligned currents could explain the observations obtained by the all-sky cameras mounted on airplanes two decades earlier. This inter-hemispheric current (or rather, an inter-hemispheric component to the existing FAC) was suggested to be due to partial, but non-uniform penetration of the IMF B_y to the magnetosphere, which by Ampere's law implies currents. A similar explanation was suggested by *Liou et al.* (1998), to explain their observations of increased intensity in the northern hemisphere when IMF $B_y < 0$.

In Paper II, we observe large asymmetries in the auroral intensity, during times with concurrent negligible IMF B_y. During this event, however, the dipole tilt angle was large, so that the northern hemisphere was sunlit, and the southern hemisphere auroral zone was in darkness. These conditions are favorable for inter-hemispheric currents, according to a model by *Benkevich et al.* (2000). Their proposed inter-hemispheric FACs would go up (i.e., electrons going down) approximately at the locations where the aurora was most intense in the event studied in Paper II, making inter-hemispheric FACs a possible explanation for the observations. According to *Benkevich et al.* (2000), these currents arise in the following way: High latitude FACs (region 1) are stronger in the sunlit hemisphere, than they are in the dark hemisphere. The strong FACs close partly across the polar cap, and partly via the opposite hemisphere. The current crosses from one hemisphere to the other at regions with sharp gradients in the conductance, the conductance being calculated as the sum of the conductance in the two hemispheres at conjugate points. These gradients could be located at the sunlight terminator (in one of the hemispheres).

The *Benkevich et al.* (2000) model uses imposed FACs, with a realistic conductance pattern, current continuity, and Ohm's law. As we argued in Chapter 2, this technique presupposes a stable equilibrium. In the 12 May 2001 event (Papers II and III), the non-conjugate spots appeared during a very active time, a period of very strong imbalance between nightside and dayside reconnection. In the northern hemisphere, the non-conjugate spot was visible for only ≈ 10 minutes. The dynamic nature of the event, and the stable equilibrium required for the *Benkevich et al.* (2000) model poses a paradox. An alternative approach would be to treat the problem in terms of $\mathbf{v}$ and $\mathbf{B}$, and take into account large-scale dynamics. Using the observations of asymmetries in the poleward boundary of the aurora (assumed to coincide with the OCB), the appearance of inter-hemispheric current could be explained in the following (highly qualitative) way:

Figure 5.8 shows a flux tube connected to the ionosphere in both hemispheres at three different times. First, magnetospheric convection is excited, marked by the bold gray circle in the middle of the flux tube. For simplicity, the convection is depicted as circular, equivalent to a closed convection path in the magnetosphere. Since the ionosphere does not immediately catch up with this convection, it holds the magnetic field back, and the flux tube becomes twisted. Symmetrical (between hemispheres) currents then appear according to Ampere's law (a similar figure and explanation for FACs is given by *Paschmann et al.* (2003), p. 63). The magnetic stress associated with this twist excites ionospheric convec-

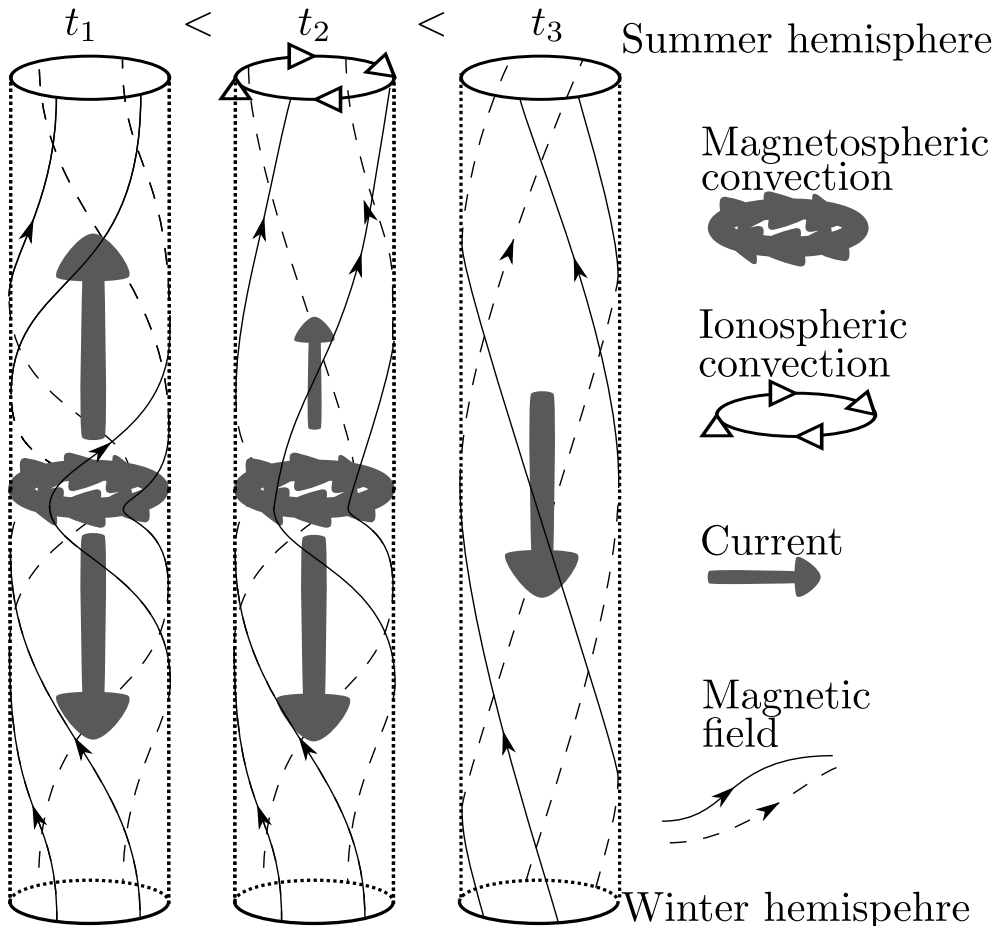

Figure 5.8: Cartoon showing how the asymmetrical ionospheric convection can set up a temporary inter-hemispheric current. We show magnetic flux tubes, extending from the winter hemisphere (in this case the southern hemisphere, since the magnetic field goes upwards) to the summer hemisphere. At $t = t_1$, convection is excited in the magnetosphere. Since the ionosphere does not immediately catch up with this convection, the flux tube is twisted, producing a symmetrical pair of currents. At $t = t_2$, the summer ionosphere has begun convecting, unwinding the twist, and reducing the current. At $t = t_3$, the driving of magnetospheric convection has been reduced, and the remaining twist of the magnetic field implies an inter-hemispheric current, which lasts until convection in the two hemispheres has unwound the twist. For simplicity, the figure shows only closed field lines, but the same mechanism may apply if part of the ionospheric loops connect to open field lines.

tion. At time t_2, the ionospheric convection has begun rectifying the twist in the summer hemisphere (in this case, the northern hemisphere), but not in the winter hemisphere. If the magnetospheric convection at some point is reduced, we are left with the situation seen at $t = t_3$, in which a twist remains in the flux tube connecting the two hemispheres. This implies an inter-hemispheric current. With convection differences similar to those suggested by the observations in Paper III and Paper IV, the direction of the current is from the sunlit hemisphere to the winter hemisphere at the dawnside of the onset local time (or the local time with the strongest earthward magnetospheric convection), and from the winter hemisphere to the summer hemisphere on the duskside. These locations are consistent with the observations of differences in auroral intensity (Paper II), and the timing is in qualitative agreement with the proposed difference in ionospheric convection following magnetotail reconnection (Paper III). This chain of events may also explain why the non-conjugate aurora appeared only for approximately 10 minutes at the dawn side, since the curl in the magnetic field represents magnetic stress which will have a finite duration.

It should be noted that the situation at $t = t_2$ in Figure 5.8 seems unrealistic, with stronger FACs flowing to the dark, and presumably (but not necessarily, according to *Ohtani et al.* (2009)) low-conductance, hemisphere. This happens because the ionospheric convection is depicted to take place first in the summer hemisphere, in accordance with the simplest representation of the ionospheric convection differences suggested in Papers III and IV. The net effect of this difference in convection is that the magnetic field geometry changes, such as to imply an inter-hemispheric current.

Low altitude magnetic field strength

As charged particles, spiraling around magnetic field lines, approach regions of converging magnetic field strength, they experience a net force (mirror force), repelling them in the opposite direction. This means that, at low altitudes in the auroral zone, particles either collide with the atmosphere, and may thereby contribute to the aurora, or they bounce back along the magnetic field lines. Since the magnetic field of the earth is not perfectly symmetrical between the hemispheres, the altitude at which they mirror can be different, and thus also the probability that particles collide with the atmosphere. Figure 5.9 shows the ratio of magnetic field strength at low altitude, in apex coordinates at 21:45 UT. From this figure, we see that in certain regions, the difference can be quite large, almost up to a factor of 2. The largest differences are found at 21 MLT in Figure 5.9, which in the southern hemisphere corresponds to the region south of South America, where the magnetic field has a minimum, called the South Atlantic anomaly.

Since accelerated auroral particles attain a highly field-aligned distribution, the resulting auroral intensity is not expected to be notably affected by the differences in mirror force. However, it may be important to the diffuse aurora, as reported by *Stenbaek-Nielsen et al.* (1973). These authors showed that, if the pitch angle distribution of the particles is isotropic, the ratio of the precipitating particle flux to the two hemispheres depends on the ratio of magnetic field strength in the two hemispheres. They also considered theoretically how parallel electric fields and weak diffusion may amplify or reduce this effect. In the case

of weak diffusion, the particles slowly fill the loss cone. If the bounce periods of the particles are shorter than the diffusion time, the particle precipitation could be much stronger to the hemisphere with the weakest magnetic field, even with relatively small differences between hemispheres.

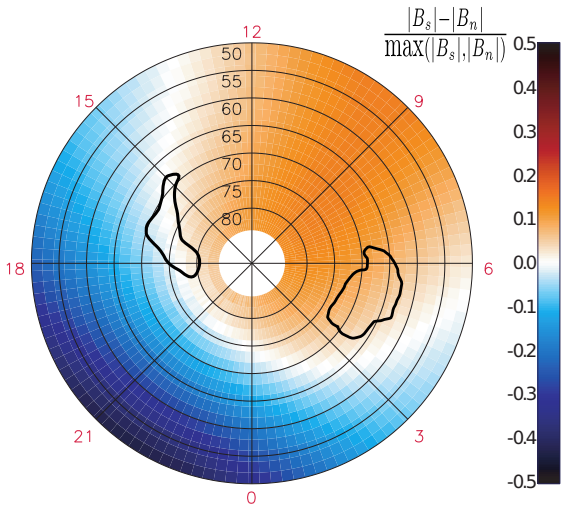

Figure 5.9: The ratio of low-altitude magnetic field strength at conjugate points in the two hemispheres. The ratio is plotted in magnetic coordinates, for 21:45 UT, at the time of the images in Figure 1 in Paper II. Contours of the non-conjugate aurora are also shown.

Also shown in Figure 5.9 are contours of the non-conjugate auroral spots reported in Paper II. These spots were seen in regions where the magnetic field strength differed by less than 10%. We can conclude that the differences in intensity were not caused by asymmetries in the mirror force in this case.

5.4 Future potential of inter-hemispheric measurements in the study of magnetosphere-ionosphere coupling

Ionospheric dynamics on high latitudes can be seen as the result of magnetospheric dynamics, and the various coupling mechanisms between the ionosphere and the magnetosphere (Figure 3.2). Since the ionosphere is much more accessible than the high altitude magnetosphere, most of our knowledge about magnetospheric dynamics is indirectly inferred from

ionospheric measurements, assuming the coupling processes to be known. This assumption may however be problematic during the most dynamical events, such as substorms. Since conjugate measurements in the ionosphere provide two independent pictures of the ionosphere, which correspond to the exact same magnetospheric state, such measurements have the potential to increase our understanding of the coupling processes.

The incoherent results of the studies of ionospheric convection during substorm expansion phase (Section 5.2.4) may be seen as an example of how the unknown coupling prevents a consistent picture of the magnetospheric state during certain periods. If the response time in the two hemispheres is different, as was discussed in Section 5.3.2 and in Papers III and IV, conjugate measurements of the convection could provide new insight to the nature of the coupling.

Several current projects provide conjugate measurements which can be used to continue and expand on studies of the magnetosphere-ionosphere coupling. SuperDARN[2], which consists of several radars measuring ionospheric convection, can be used to generate global instantaneous maps of the convection in both hemispheres (although the signal tends to disappear when auroral activity is high, excluding many of the perhaps most interesting events). SuperMAG[3] is an initiative to collect as many ground magnetometer measurements as possible in one place, using a common coordinate system, and a user friendly interface. With knowledge, or assumptions, on the conductance, these measurements can also be used to assess global convection in both hemispheres. The Assimilative Mapping of Ionospheric Electrodynamics (AMIE) technique is a technique to combine all relevant measurements to produce instantaneous maps of ionospheric parameters (conductance, currents, convection). The Iridium satellites, whose primary purpose is to facilitate satellite phone communication, are also equipped with magnetometers. Magnetic field measurements from the ~ 70 satellites have recently been used to generate maps of field-aligned currents in both hemispheres with relatively high time resolution[4].

The Chinese KuaFu project is a future initiatives to monitor the aurora in both hemispheres. It is thought to encompass two IMAGE like satellites and one solar wind monitor in orbit around the L1 point. The schedule for the KuaFu project, if it is realized, is not known[5].

[2]SuperDARN web page: http://superdarn.jhuapl.edu/

[3]SuperMAG web page: http://supermag.jhuapl.edu/

[4]FAC patterns derived from Iridium: http://sd-www.jhuapl.edu/UPOS/FAC/

[5]Information about KuaFu at Chinese Academy of Science web pages: http://english.cssar.cas.cn/ic/ip/200909/t20090917_38746.html

Chapter 6

Instrumentation and data processing

In this chapter we give an overview of the instruments which have been used to collect the data for the papers in this thesis. The key instruments are the FUV cameras on IMAGE, and the VIS Earth camera on Polar, and we therefore place particular emphasis on the quantitative interpretation of these measurements. We also mention the solar wind monitors that we have used, as well as low altitude satellites which provide in-situ measurements of particle precipitation.

Please consult page 86 for definitions of acronyms which are not given in this chapter.

6.1 Global UV imaging

The IMAGE satellite (*Burch*, 2000) was launched in March 2000. It carried several instruments designed to remotely image the magnetosphere, observing extreme ultraviolet (EUV), radio (RPI) and far ultraviolet (FUV) wavelengths, as well as neutral atoms (HENA/MENA). The FUV instrument consisted of three photometers (GEO), and three imagers, WIC, SI-12, and SI-13. In the next section, we look in more detail at the FUV instrument.

The Polar satellite was launched in February 1996. It carried twelve scientific instruments, three of which could be used for auroral imaging: The Polar Ionospheric X-ray Imaging Experiment (PIXIE) measured X-ray emissions, or bremsstrahlung, emitted as energetic electrons are decelerated in the atmosphere. The Ultraviolet Imager (UVI) provided UV images of the aurora, at different wavelengths. The Visible Imaging System (VIS) was designed to provide images of the aurora at visible wavelengths. This instrument also included a UV camera, VIS Earth Camera, which was intended as a monitor of the direction of the field of view of the visible wavelength cameras with respect to the sunlit Earth. However, the VIS Earth camera has produced a much more extensive scientific outcome than the visible wavelength cameras. The VIS Earth camera has also been used in the present thesis, preferred over UVI because of its large field of view (20°, compared to 8° in UVI), enabling observations of the global aurora from relatively low altitudes.

Table 6.1 shows an overview of the satellite orbits, and some parameters for the cameras

Satellite	IMAGE			Polar
Apogee			7.2 R_E	9 R_E
Perigee			1000 km	1.8 R_E
Orbit period			14.2 h	17.5 h
Life time			Mar. 2000 - Dec. 2005	Feb. 1996 - Apr. 2008
Camera	WIC	SI-13	SI-12	VIS Earth
Integration time	10 s	5 s	5 s	32.5 s
Cadence	123 s	123 s	123 s	54 s
Wavelength range	140 − 190 nm	135.6 nm	126.8 nm	124 − 149 nm
Resolution	256×256	128×128	128×128	256×256
Field of view	17° × 17°	16° × 16°	17° × 17°	20° × 20°
PSF FWHM	3 pixels	1.5 pixels	2 pixels	–

Table 6.1: Overview of the IMAGE and Polar satellites, and the UV cameras which were used in this thesis (*Mende et al.*, 2000a; *Frank et al.*, 1995). PSF FWHM is the full width at half maximum of the point spread function, taken from *Hubert et al.* (2002). Both IMAGE and Polar were NASA missions.

that we have used.

6.1.1 IMAGE FUV

The FUV instrument (*Mende et al.*, 2000a) encompasses three imagers: The Wideband Imaging Camera (WIC) (*Mende et al.*, 2000b) and the Spectrographic Imager (SI) (*Mende et al.*, 2000c), which produces two narrow pass-band images, centered at two wavelengths: 135.6 nm (SI-13) and 121.8 nm (SI-12). The WIC camera has a wide passband, observing aurora primarily in the range from 140 nm to 190 nm, which is dominated by N_2 emissions in the Lyman-Birge-Hopfield (LBH) band and a few strong N lines. The dynamic range and the resolution of WIC is higher than that of SI (*Frey et al.*, 2003a).

The narrow passbands of the SI channels are accomplished by an advanced system of slit grills, leading the light at the two wavelength regions to two different detectors. The 135.6 nm line, which is observed by SI-13, is emitted by atomic oxygen. Compared to the more intense OI line at 130.4 nm, the 135.6 nm line is scattered in the atmosphere only to a limited degree, and therefore the intensity in this camera is believed to be a good proxy for the total precipitation. The SI-12 camera has a peak sensitivity at ≈ 0.2 nm longer wavelengths than the Lyman-α emissions from hydrogen (121.56 nm). Blocking the Ly-α, the SI-12 signal is dominated by Doppler shifted emissions from receding hydrogen atoms. These atoms are primarily caused by precipitating protons, which charge exchange with the neutral atmosphere, and pick up an electron. Subsequently the hydrogen atom may be ionized again, and the process can be repeated hundreds to ten thousands of times, depending on the initial energy of the proton precipitation. The SI-12 transmission function is sinusoidal, with peaks every 0.5 nm, decreasing in amplitude away from 121.8

nm and reaching 0% transmission at $\lambda < 117$ nm and $\lambda > 126.5$ nm (*Immel et al.*, 2003).

The FUV cameras were mounted radially out from the spinning satellite, the spin period being 123 s. As the Earth swept through the field of view of the cameras every 123 s, the WIC camera, which had a CCD detector, took approximately 300 video frames. These frames were subsequently integrated to produce one image, using an on-board processing system called Time Delay Integration (TDI). A similar technique was applied to produce the SI images, which had a different detector (crossed delay-line) which recorded the position of every single photon, rather than instant 2D images.

Since the cameras observed the Earth from an altitude of several R_E, even very small inaccuracies in the pointing would lead to large errors in the interpretation of the images. To pin down the orientation of the cameras, we adjust the images so that the stars in the camera field of view (FOV) match the predicted (known) locations of the stars. With the software we have used[1], the pointing adjustment could be done with a one day resolution (i.e., the adjustment for one image is common to all images from the same day). During the course of the IMAGE mission, different pieces of the RPI instrument fell off[2], changing the satellite spin axis, causing it to wobble. This wobbling motion introduced a rhythmic (period of ~ 10 minutes) pointing error in the FUV images which could not be corrected using the star adjustment method. Data from the last part of the IMAGE mission should therefore be treated with some caution. For the 12 May 2001 event (Papers II and III) the wobbling is hardly noticeable.

In Section 6.1.4, we discuss the quantitative interpretation of images taken by the FUV cameras.

6.1.2 Polar VIS Earth

The VIS Earth Camera (*Frank et al.*, 1995) was mounted on a despun platform on the Polar satellite. It was equipped with a broad-band filter with a FWHM of 25 nm. The passband was $124 - 149$ nm, which includes the intense OI emissions at 130.4 nm and 135.6 nm, but also part of the LBH-band. For the periods when Polar and IMAGE produced conjugate images, the integration time of the camera was 32.5 seconds. The nominal cadence was 54 seconds, although when the other channels of the VIS instrument were in use, it was longer. Its sensitivity was 4.32 counts/kR.

The quantitative interpretation of VIS Earth images is discussed in Section 6.1.4.

6.1.3 Background removal

The images taken by VIS Earth and the FUV cameras have been corrected for varying sensitivity between pixels (flatfield correction), and for time dependent variations in sensitivity. This means that the intensity at different regions of the image, and images from different times, can be directly compared. The source of the measured intensity can then

[1] We have used Fuview, developed by the FUV team at Space Sciences Laboratory, Berkeley, USA

[2] according to the log file of FUV operations, at
http://sprg.ssl.berkeley.edu/image/wic_summary/0_fuv_operations.log

roughly be divided into three components: Auroral emissions, a relatively uniform (Poisson distributed) but slowly time-varying background, and sunlight induced emissions from the dayside ionosphere. The two latter components can represent a significant fraction of the total observed intensity, making auroral studies difficult, unless these emissions are subtracted from the image. In the following we describe two background/dayglow removal techniques which have been used in this thesis.

Geometric

In Paper I, we used geometric considerations to remove the dayglow in the SI-12 camera. The background proved to be fairly well modeled in two steps: First subtract a constant background, and then a crescent-shaped dayglow. The dayglow was modeled by assuming that the intensity in a given pixel depends on the area which is observed in the pixel, roughly proportional to $1/\cos\theta_{DZA}$, $\theta_{DZA} \leq 80°$, where θ_{DZA} is the satellite zenith angle (0° when viewing from nadir), and the inverse of the area over which the sunlight is distributed, which is approximately proportional to $1/\cos\theta_{SZA}$, where θ_{SZA} is the solar zenith angle. In a pixel with given $(\theta_{SZA}, \theta_{DZA})$, the intensity is then:

$$I(\theta_{SZA}, \theta_{DZA}) = I_0 \frac{\cos(\theta_{SZA})}{\cos(\theta_{DZA})}, \qquad \theta_{DZA} \leq 80° \tag{6.1}$$

The proportionality constant I_0 was determined by assuming that the pixels on the dayside, equatorward from the oval, were entirely due to sunlight. This constant was determined individually for each image, and the resulting background was then removed.

This method did not produce good results in WIC, because WIC is sensitive to dayglow scattered beyond the sunlight terminator. Another problem with this method is the assumption of linearity between the pixel intensity and the fraction on the right hand side. With more background pixel samples, more advanced relations can be considered. Figure 6.1a shows the intensity in background WIC pixels, plotted against $\cos\theta_{SZA}/\cos\theta_{DZA}$, from images taken during the substorm event shown in Figure 3.3. The background sample pixels were obtained from the region between 45° and 53°, and above 85° magnetic latitude, which was well outside the auroral oval. The red curve is a fitted function, in this case a constant for low values of the fraction (pixels which were in darkness, and dominated by the constant background), and a polynomial for higher values. The correlation between the observed intensity, and the intensity predicted by the fitted function is 0.997, which means that practically all variation in background intensity is captured by the functional fit. This method requires that the time variation in the background is slow. To include time variation in the model background, time could be included as a parameter, in addition to the angles.

Figure 6.1b shows this method applied on the WIC image from 13:29 UT on 23 June 2000. Panel b1 shows the original image, b2 shows the modeled background, and b3 shows the difference between the original image and the background. This is one of the auroral images which are shown in Figure 3.3. Since the background is roughly Poisson distributed, subtraction of a smooth background leaves significant noise in sunlit parts of the image.

This is clearly seen in Figure 6.1b3. Figure 6.1b4 shows a smoothed version of Figure 6.1b3.

Another variation of this method has also been used, in which the background is assumed to depend only on solar zenith angle. Then one can collect pixels which are outside the auroral oval, and interpolate to get the function $I_{BG} = f(\theta_{SZA})$. This method supposes that the background is independent of viewing angle, and is therefore less accurate. However, it is often seen to work quite well, and it is useful in double-checking the validity of other methods.

Polynomial fit

In Papers II and III, we fitted a 2D polynomial to the background and dayglow in the WIC images, and then subtracted this polynomial from the image. The method is illustrated in Figure 6.2. To fit the polynomial to the background, we had to define a region which was believed to be void of auroral emissions. This region was identified in two steps: First, we guessed at the location of the aurora, and fitted a polynomial to the remaining pixels. The fitting was done using the IDL routine, SFIT. Then we subtracted the resulting polynomial (Figure 6.2b) from the image (Figure 6.2a), thus removing most of the background. This corrected image (Figure 6.2c) was then used to identify the pixels containing aurora, using the IDL search routine SEARCH2D. The pixels which did not contain aurora, were assumed to contain background. These background pixels were then used in a second iteration of the polynomial fit. The resulting polynomial (Figure 6.2d) was subtracted from the original image, producing the final corrected images (Figure 6.2e). This method is inspired by the method used by *Hubert et al.* (2002) (personal communication).

While the polynomial fit effectively removed the background in the 12 May 2001 event, studied in Papers II and III, it did not prove to be universally applicable. To use this method, we had to carefully choose the input parameters, such as the order of the polynomial, the threshold in the SEARCH2D routine, and the initial guess at oval location. In many cases we did not succeed in getting a good polynomial fit to the background. The method seems more likely to succeed if the oval is completely embedded in sunlight, as in the 12 May 2001 event. It is less likely to succeed in imagers with lower resolution (e.g. the SI), since the fitted function will be based on fewer pixels. The same is true if the FOV does not cover much of the background. In the case of 12 May 2001, similar results were obtained using both the polynomial fit, and the geometric technique described in the previous section.

6.1.4 Quantitative interpretation

As the unit of the FUV images we have generally chosen instrument counts, rather than something physically more meaningful. Ideally, we would like to convert counts to energy flux ($\mathrm{mW/m^2}$), so that the measurements can be compared with those from other instruments, or serve as input in models. However, without complementary measurements, which can assess the mean energy of the precipitating particles, such a conversion necessitates

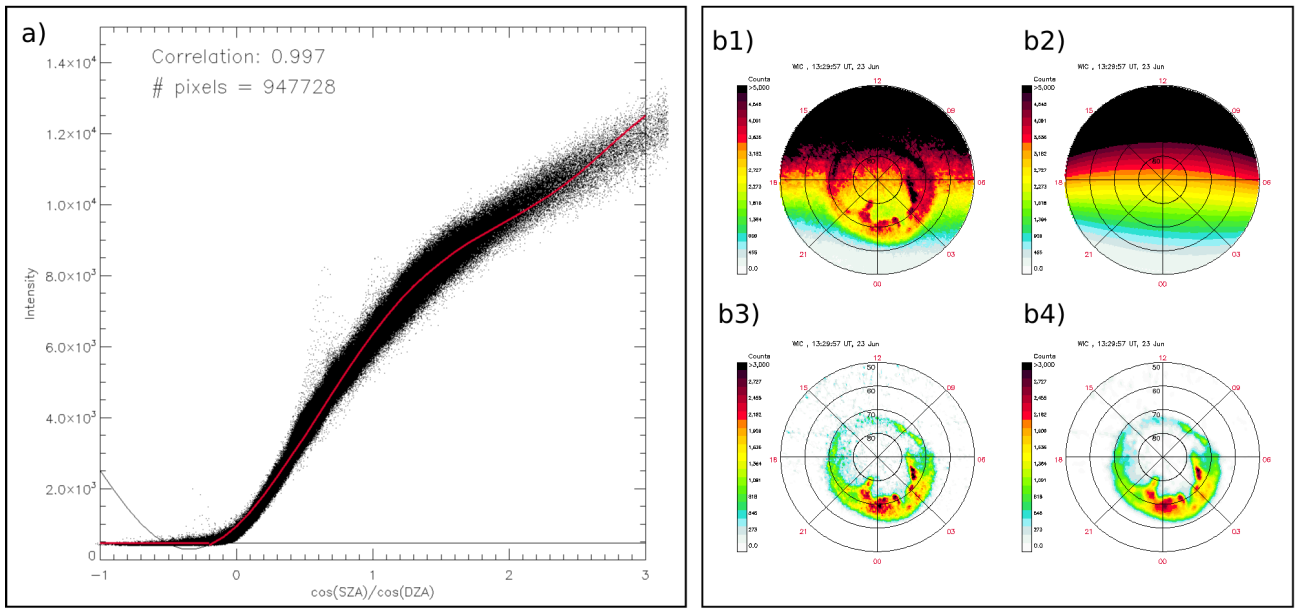

Figure 6.1: a) Intensity in background (non-aurora) pixels, plotted against $\frac{\cos\theta_{SZA}}{\cos\theta_{DZA}}$ (947728 pixels in total), for images taken on 23 June 2000, by IMAGE WIC. The correlation between the observed intensity, and the intensity according the functional fit, shown in red, is 0.997. b) The technique applied on the image taken at 13:29 UT at 23 June 2000. The figure shows the original image (b1), the modeled background (b2), the corrected image (b3), and a smoothed version of the corrected image (b4).

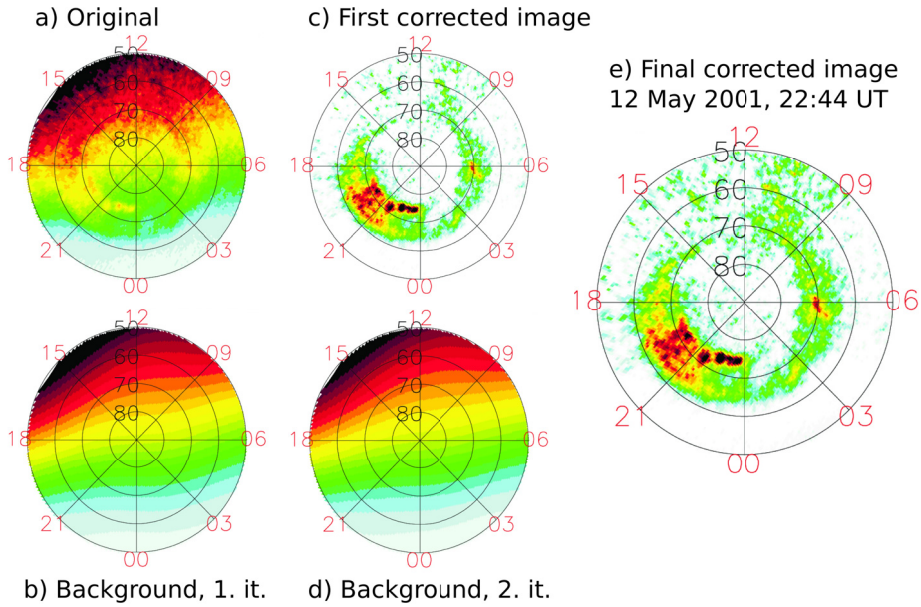

Figure 6.2: Example of polynomial fit method. a) Original image, b) fitted polynomial in first iteration, c) corrected image after first iteration, d) fitted polynomial in second iteration, e) final image. The color scales range from 0 to 2000 counts in the corrected images (c and e) and from 0 to 8000 in the original and the background images (a, b, and d)

crude assumptions, which almost certainly introduce errors. When energy flux is not required to answer a particular scientific question, we have chosen to process the data as little as possible, thus minimizing the black box between the instrument signal and the printed figures. The reduced black box does however come at the expense of an increased gap between the measurements and the real world. In this section we try to fill in part of this gap, by describing what the instrument counts correspond to in terms of energy flux.

Mathematically, the instrument counts in a given pixel at a given time is

$$I_{\text{counts}} = \int_0^\infty f(\lambda)g(\lambda)d\lambda \tag{6.2}$$

where λ is the wavelength, $g(\lambda)$ is the (known) passband of the camera, and $f(\lambda)$ is the spectrum of the photons reaching the camera. The latter function contains the atmospheric response to particle precipitation, and thus depends on several unknowns: The atmospheric composition, and the energy, mass, charge and direction of each of the precipitating particles. With the aid of atmospheric models and knowledge about (or assumptions on) the

distribution of the precipitating particles, it is possible to reduce the number of unknowns down to energy flux, so that Equation 6.2 relates energy flux and instrument counts.

We also note that the uncertainty in $f(\lambda)$ also affects the conversion from counts to kR. Since kR is a measure of the number of photons/sm^{2}sr, and since $g(\lambda)$ is not uniform, the same number of photons (same kR) does not always produce the same number of counts. In the conversion to kR used in Figure 1 of Paper II, we have used the value at the peak sensitivity of the WIC camera (*Frey et al.*, 2003a).

IMAGE FUV

Frey et al. (2003a) presented a comprehensive summary of some of the efforts (e.g., *Gérard et al.* (2000, 2001); *Hubert et al.* (2001, 2002)), that have been made to determine Equation 6.2 for the FUV instrument. The description given here relies heavily on this paper. The IMAGE FUV instrument package was designed so that energy flux could be determined with a fair accuracy without additional measurements. The procedure is as follows:

1. First, we have to measure, or assume a mean energy for the proton precipitation. When this is done, we use a modeled atmospheric response (assuming the protons have a kappa distribution) to find the energy flux associated with the observed intensity in SI-12. The modeled response is shown in Figure 6.3a.

2. A given proton energy flux, at the assumed mean proton energy, produces a known (also from the model) intensity in the SI-13 and WIC images. Figures 6.3b and c can be used to subtract the proton contribution, so that the SI-13 and WIC counts are solely due to electron precipitation.

3. After having subtracted the proton contribution, the WIC/SI-13 ratio depends on the mean electron energy (Figure 6.3f). An increasing mean electron energy increases the WIC/SI-13 ratio. This division produces a map of the mean electron energy.

4. Finally, Figure 6.3d (6.3e) can be used to find the energy flux which produces the observed WIC (SI-13) counts.

Application of the above technique requires that the images have been accurately corrected for background and dayglow. To perform the proton subtraction and the WIC/SI-13 division, it is also necessary that the pixels are mapped to the same grid. A slight error in background subtraction in SI-13, or in the pointing of one of the cameras with respect to the other, can produce dramatic results, since the SI-13 count rate is low compared to WIC. Another complication is that the atmospheric composition is assumed fixed in the atmospheric models used to derive the relations in Figure 6.3. It has been shown that the O/N_2 atmospheric density ratio is reduced during high geomagnetic activity, and the difference between the regions of O/N_2 depletion and the undisturbed regions can be more than a factor of two (*Strickland et al.*, 1998). Since WIC is sensitive to emissions from N_2, and SI-13 responds to emissions from atomic oxygen, the WIC/SI-13 ratio will increase in the O/N_2 depletion region, independent of the mean electron energy.

Even though the application of the method may be problematic, the modeled relations between counts and energy flux are informative. Figure 6.3a shows that the SI-12 camera efficiency increases very rapidly at low energies, just above its threshold at ≈ 1 keV. It reaches a maximum at $2-3$ keV, before it decreases rapidly. At high energies, the decrease is slow, and so we would expect SI-12 to respond to all energies of some significance in the magnetosphere (the ring current energy is is mainly carried by $10-200$ keV protons). These protons would also produce a significant signal in WIC and SI-13 (Figures 6.3b and 6.3c).

Figure 6.3d shows that, for constant energy flux, the WIC signal is rapidly reduced when the electron energy increases: At 20 keV the signal is ≈ 20 % of that at 1 keV. This trend is even more severe for SI-13 (Figure 6.3e) which is reduced to ≈ 10 % when the mean energy is increased from 1 to 20 keV.

Polar VIS Earth

We are not aware of any published study systematically addressing the response of the VIS Earth camera to electron energy flux, and its dependence on precipitation at different energies. However, Figure 6.4a shows an empirically determined relationship between observed VIS Earth intensity and electron energy flux (J. Sigwarth, personal communication). The upper and lower curves represent the 75th and 25th percentiles, respectively.

The VIS Earth response to varying electron energy can also be described using the information in *Frey et al.* (2003a). Polar VIS Earth observes emissions in the energy range of $124-149$ nm. This range encompasses the two intense atomic oxygen lines at 130.4 nm and 135.6 nm (which SI-13 observes), as well as some of the LBH band. In quiet conditions (pure dayglow emissions and very low-energy precipitation), *Frank and Sigwarth* (2003) report that 83 % of the VIS Earth signal is due to the 130.4 nm line. Figure 6.4b compares the intensity of the 130.4 nm and 135.6 nm lines for 1 $\mathrm{mW/m^2}$ electron flux at various mean energies. The numbers are based on Table 6.2, which is a reproduction of Table II in *Frey et al.* (2003a). The figure shows that, if the intensity in the VIS Earth camera is dominated by the 130.4 nm line, we can expect it to behave approximately like SI-13.

However, for higher energies, the relative importance of the various emission lines will change. According to Table 6.2, at low electron energies (0.2 keV) the 130.4 nm line represents 54% of the collective intensity escaping from the atmosphere from the LBH band and the two OI lines at 135.6 nm and 130.4 nm (in the nadir direction). At high energies (25.0 keV), the ratio is 10%. The relative importance of the 130.4 nm line in the VIS Earth signal thus decreases with increasing energy. We can therefore expect that as the energy increases, the relative importance of LBH emissions will increase in the VIS Earth signal. Based on this, the WIC/VIS ratio is expected to be approximately proportional to the WIC/SI-13 ratio (Figure 6.3f) at low energies, but to increase more slowly at higher energies.

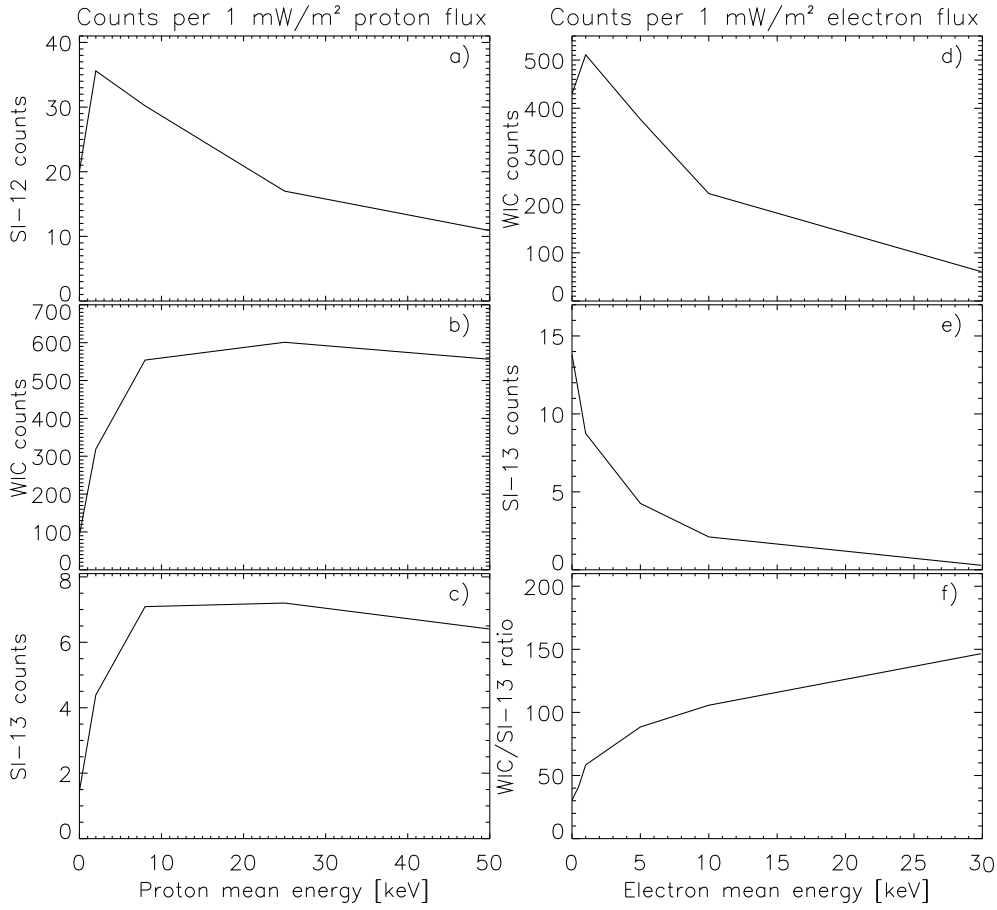

Figure 6.3: The response of SI-12 (a), WIC (b) and SI-13 (c), in corrected instrument counts, to a 1 mW/m^2 proton flux. Protons are assumed to be kappa distributed, with mean energy given at the x axis. The response of WIC (d) and SI-13 (e) to Maxwell distributed electron precipitation is also shown (mean energy at the x axis). Panel f shows the ratio of WIC and SI-13 counts. Figures a, b, c, d, and e are after Tables III, V, VIII, IV, and VII in *Frey et al.* (2003a), respectively.

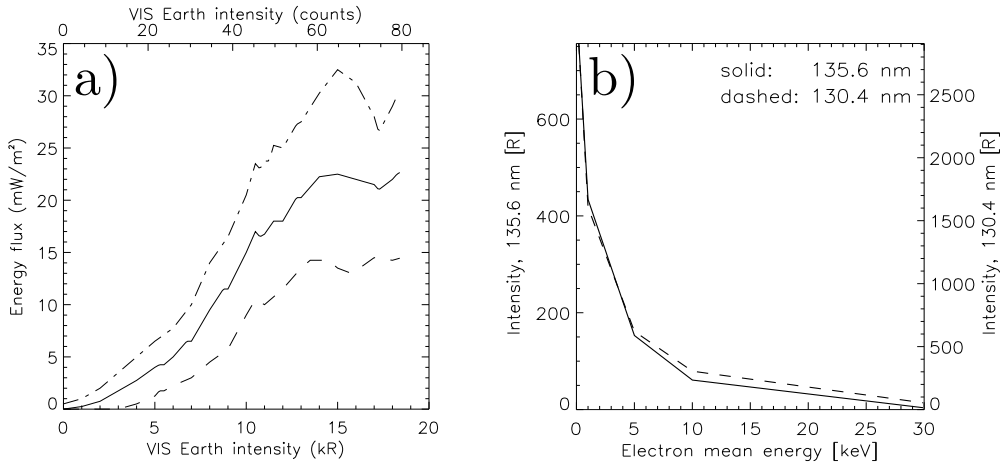

Figure 6.4: a) Empirically determined relationship between precipitating energy flux, and auroral intensity observed in the VIS Earth camera (J. Sigwarth, personal communication). b) Atmospheric response to electron precipitation. The solid curve shows intensity (in Rayleigh) of the 135.6 nm emission line (left y axis), and the dashed curve shows intensity of the 130.4 nm emission line (right y axis). The intensities are shown as function of mean electron energy. After Table 6.2

6.2 Solar wind monitors

Since high-latitude geomagnetic activity is mainly a consequence of interaction with the solar wind and the interplanetary magnetic field, it is essential to have measurements of the upstream solar wind conditions. In the papers in the present thesis, we have used ACE and Geotail for this purpose. Other spacecraft which are commonly located outside the magnetosphere is Wind and Cluster, which are still operational, and IMP-8, which was in operation from 1973 to 2001.

6.2.1 ACE

In all the papers in this thesis, we use measurements from the Advanced Composition Explorer (ACE) (*Stone et al.*, 1998). ACE was launched in August 1997, into an orbit about the Earth-Sun Lagrangian point, $\sim 240\ R_E$ sunward of the Earth. The Solar Wind Electron, Proton and Alpha Monitor (SWEPAM) (*McComas et al.*, 1998) is used to measure solar wind density and velocity. The solar wind dynamic pressure can then be calculated as $m_p n v^2$. Here, n is the proton density, v is the bulk velocity, and m_p is the proton mass. The formula should be adjusted if the fraction of heavier ions, mainly He^{2+}, becomes significant. The magnetic field is measured by a magnetometer, MAG (*Smith et al.*,

< E > [keV]	LBH	LBH abs.	1356	1356 abs.	1304	1304 abs.
0.20	1630	1629	757	756	2908	2907
0.50	1940	1910	638	635	2420	2420
1.00	2450	2390	440	434	1607	1606
5.00	3070	2320	194	153	630	621
10.0	3194	1738	124	61	321	305
25.0	3170	1010	85	18	132	116

Table 6.2: Atmospheric response to 1 mW/sm^2 electron precipitation, from Table II of *Frey et al.* (2003a). The table shows intensity [Rayleigh] of LBH, 135.6 nm and 130.4 nm emissions at different average electron energies, with and without atmospheric absorption.

1998).

Since the instruments on ACE record changes in the solar wind before these changes reach Earth, we need to time shift the measurements to relate solar wind parameters to observations in the magnetosphere, typically by $\sim$ 30 minutes to 1 h. We have employed two methods to do this time shift. 1) Variations in solar wind dynamic pressure often have clear effects on the magnetic field at ground, in near-Earth space, and on the auroral luminosity. ACE measurements can therefore be time shifted to match the solar wind variations with the observed effects in the magnetosphere. 2) The plane in which the solar wind has the least variation can be identified, using a statistical technique (*Weimer*, 2004). This plane represents the orientation of solar wind "phase fronts", which may be tilted with respect to the direction of the solar wind propagation. When the phase front orientation is known, this can be used to determine the distance which the measured solar wind variations travel before reaching the magnetosphere, and the time shift can be calculated as this distance, divided by the velocity. Time shift methods are discussed further in the papers.

6.2.2 Geotail

The Geotail satellite was launched in 1992, to an elliptical orbit with perigee and apogee at 8 R_E and 210 R_E, respectively. Its primary purpose was to investigate tail dynamics. In the 12 May 2001 event, which is studied in Papers II and III, it was located in the solar wind. We use measurements of the magnetic field, from the MGF instrument (*Kokubun et al.*, 1994). The advantage of using Geotail measurements in this event was that the time shift from the Geotail position to the magnetosphere was very small, or negligible.

6.3 Low altitude satellite measurements

Low altitude (< 1000 km) satellite measurements were used in Paper III to accurately determine the poleward boundary of the precipitation using in-situ particle measurements.

These measurements have also been useful in comparison with FUV images in the other studies, as an assurance that the camera pointing is correct.

6.3.1 DMSP

The Defense Meteorological Satellite Program (DMSP) comprises a series of satellites equipped with instruments measuring, among other things, the flux of charged particles, magnetic field, auroral emissions, and convection velocity. Their orbit is circular, at an altitude of ~ 840 km, with a period of approximately 100 minutes.

In Paper III, we used particle measurements from the Special Sensor Precipitating Plasma Monitor (SSJ) instrument, from the DMSP F12, F13, F14, and F15 satellites. The SSJ/4 instrument consists of four electrostatic analyzers that record the flux of precipitating electrons or ions in 19 logarithmically spaced energy intervals from 30 eV to 30 keV. The detected particles originate from within $\sim 3^\circ$ of the vertical, which means that the particles are well within the loss cone.

The data we have used have been downloaded from, or plotted at the Johns Hopkins University Applied Physics Laboratory web site[3].

6.3.2 NOAA POES

Another series of low-altitude satellites also carry instruments that measure the flux of precipitating particles: The National Oceanic and Atmospheric Administration (NOAA) Polar Orbiting Environmental Satellites (POES). We used measurements from the Total Energy Detector (TED) to determine the point at which the the satellites (NOAA-15 and NOAA-16) crossed the polar cap boundary. TED measures electrons and ions in 16 different energy intervals, from 50 eV to 20 keV. The quantities which are telemetered to the Earth is the integrated flux from these channels, as well as the flux in four different channels, and in the channel with the highest flux.[4]

The NOAA data was provided by NOAA's National Geophysical Data Center (NGDC).

6.4 Magnetic indices

Ground magnetometers have long been the primary method of measuring geomagnetic disturbances on Earth. Several magnetic indices exist, which facilitate studies of long-term trends, and comparisons between different events. Here we briefly describe the AE indices, and the SYM-H and Dst indices.

[3] http://seegar.jhuapl.edu/dmsp/

[4] Documentation on the NOAA TED can be found at
http://poes.ngdc.noaa.gov/docs/sem2_docs/2006/SEM2v2.0.pdf

6.4.1 AE

The AE (Auroral Electrojet) indices are composed of measurements from up to 12 stations distributed around the northern auroral zone at typical auroral latitudes. The AL index is defined as the minimum horizontal component measured by these stations (a baseline is subtracted first from each station). Since the horizontal component points northward in the northern hemisphere, AL is a measure of the maximum southward perturbation of the magnetic field in the auroral zone. This southward perturbation is often interpreted as an effect of westward ionospheric currents. AU is defined as the maximum horizontal component among the 12 stations, presumably associated with eastward currents. The AE index is the difference between AL and AU, and AO is the mean.

Substorms are often associated with a sharp drop in the AL index and a slow ($\sim$ 1 hour) recovery. However, if the substorm is located on different latitudes than the AE stations, its magnitude may be misrepresented, or it may not even be noticed in the indices.

6.4.2 SYM-H

The SYM-H index, which was used in Paper I, is derived from six magnetometers at low latitudes (although they are $\approx 20^\circ$ away from the magnetic equator). The index is constructed as a normalized average of the southward component measured at these stations. The SYM-H index can be seen as a high resolution (1 minute) version of the Dst index, which has existed since the 1950s. These indices are used to define the periods called geomagnetic storms, when SYM-H drops below a certain value (*Gonzalez et al.* (1994) define Dst < -30 nT to be a small storm, and Dst < -100 nT is an intense storm). As in substorms, storms are seen as a sharp drop, and a slow recovery in the magnetic indices, but in the case of storms, the time scales are longer: The main phase (sharp drop in SYM-H) lasts for typically a few hours, and the recovery can last for several days.

The SYM-H and Dst indices have a fairly clear physical meaning. The total kinetic energy of all charged particles trapped in a dipole magnetic field is proportional to the deflection of the magnetic field at the center of the dipole. This elegant relation was derived by *Dessler and Parker* (1959) and *Sckopke* (1966). Since SYM-H and Dst are derived from low-latitude magnetic field measurements, they are therefore often interpreted as a direct measure of ring current energy. However, in the real magnetosphere, other regions also contribute to the measurements comprising SYM-H and Dst, most notably the magnetopause, the magnetotail, the ionosphere, and induced currents in the ground.

Chapter 7

Summary of papers

This chapter contains brief summaries and corrections to the papers.

Paper I: Persistent global proton aurora caused by high solar wind dynamic pressure

In this paper, we report observations of a very clear response in the global proton aurora to changes in the solar wind dynamic pressure: Examples from five events with concurrent IMF $B_z > 0$ (low solar wind driving) show that the proton aurora, observed by the SI-12 camera on IMAGE, increases (decreases) as the solar wind dynamic pressure increases (decreases). This is true, even for low pressure and small changes (from 1 nPa to only 2 nPa in one event), and for both gradual and transient changes in the pressure.

An important distinction between our observations (and the similar observations of electron dominated aurora reported by *Liou et al.* (2007)) and previous studies of auroral response to changes in solar wind dynamic pressure (e.g., *Meurant et al.* (2004)), is that our observations show a persistent change in intensity when the pressure changes; the intensity seems to depend on the magnitude of the pressure, rather than (or in addition to) the rate of change of the pressure.

We also present observations from two events, classified as storm main phases. A storm main phase is a time of very high geomagnetic activity, and intense auroras are expected. In the two events presented, the drop in SYM-H, which is a way of quantifying the intensity of the main phase, was comparable, but the intensity of the proton aurora was very different. The dynamic pressure in the solar wind was also very different in these events, which might suggest that the solar wind dynamic pressure plays an important modulating role, also for the most intense proton auroras, with intense auroras occurring only when the geomagnetic activity and the solar wind pressure are high simultaneously.

Correction

In the abstract, it says that the time delay between changes in ground magnetic signatures and changes in the proton aurora intensity is short, "-2 minutes". This should be "$\lesssim$ 2 minutes".

Paper II: Asymmetric auroral intensities in the Earth's Northern and Southern hemispheres

In this paper, we show that the global auroral intensity distributions can be completely different in the two hemispheres. A pair of simultaneous images, taken by IMAGE WIC in the northern hemisphere and Polar VIS Earth in the southern hemisphere, showed a much higher intensity at dawn in the northern hemisphere, compared to dusk, and a much higher intensity at dusk in the southern hemisphere, compared to dawn.

The inter-hemispheric intensity asymmetries which are reported in this paper are important for at least two reasons: i) They confirm a proposed pattern of inter-hemispheric currents (assuming the currents go up where the electrons precipitate), which arises because of differences in the ionospheric conductance (*Benkevich et al.*, 2000). ii) Auroral intensifications in global images are often interpreted as "tv screen" images of activations of the magnetospheric regions to which they map. The observations show that such an interpretation could lead to very different conclusions, depending on which hemisphere we look at.

See Section 5.3.4 for a more detailed discussion of inter-hemispheric currents, and different causes for inter-hemispheric differences in auroral intensity.

Paper III: Inter-hemispheric observations of emerging polar cap asymmetries

In this paper, we take a new look at the same event as in Paper II, but change focus to inter-hemispheric asymmetries in the poleward boundary of the aurora. This boundary was visible at all local times for approximately 50 minutes, during the expansion phase of a strong substorm. We show that the poleward boundaries propagated poleward at different rates in the two hemispheres, leading to large inter-hemispheric asymmetries in the polar caps. We also show that the magnetic flux encircled by the boundaries in the two hemispheres was similar, in both the 12 May 2001 event and in another event, on 23 October 2002 (studied in more detail by *Stubbs et al.* (2005)). This is expected if the boundary coincides with the open/closed magnetic field line boundary.

From the argument discussed in Section 5.3.3, we know, with certain assumptions about parallel electric fields, that the open/closed magnetic field line boundary moves in response to either magnetic reconnection (the boundary is re-defined), or plasma convection (the boundary is physically moved) (*Cowley and Lockwood*, 1992). The emerging

inter-hemispheric asymmetries in the polar cap boundary which were observed in Paper III can therefore be explained if the ionospheric response to increased magnetospheric convection was different in the two hemispheres. Specifically, the emerging asymmetries were consistent with earthward convection in the magnetosphere, excited by tail reconnection (*Cowley and Lockwood*, 1992), being communicated faster to the northern summer hemisphere than to the southern winter hemisphere. A detailed investigation of the [18, 21] MLT region indicated a difference in equatorward convection of $\sim$ 500 m/s, lasting for $\sim$ 10 minutes.

This study shows that substorm signatures can be different in the two hemispheres, emphasizing the need for further parameterization in statistical studies of substorms.

Correction

In Equation 8 in the paper, positive ΔV corresponds to an electric field in the same direction as the magnetic field somewhere along the eastern integration paths (C_{p2} and C_{p4}). This is in contrast to the statement in parentheses preceding the equation.

Paper IV: Seasonal and IMF dependent nightside polar cap contraction during substorm expansion phase

Paper IV follows up on the finding from Paper III, that during the expansion phase of a substorm, the polar caps can contract differently in the two hemispheres. The aim of this paper is to investigate statistically the effect of different seasons, and different orientations of the IMF, on the location of the open/closed boundary during substorm expansion phase. The observational basis for this paper is images from the 3943 substorms identified by *Frey et al.* (2004) in the IMAGE WIC data set. These images were used to construct a large database of OCBs at different substorm epoch times.

Among the main results from this study was that the average OCB in substorms observed in the winter (dark) hemisphere has a more pronounced bulge, compared to summer hemisphere substorms. In the summer hemisphere, the OCB is more smooth. At substorm onset, the summer hemisphere OCB is, on average, closer to equator, compared to the winter hemisphere. During the expansion phase, this asymmetry reduces. One possible scenario leading to this asymmetry is an overall larger increase in equatorward convection in the winter ionosphere, except for in the bulge region, where the winter hemisphere ionospheric convection is more suppressed than in the summer hemisphere.

With the statistical data set developed for this study, we can investigate the average effect of the seasonal and IMF conditions in the 12 May 2001 event, studied in Papers II and III. During this event, $B_x > 0$, $B_y \approx 0$, and the tilt angle was quite strongly positive (summer in the north). Figure 7.1a compares the average boundaries for substorms in the northern hemisphere with $B_x > 3$ nT and tilt angle $> 15^\circ$ (dashed) with substorms with $B_x < -3$ nT and tilt angle less than -15° (solid). These groups resemble the conditions in the 12 May 2001 event in the northern and southern hemisphere, respectively. Figure 7.1b

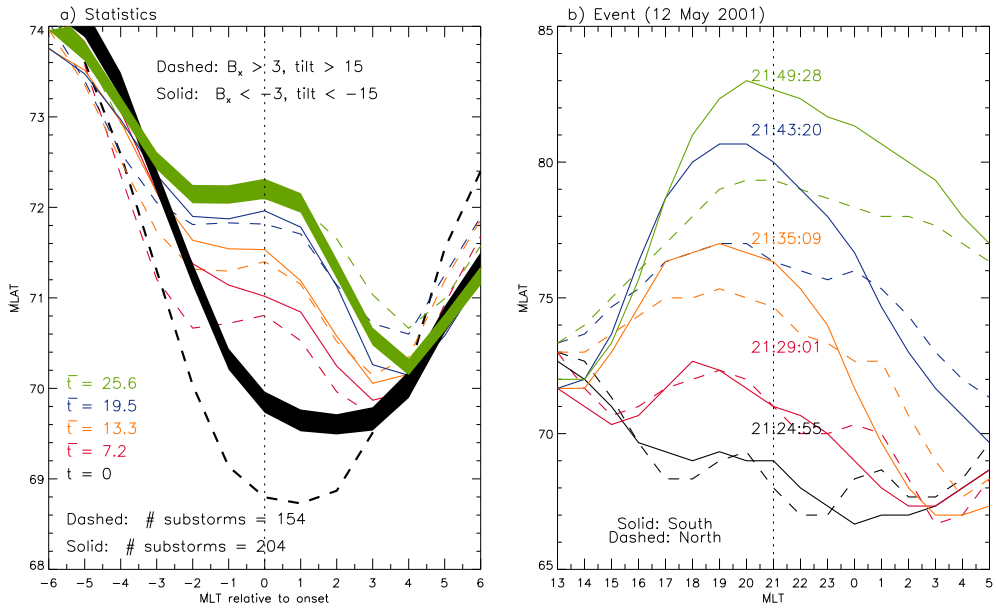

Figure 7.1: Comparison between the OCB in the 12 May 2001 event, discussed in Paper III (b), and the statistical average OCB for substorms with similar conditions (a). Note that the x and y axis have a much higher range for the single event boundaries. Figure a shows the average poleward boundary of the aurora at times relative to substorm onset, indicated by different colors. The x axis shows distance in MLT from the substorm onset location. The width of the black and green curves spans the standard error of mean. In contrast to the figures in Paper IV, these statistical distributions have been smoothed, using a boxcar average of width 3. Figure b is composed from simultaneous, or close to simultaneous, images taken in the two hemispheres at the times indicated in the figure (the times refer to the center of exposure in WIC). The dashed vertical bar in this figure denotes the approximate location of the onset (21 MLT).

shows the OCBs in the event, plotted in a similar format as the statistics. Dashed curves are from the northern hemisphere, and solid curves are from the southern hemisphere (to be compared with the corresponding line styles in Figure 7.1a).

A big difference between these plots is that the single event encompassed a larger dynamic range: The y axis spans 20°, compared to 6° in the statistics, and the x axis spans 16 hours, compared to 12 hours in the statistics. Further, there is only small, or no asymmetries at onset in the single event. During the expansion phase, a more pronounced bulge is formed in the winter hemisphere in the event, but this is not very prominent in the statistical plot. However, this feature corresponds well to what we observe when dividing substorms into summer and winter, independent of the orientation of the IMF (Figure 2 in Paper IV). In fact, the statistical plot and the case study look more similar for the reverse signs of B_x (this is not shown). Based on this, and on the conclusions from Paper IV, we conclude that the differences in the case study were due to seasonal effects, and that B_x may actually have had a dampening effect on the asymmetries in the May 2001 event. We can also conclude that instantaneous asymmetries between hemispheres can be much stronger than what is suggested by the modest (but statistically significant) asymmetries in the statistical study.

LoA List of Acronyms

AACGM	Altitude Adjusted Corrected Geomagnetic
ACE	Advanced Composition Explorer
AE	Auroral Electrojet
AMIE	Assimilative Mapping of Ionospheric Electrodynamics
ASC	All-Sky Camera
CCD	Charge-coupled device
DMSP	Defense Meteorological Satellite Program
EDI	Electron Drift Instrument
ENA	Energetic Neutral Atom
EUV	Extreme Ultraviolet
IGRF	International Geomagnetic Reference Field
IMAGE	Imager for Magnetopause-to-Auroral Global Exploration
IMP	Interplanetary Monitoring Platform
FAC	Field-aligned current
FOV	Field of view
FUV	Far Ultraviolet
FWHM	Full Width at Half Maximum
GEO	Geocorona Photometer
GSM	Geocentric Solar Magnetospheric Coordinate System
GUVI	Global UltraViolet Imager
HENA	High Energy Neutral Atom Imager
IMF	Interplanetary Magnetic Field
LBH	Lyman-Birge-Hopfield
LLBL	Low Latitude Boundary Layer
MENA	Medium Energy Neutral Atom Imager
MHD	MagnetoHydroDynamics
MLT	Magnetic Local Time
NENL	Near-Earth Neutral Line
NOAA	National Oceanic and Atmospheric Administration
OCB	Open/Closed Boundary
PIXIE	Polar Ionospheric X-ray Imaging Experiment
POES	Polar Orbiting Environmental Satellites
Polar BEAR	Polar Beacon Experiment and Auroral Research (satellite)
PSBL	Plasma Sheet Boundary Layer
PSF	Point Spread Function
R_E	Earth Radius (approximately 6370 km)
RPI	Radio Plasma Imager
SI	Spectrographic Imager
SuperDARN	Super Dual Auroral Radar Network
SWEPAM	Solar Wind Electron, Proton and Alpha Monitor
TED	Total Energy Detector
TIMED	Thermosphere Ionosphere Mesosphere Energetics and Dynamics (satellite)
UT	Universal Time
UV	UltraViolet
UVI	UltraViolet Imager
VIS	Visible Imaging System
WIC	Wideband Imaging Camera

Bibliography

Akasofu, S.-I., The development of the auroral substorm, *Planet. Space Sci.*, *12*, 273–282, 1964.

Ambrosino, D., E. Amata, M. F. Marcucci, I. Coco, W. Bristow, and P. Dyson, Different responses of northern and southern high latitude ionospheric convection to IMF rotations: A case study based on SuperDARN observations, *Ann. Geophys.*, *27*, 2423–2438, 2009.

Anderson, K. A., C. D. Anger, R. R. Brown, and D. S. Evans, Simultaneous electron precipitation in the northern and southern auroral zones, *J. Geophys. Res.*, *67*, 4076–4077, 1962.

Angelopoulos, V., et al., Statistical characteristics of bursty bulk flow events, *J. Geophys. Res.*, *99*, 21,257–21,280, 1994.

Atkinson, G., and D. Hutchison, Effect of the day night ionospheric conductivity gradient on polar cap convective flow, *J. Geophys. Res.*, *83*, 725–729, 1978.

Axford, W. I., and C. O. Hines, A unifiying theory of high-latitude geophysical phenomena and geomagnetic storms, *Can J. Phys.*, *39*, 1433, 1961.

Baker, K. B., and S. Wing, A new magnetic coordinate system for conjugate studies at high latitudes, *J. Geophys. Res.*, *94*, 9139–9143, 1989.

Baumjohann, W., and R. A. Treumann, *Basic space plasma physics*, Imperial College Press, 1997.

Belon, A. E., J. E. Maggs, T. N. Davis, K. B. Mather, N. W. Glass, and G. F. Hughes, Conjugacy of visual auroras during magnetically quiet periods, *J. Geophys. Res.*, *74*, 1–27, 1969.

Benkevich, L., W. Lyatsky, and L. L. Cogger, Field-aligned currents between conjugate hemispheres, *J. Geophys. Res.*, *105*, 27,727–27,737, 2000.

Blanchard, G. T., L. R. Lyons, and O. de la Beaujardire, Magnetotail reconnection rate during magnetospheic substorms, *J. Geophys. Res.*, *102*, 14,303–24,312, 1997.

Boakes, P. D., S. E. Milan, G. A. Abel, M. P. Freeman, G. Chisham, B. Hubert, and T. Sotirelis, On the use of IMAGE FUV for estimating the latitude of the open/closed magnetic field line boundary in the ionosphere, *Ann. Geophys.*, pp. 2759 – 2769, 2008.

Boakes, P. D., S. E. Milan, G. A. Abel, M. P. Freeman, G. Chisham, and B. Hubert, A statistical study of the open magnetic flux content of the magnetosphere at the time of substorm onset, *Geophys. Res. Lett.*, doi:10.1029/2008GL037059, 2009.

Bond, F. R., Auroral morphological similarities at two magnetically conjugate stations: Buckles Bay and Kotzebue, *Aust. J. Phys.*, *22*, 421–433, 1969.

Bristow, W. A., and P. Jensen, A superposed epoch study of SuperDARN convection observations during substorms, *J. Geophys. Res.*, *112*, doi:10.1029/2006JA012049, 2007.

Burch, J. L., IMAGE Mission Overview, *Space Sci. Rev.*, *91*, 1–14, 2000.

Burch, J. L., J. Goldstein, and B. R. Sandel, Cause of plasmasphere corotation lag, *Geophys. Res. Lett.*, *31*, doi:10.1029/2003GL019164, 2004.

Burns, G. B., D. J. McEwen, R. A. Eather, F. T. Berkey, and J. S. Murphree, Optical auroral conjugacy: Viking UV imager - South Pole Station ground data, *J. Geophys. Res.*, *95*, 5781–5790, 1990.

Carbary, J. F., T. Sotirelis, P. T. Newell, and C.-I. Meng, Auroral boundary correlations between UVI and DMSP, *J. Geophys. Res.*, *108*, doi:10.1029/2002JA009378, 2003.

Chaston, C. C., J. W. Bonnell, C. W. Carlson, J. P. McFadden, R. E. Ergun, and R. J. Strangeway, Properties of small-scale Alfven waves and accelerated electrons from FAST, *J. Geophys. Res.*, *108*, doi:10.1029/2002JA009420, 2003.

Coroniti, F. V., and C. F. Kennel, Can the ionosphere regulate magnetospheric convection?, *J. Geophys. Res.*, *78*, 2837–2851, 1973.

Coumans, V., J.-C. Gérard, B. Hubert, S. B. Mende, and S. W. H. Cowley, Morphology and seasonal variations of global auroral proton precipitation observed by IMAGE-FUV, *J. Geophys. Res.*, *109*, doi:10.1029/2003JA010348, 2004.

Coumans, V., J.-C. Gérard, B. Hubert, and M. Meurant, Global auroral proton precipitation observed by IMAGE-FUV: Noon and midnight brightness dependence on solar wind characteristics and IMF orientation, *J. Geophys. Res.*, *111*, doi:10.1029/2005JA011317, 2006.

Cowley, S. W. H., Asymmetry effects associated with the x-component of the IMF in a magnetically open magnetosphere, *Planet. Space Sci.*, *29*(8), 809–818, 1981a.

Cowley, S. W. H., Magnetospheric asymmetries associated with the y-component of the IMF, *Planet. Space Sci.*, *29*(1), 79–96, 1981b.

Cowley, S. W. H., and M. Lockwood, Excitation and decay of solar wind-driven flows in the magnetosphere-ionosphere system, *Ann. Geophys.*, pp. 103–115, 1992.

Cowley, S. W. H., J. P. Morelli, and M. Lockwood, Dependence of convective flows and particle precipitation in the high-latitude dayside ionosphere on the x and y components of the interplanetary magnetic field, *J. Geophys. Res.*, *96*, 5557–5564, 1991.

Craven, J. D., J. S. M. L. A. Frank, and L. L. Cogger, Simultaneous optical observations of transpolar arcs in the two polar caps, *Geophys. Res. Lett.*, *18*, 2297 – 2300, 1991.

Crooker, N. U., Reverse convection, *J. Geophys. Res.*, pp. 19,363–19,372, 1992.

Dessler, A. J., and E. N. Parker, Hydromagnetic theory of geomagnetic storms, *J. Geophys. Res.*, *64*, 2239–2252, 1959.

DeWitt, R. N., The occurrence of aurora in geomagnetically conjugate areas, *J. Geophys. Res.*, *62*, 1347–1352, 1962.

Dungey, J. W., Interplanetary magnetic field and the auroral zones, *Phys. Rev. Lett.*, *6*, 47–48, 1961.

Elphinstone, R. D., K. Jankowska, J. S. Murphree, and L. L. Cogger, The configuration of the auroral distribution for interplanetary magnetic field B_z northward 1. IMF B_x and B_y dependencies as observed by the Viking satellite, *J. Geophys. Res.*, *95*, 5791–5804, 1990.

Evans, D. S., Precipitating electron fluxes formed by a magnetic field aligned potential difference, *J. Geophys. Res.*, *79*, 2853–2858, 1973.

Fairfield, D. H., On the average configuration of the geomagnetic tail, *J. Geophys. Res.*, *84*, 1950–1958, 1979.

Fillingim, M. O., G. K. Parks, H. U. Frey, T. J. Immel, and S. B. Mende, Hemispheric asymmetry of the afternoon electron aurora, *Geophys. Res. Lett.*, *32*, doi: 10.1029/2004GL021635, 2005.

Fillingim, M. O., J. P. Eastwood, G. K. Parks, V. Angelopoulos, I. R. Mann, S. B. Mende, and A. T. Weatherwax, Polar UVI and THEMIS GMAG observations of the ionospheric response to a hot flow anomaly, *J. Atmos. Terr. Phys.*, doi: doi:10.1016/j.jastp.2010.03.001, 2010.

Frank, L. A., and J. B. Sigwarth, Simultaneous images of the northern and southern auroras from the Polar spacecraft: An auroral substorm, *J. Geophys. Res.*, *108*, doi: 10.1029/2002JA009356, 2003.

Frank, L. A., J. B. Sigwarth, J. D. Craven, J. P. Cravens, J. S. Dolan, M. R. Dvorsky, P. K. Hardebeck, J. D. Harvey, and D. W. Muller, The visible imaging system VIS for the Polar spacecraft, *Space Sci. Rev.*, *71*, 297–328, 1995.

Frey, H. U., Localized aurora beyond the auroral oval, *Reviews of Geophysics*, *45*, 2007.

Frey, H. U., and S. B. Mende, Substorm onsets as observed by IMAGE-FUV, in *Substorms VIII: Proc. of the 8th International Conference on Substorms*, pp. 71–76, Univ. of Calgary Press, Calgary, 2006.

Frey, H. U., S. B. Mende, H. B. Vo, M. Brittnacher, and G. K. Parks, Conjugate observation of optical aurora with Polar satellite and ground-based cameras, *Advances in Space Research*, *23*, 1647–1652, 1999.

Frey, H. U., S. B. Mende, C. W. Carlson, J.-C. Gérard, B. . Hubert, J. Spann, R. Gladstone, and T. J. Immel, The electron and proton aurora as seen by IMAGE-FUV and FAST, *Geophys. Res. Lett.*, *28*, 1135–1138, 2001.

Frey, H. U., T. D. Phan, S. A. Fuselier, and S. B. Mende, Continuous magnetic reconnection at Earth's magnetopause, *Nature*, *426*, 533–537, 2003a.

Frey, H. U., S. B. Mende, V. Angelopoulos, and E. F. Donovon, Substorm onset observations by IMAGE-FUV, *J. Geophys. Res.*, *109*, doi:10.1029/2004JA010607, 2004.

Frey, H. U., et al., Summary of quantitative interpretation of IMAGE far ultraviolet auroral data, *Space Sci. Rev.*, *109*, 255–283, 2003b.

Fujii, R., N. Sato, T. Ono, H. Fukunishi, T. Hirasawa, S. Kokubun, T. Araki, and T. Saemundsson, Conjugacies of pulsating auroras by all-sky TV observations, *Geophys. Res. Lett.*, *14*, 115–118, 1987.

Galand, M., and D. Lummerzheim, Contribution of proton precipitation to space-based auroral FUV observations, *J. Geophys. Res.*, *109*, doi:10.1029/2003JA010321, 2004.

Gérard, J., B. Hubert, M. Meurant, V. I. Shematovich, D. V. Bisikalo, H. Frey, S. Mende, G. R. Gladstone, and C. W. Carlson, Observation of the proton aurora with IMAGE FUV imager and simultaneous ion flux in situ measurments, *J. Geophys. Res.*, *106*, 28,939–28,948, 2001.

Gérard, J.-C., B. Hubert, D. V. Bisikalo, and V. I. Shematovich, A model of the Lyman-α line profile in the proton aurora, *J. Geophys. Res.*, *105*, 15,795–15,805, 2000.

Gjerloev, J. W., R. A. Hoffman, J. B. Sigwarth, L. A. Frank, and J. B. H. Baker, Typical auroral substorm: A bifurcated oval, *J. Geophys. Res.*, *113*, doi:10.1029/2007JA012431, 2008.

Gonzalez, W., J. Joselyn, Y. Kamide, H. Kroehl, G. Rostoker, B. Tsurutani, and V. Vasyliunas, What is a geomagnetic storm?, *J. Geophys. Res.*, *99*, 5771–5792, 1994.

Griffiths, D. J., *Introduction to electrodynamics*, 3.rd ed., Prentice Hall, 1981.

Grocott, A., T. K. Yeoman, S. E. Milan, and S. W. H. Cowley, Interhemispheric observations of the ionospheric signature of tail reconnection during IMF-northward non-substorm intervals, *Ann. Geophys.*, *23*, 1763–1770, 2005.

Grocott, A., J. A. Wild, S. E. Milan, and T. K. Yeoman, Superposed epoch analysis of the ionospheric convection evolution during substorms: Onset latitude dependence, *Ann. Geophys.*, *27*, 591–600, 2009.

Haaland, S. E., G. Paschmann, M. Forster, J. M. Quinn, R. B. Torbert, C. E. McIlwain, H. Vaith, P. A. Puhl-Quinn, and C. A. Kletzing, High-latitude plasma convection from cluster EDI measurements: Method and IMF-dependence, *Ann. Geophys.*, pp. 239–253, 2007.

Hargreaves, J. K., Conjugate and closely-spaced observations of auroral radio absorption - I, *Planet. Space Sci.*, *17*, 1459–1484, 1969.

Heppner, J. P., and N. C. Maynard, Empirical high-latitude electric field models, *J. Geophys. Res.*, *92*, 4467–4489, 1987.

Holzworth, R. H., and C.-I. Meng, Mathematical representation of the auroral oval, *Geophys. Res. Lett.*, *2*, 377–380, 1975.

Holzworth, R. H., and C.-I. Meng, Auroral boundary variations and the interplanetary magnetic field, *Planet. Space Sci.*, *32*, 25–29, 1984.

Hubert, B., J.-C. Gérard, D. V. Bisikalo, V. I. Shemantovich, and S. C. Solomon, The role of proton precipitation in the excitation of auroral FUV emissions, *J. Geophys. Res.*, *106*, 21,475–21,494, 2001.

Hubert, B., J.-C. Gérard, D. S. Evans, M. Meurant, S. B. Mende, H. U. Frey, and T. J. Immel, Total electron and proton energy input during auroral substorms: Remote sensing with IMAGE-FUV, *J. Geophys. Res.*, *107*, doi:10.1029/2001JA009229, 2002.

Hubert, B., S. E. Milan, A. Grocott, C. Blockx, S. W. H. Cowley, and J. C. Gérard, Dayside and nightside reconnection rates inferred from IMAGE-FUV and Super Dual Auroral Radar Network data, *J. Geophys. Res.*, *111*, doi:10.1029/2005JA011140, 2006.

Imber, S. M., S. E. Milan, and B. Hubert, Observations of significant flux closure by dual lobe reconnection, *Ann. Geophys.*, *25*, 1617–1627, 2006.

Immel, T., S. Mende, H. Frey, N. Østgaard, and G. Gladstone, Effects of the 14 July 2000 solar flare on Earth's FUV emissions, *J. Geophys. Res.*, *108*, doi:10.1029/2001JA009060, 2003.

Jørgensen, T. S., E. Friis-Christensen, and J. Wilhjelm, Interplanetary magnetic-field directions and high-latitude ionospheric currents, *J. Geophys. Res.*, *77*, 1976–1977, 1972.

Khurana, K. K., R. J. Walker, and T. Ogino, Magnetospheric convection in the presence of interplanetary magnetic field B_y: A conceptual model and simulations, *J. Geophys. Res.*, *101*, 4907–4916, 1996.

Kivelson, M. G., and C. T. Russell, *Introduction to space physics*, Cambridge University Press, Cambridge, UK, 1995.

Knight, S., Parallel electric fields, *Planet. Space Sci.*, *21*, 741, 1973.

Kokubun, S., T. Yamamoto, M. H. Acuna, K. Hayashi, K. Shiokawa, and H. Kawano, The geotail magnetic field experiment, *Journal of Geomagnetism and Geoelectricity*, *46*, 7–21, 1994.

Liou, K., P. T. Newell, C.-I. Meng, M. Brittnacher, and G. Parks, Characteristics of the solar wind controlled auroral emissions, *J. Geophys. Res.*, *103*, 17,543–17,557, 1998.

Liou, K., P. T. Newell, and C.-I. Meng, Seasonal effects on auroral particle acceleration and precipitation, *J. Geophys. Res.*, *106*, 5531–5542, 2001.

Liou, K., C.-I. Meng, A. T. Y. Lui, P. T. Newell, and S. Wing, Magnetic dipolarization with substorm expansion onset, *J. Geophys. Res.*, *107*, doi:10.1029/2001JA000179, 2002.

Liou, K., P. T. Newell, J.-H. Shue, C.-I. Meng, Y. Miyashita, H. Kojima, and H. Matsumoto, "Compression aurora": Particle precipitation driven by long-duration high solar wind ram pressure, *J. Geophys. Res.*, *112*, doi:10.1029/2007JA012443, 2007.

Lockwood, M., S. W. H. Cowley, and M. P. Freeman, The excitation of plasma convection in the high-latitude ionosphere, *J. Geophys. Res.*, *95*, 7961–7972, 1990.

Lu, G., et al., Interhemispheric asymmetry of the high-latitude ionospheric convection pattern, *J. Geophys. Res.*, *99*, 6491–6510, 1994.

Lysak, R. L., Feedback instability of the ionospheric resonant cavity, *J. Geophys. Res.*, *96*, 1553–1568, 1991.

Mansurov, S. M., New evidence of a relationship between magnetic fields in space and on Earth, *Geomagn. Aeron.*, *9*, 622, 1969.

McComas, D., S. Bame, P. Barker, W. Feldman, J. Phillips, P. Riley, and J. Griffee, Solarwind Electron Proton Alphamonitor (SWEPAM) for the Advanced Composotion Explorer, *Space Sci. Rev.*, *86*, 563–612, 1998.

Mende, S., et al., Far ultraviolet imaging from the IMAGE spacecraft. 1. System design, *Space Sci. Rev.*, *91*, 243–270, 2000a.

Mende, S. B., H. U. Frey, T. J. Immel, J.-C. Gérard, B. Hubert, and S. A. Fuselier, Global imaging of proton and electron aurorae in the far ultraviolet, *Space Sci. Rev.*, *109*, 211–254, 2003a.

Mende, S. B., H. U. Frey, B. J. Morsony, and T. J. Immel, Statistical behavior of proton and electron auroras during substorms, *J. Geophys. Res.*, *108*, doi:10.1029/2002JA009751, 2003b.

Mende, S. B., et al., Far ultraviolet imaging from the IMAGE spacecraft. 3. Spectral imaging of Lyman-α and OI 135.6 nm, *Space Sci. Rev.*, *91*, 287–318, 2000b.

Mende, S. B., et al., Far ultraviolet imaging from the IMAGE spacecraft. 2. wideband FUV imaging, *Space Sci. Rev.*, *91*, 271–285, 2000c.

Meng, C.-I., R. H. Holzworth, and S.-I. Akasofu, Auroral circle - delineating the poleward boundary of the quiet auroral belt, *J. Geophys. Res.*, *82*, 164–172, 1977.

Meurant, M., J.-C. Gérard, C. Blockx, B. Hubert, and V. Coumans, Propagation of electron and proton shock-induced aurora and the role of the interplanetary magnetic field and solar wind, *J. Geophys. Res.*, *109*, doi:10.1029/2004JA010453, 2004.

Milan, S. E., G. Provan, and B. Hubert, Magnetic flux transport in the dungey cycle: A survey of dayside and nightside reconnection rates, *J. Geophys. Res.*, *112*, doi:10.1029/2006JA011642, 2007.

Milan, S. E., A. Grocott, C. Forsyth, S. M. Imber, P. D. Boakes, and B. Hubert, A superposed epoch analysis of auroral evolution during substorm growth, onset and recovery: Open magnetic flux control of substorm intensity, *Ann. Geophys.*, pp. 659–668, 2009a.

Milan, S. E., J. Hutchinson, P. D. Boakes, and B. Hubert, Influences on the radius of the auroral oval, *Ann. Geophys.*, *27*, 2913–2924, 2009b.

Minatoya, H., N. Sato, T. Saemundsson, and T. Yoshino, Large displacements of conjugate auroras in the midnight sector, *J. Geomag. Geoelectr.*, *48*, 967–975, 1996.

Newell, P. T., C.-I. Meng, and K. M. Lyons, Suppression of discrete aurorae by sunlight, *Nature*, *381*, 766–767, 1996.

Newell, P. T., J. M. Ruohoniemi, and C.-I. Meng, Maps of precipitation by source region, binned by IMF, with inertial convection streamlines, *J. Geophys. Res.*, *109*, doi:10.1029/2004JA010499, 2004.

Newell, P. T., T. Sotirelis, and S. Wing, Diffuse, monoenergetic, and broadband aurora: The global precipitation budget, *J. Geophys. Res.*, *114*, doi:10.1029/2009JA014326, 2009.

Newell, P. T., T. Sotirelis, and S. Wing, Seasonal variations in diffuse, monoenergetic, and broadband aurora, *J. Geophys. Res.*, *115*, doi:10.1029/2009JA014805, 2010.

Ohtani, S., S. Wing, G. Ueno, and T. Higuchi, Dependence of premidnight field-aligned currents and particle precipiation on solar illumination, *J. Geophys. Res.*, *114*, doi:10.1029/2009JA014115, 2009.

Østgaard, N., S. B. Mende, H. U. Frey, L. A. Frank, and J. B. Sigwarth, Observations of non-conjugate theta aurora, *Geophys. Res. Lett.*, *30*, doi:10.1029/2003GL017914, 2003.

Østgaard, N., S. B. Mende, H. U. Frey, T. J. Immel, L. A. Frank, J. B. Sigwarth, and T. J. Stubbs, Interplanetary magnetic field control of the location substorm onset and auroral features in the conjugate hemisphere, *J. Geophys. Res.*, *109*, doi:10.1029/2003JA010370, 2004.

Østgaard, N., S. B. Mende, H. U. Frey, and J. B. Sigwarth, Simultaneous imaging of the reconnection spot in the opposite hemispheres during northward IMF, *Geophys. Res. Lett.*, *32*, doi:10.1029/2005GL024491, 2005a.

Østgaard, N., J. Moen, S. B. Mende, H. U. Frey, T. J. Immel, P. Gallop, K. Oksavik, and M. Fujimoto, Estimates of magnetotail reconnecton rate based on IMAGE FUV and EISCAT measurements, *Ann. Geophys.*, *23*, 123–134, 2005b.

Østgaard, N., N. A. Tsyganenko, S. B. Mende, H. U. Frey, T. J. Immel, M. Fillingim, L. A. Frank, and J. B. Sigwarth, Observations and model predictions of substorm auroral asymmetries in the conjugate hemispheres, *Geophys. Res. Lett.*, *32*, doi: 10.1029/2004GL022166, 2005c.

Østgaard, N., S. B. Mende, H. U. Frey, J. B. Sigwarth, A. Aasnes, and J. Weygand, Auroral conjugacy studies based on global imaging, *J. Atmos. Terr. Phys.*, *69*, 249–255, 2007.

Oznovich, I., R. W. Eastes, R. E. Hoffman, M. Tur, and I. Glaser, The aurora at quiet magnetospheric conditions: Repeatability and dipole tilt angle dependence, *J. Geophys. Res.*, *98*, 3789–3797, 1993.

Papitashvili, V. O., and F. J. Rich, High-latitude ionospheric convection models derived from Defense Meteorological Satellite Program ion drift observations and parameterized by the interplanetary magnetic field strength and direction, *J. Geophys. Res.*, *107*, doi: 10.1029/2001JA000264, 2002.

Parker, E. N., The alternative paradigm for magnetospheric physics, *J. Geophys. Res.*, *101*, 10,587–10,625, 1996.

Parker, E. N., Reply, *J. Geophys. Res.*, *102*, 9657–9658, 1997.

Parker, E. N., *Newton, Maxwell, and magnetospheric physics*, *AGU Geophysical monograph*, vol. 118, pp. 1–10, Washington D.C., 2000.

Parker, E. N., *Conversations on electric and magnetic fields in the cosmos*, Princeton University Press, Princeton and Oxford, 2007.

Paschmann, G., S. Haaland, and R. Treumann, *Auroral Physics*, Kluwer Academic, Dordrecht, 2003.

Petrukovich, A. A., Dipole tilt effects in plasma sheet B_y : Statistical model and extreme values, *Ann. Geophys.*, pp. 1343–1352, 2009.

Provan, G., M. Lester, S. B. Mende, and S. E. Milan, Statistical study of high-latitude plasma flow during magnetospheric substorms, *Ann. Geophys.*, *22*, 3607–3624, 2004.

Pulkkinen, T. I., D. N. Baker, R. J. Pellinen, J. S. Murphree, and L. A. Frank, Mapping of the auroral oval and individual arcs during substorms, *J. Geophys. Res.*, *100*, 21,987–21,994, 1995.

Richmond, A. D., Ionospheric electrodynamics using magnetic apex coordinates, *J. Geomag. Geoelectr.*, *47*, 191–212, 1995.

Robinson, R. M., R. R. Vondrak, K. Miller, T. Dabbs, and D. Hardy, On calculating ionospheric conductances from the flux and energy of precipitating electrons, *J. Geophys. Res.*, *92*, 2565–2569, 1987.

Ruohoniemi, J. M., and R. A. Greenwald, Dependencies of high-latitude plasma convection: Consideration of interplanetary magnetic field, seasonal, and universal time factors in statistical patterns, *J. Geophys. Res.*, *110*, doi:10.1029/2004JA010815, 2005.

Sato, N., R. Fujii, T. Ono, H. Fukunishi, T. Hirasawa, T. Araki, S. Kokubun, K. Makita, and T. Saemundsson, Conjugacy of proton and electron auroras observed near $L = 6.1$, *Geophys. Res. Lett.*, *13*, 1368–1371, 1986.

Sato, N., T. Nagaoka, K. Hashimoto, and T. Saemundsson, Conjugacy of isolated auroral arcs and nonconjugate auroral breakups, *J. Geophys. Res.*, *103*, 11,641–11,652, 1998.

Sato, N., D. M. Wright, C. W. Carlson, Y. Ebihara, M. Sato, T. Saemundsson, S. E. Milan, and M. Lester, Generation region of pulsating aurora obtained simultaneously by the FAST satellite and a Syowa-Iceland conjugate pair of observatories, *J. Geophys. Res.*, *109*, doi:10.1029/2004JA010419, 2004.

Sato, N., A. Kadokura, Y. Ebihara, H. Deguchi, and T. Saemundsson, Tracing geomagnetic conjugate points using exceptionally similar synchronous auroras, *Geophys. Res. Lett.*, *32*, doi:10.1029/2005GL023710, 2005.

Scholer, M., On the motion of artificial ion clouds in the magnetosphere, *Planet. Space Sci.*, *18*, 977, 1970.

Sckopke, N., A general relation between the energy of trapped particles and the disurbance field near the earth, *J. Geophys. Res.*, *71*, 3125–3130, 1966.

Sergeev, V. A., E. M. Sazhina, N. A. Tsyganenko, J. A. Lundblad, and F. Søraas, Pitch-angle scattering of energetic protons in the magnetotail current sheet as the dominant source of their isotropic precipitation into the nightside ionosphere, *Planet. Space Sci.*, *31*, 1147–1155, 1983.

Sergeev, V. A., K. Liou, C.-I. Meng, P. T. Newell, M. Brittnacher, G. Parks, and G. D. Reeves, Development of auroral streamers in association with localized impulsive injections to the inner magnetotail, *Geophys. Res. Lett.*, *26*, 417–420, 1999.

Shay, M. A., and M. Swisdak, Three-species collisionless reconnection: Effect of O+ on magnetotail reconnection, *Phys. Rev. Lett.*, *93*, doi:10.1103/PhysRevLett.93.175001, 2004.

Shue, J.-H., P. T. Newell, K. Liou, C.-I. Meng, and S. W. H. Cowley, Interplanetary magnetic field B_x asymmetry effect on auroral brightness, *J. Geophys. Res.*, *107*, doi: 10.1029/2001JA000229, 2002.

Siscoe, G. L., and T. S. Huang, Polar cap inflation and deflation, *J. Geophys. Res.*, *90*, 543–547, 1985.

Smith, C., J. L'Heureux, N. Ness, M. Acuña, L. Burlaga, and J. Scheifele, The ACE magnetic fields experiment, *Space Sci. Rev.*, *86*, 613–632, 1998.

Snekvik, K., R. Nakamura, N. Østgaard, S. Haaland, and A. Retino, The hall current system revealed as a statistical significant pattern during fast flows, *Ann. Geophys.*, *26*, 3429–3437, 2008.

Song, P., V. M. Vasyliunas, and X.-Z. Zhou, Magnetosphere-ionosphere/thermosphere coupling: Self-consistent solutions for a one-dimensional stratified ionosphere in three-fluid theory, *J. Geophys. Res.*, *114*, doi:10.1029/2008JA013629, 2009.

Stenbaek-Nielsen, H. C., and A. Otto, Conjugate auroras and the interplanetary magnetic field, *J. Geophys. Res.*, *102*, 2223–2232, 1997.

Stenbaek-Nielsen, H. C., T. N. Davis, and N. W. Glass, Relative motion of auroral conjugate points during substorms, *J. Geophys. Res.*, *77*, 1844–1858, 1972.

Stenbaek-Nielsen, H. C., E. M. Wescott, T. N. Davis, and R. W. Peterson, Differences in auroral intensity at conjugate points, *J. Geophys. Res.*, *78*, 659–671, 1973.

Stone, E. C., A. M. Frandsen, R. A. Mewaldt, E. R. Christian, D. Margolies, J. F. Ormes, and F. Snow, The Advanced Composotion Explorer, *Space Sci. Rev.*, *86*, 1–22, 1998.

Strickland, D. J., R. J. Cox, R. R. Meier, and D. P. Drob, Global O/N_2 derived from DE 1 FUV dayglow data: Technique and examples from two storm periods, *J. Geophys. Res.*, *104*, 4251–4266, 1998.

Stubbs, T. J., R. R. Vondrak, N. Østgaard, J. B. Sigwarth, and L. A. Frank, Simultaneous observations of the auroral ovals in both hemispheres under varying conditions, *Geophys. Res. Lett.*, *32*, doi:10.1029/2004GL021199, 2005.

Svalgaard, L., *Sector structure of the interplanetary magnetic field and daily variation of the geomagnetic field at high latitudes*, Geophys Pap. R-6, Danish Meterol. Inst., Charlottenlund, 1968.

Tanaka, T., Interplanetary magnetic field B_y and auroral conductance effects on high-latitude ionospheric convection patterns, *J. Geophys. Res.*, *106*, 24,505–24,516, 2001.

Tsurutani, B. T., D. E. Jones, R. P. Lepping, E. J. Smith, and D. G. Sibeck, The relationship beteween the IMF B_y and the distant tail $(150 - 238R_E)$ lobe and plasmasheet B_y fields, *Geophys. Res. Lett.*, *11*, 1082–1085, 1984.

Tsyganenko, N. A., A model of the near magnetosphere with a dawn-dusk asymmetry 1. Mathematical structure, *J. Geophys. Res.*, *107*, doi:10.1029/2001JA000219, 2002.

VanZandt, T. E., W. L. Clark, and J. W. Warnock, Magnetic Apex Coordinates: A Magnetic Coordinate System for the Ionospheric F2 Layer, *J. Geophys. Res.*, *77*, 2406–2411, 1972.

Vasyliunas, V. M., *Steady state aspects of magnetic field line merging*, *Geophys. Mongr. Ser.*, vol. 30, pp. 25–31, AGU, Washington D.C., 1984.

Vasyliunas, V. M., Electric field and plasma flow: What drives what?, *Geophys. Res. Lett.*, *28*, 2177–2180, 2001.

Vasyliunas, V. M., Relation between magnetic fields and electric currents in plasmas, *Ann. Geophys.*, *23*, 2589–2597, 2005a.

Vasyliunas, V. M., Time evolution of electric fields and currents and the generalized Ohm's law, *Ann. Geophys.*, *23*, 1347–1354, 2005b.

Vasyliunas, V. M., and P. Song, Meaning of ionospheric Joule heating, *J. Geophys. Res.*, *110*, doi:10.1029/2004JA010615, 2005.

Vo, H. B., J. S. Muphree, D. Hearn, P. T. Newell, and C.-I. Meng, A satellite study of dayside auroral conjugacy, *Ann. Geophys.*, *13*, 1134–1143, 1995.

Vorobjev, V. G., O. I. Yagodkina, D. Sibeck, K. Liou, and C.-I. Meng, Aurora conjugacy during substorms: Coordinated Antarctic ground and Polar Ultraviolet observations, *J. Geophys. Res.*, *106*, 24,579–24,591, 2001.

Wang, H., H. Lühr, S. Y. Ma, and H. U. Frey, Interhemispheric comparison of average substorm onset locations: Evidence for deviation from conjugacy, *Ann. Geophys.*, *25*, 989–999, 2007.

Watanabe, M., A. Kadokura, N. Sato, and T. Saemundsson, Absence of geomagnetic conjugacy in pulsating auroras, *Geophys. Res. Lett.*, *34*, doi:10.1029/2007GL030469, 2007a.

Watanabe, M., G. J. Sofko, K. Kabin, R. Rankin, A. J. Ridley, C. R. Clauer, and T. I. Gombosi, Origin of the interhemispheric potential mismatch of merging cells for interplanetary magnetic field B_y-dominated periods, *J. Geophys. Res.*, *112*, doi: 10.1029/2006JA012179, 2007b.

Weimer, D. R., Models of high-latitude electric potentials derived with a least error fit of spherical harmonic coefficients, *J. Geophys. Res.*, *100*, 19,595–19,607, 1995.

Weimer, D. R., Correction to "Predicting interplanetary magnetic field (IMF) propagation delay times using the minimum variance technique", *J. Geophys. Res.*, *109*, doi: 10.1029/2004JA010691, 2004.

Wescott, E. M., Magnetoconjugate phenomena, *Space Sci. Rev.*, *5*, 507–561, 1966.

Wing, S., P. T. Newell, D. G. Sibeck, and K. B. Baker, A large statistical study of the entry of interplanetary magnetic field y-component into the magnetosphere, *Geophys. Res. Lett.*, *22*, 2083–2086, 1995.

Zhang, Y., L. J. Paxton, and A. T. Y. Lui, An unusual nightside distortion of the auroral oval: TIMED/GUVI and IMAGE/FUV observations, *J. Geophys. Res.*, *111*, doi: 10.1029/2005JA011217, 2006.